Czech technical university in Prague

Department of Fluid Dynamics and Thermodynamics

Doctoral Thesis

# Verified Unsteady Model for Analysis of Contra-Rotating Propeller Aerodynamics

*Author:*
Ing. Vít Štorch

*Supervisor:*
Prof. Ing. Jiří Nožička CSc.
*Co-supervisor:*
Ing. Jan Čížek, Ph.D.

*A thesis submitted in fulfilment of the requirements for the degree of Doctor of Philosophy*

*in the field of*

Thermodynamics and Fluid Dynamics

September 2017

# Declaration of Authorship

I, Ing. Vít Štorch, declare that this thesis titled, 'Verified Unsteady Model for Analysis of Contra-Rotating Propeller Aerodynamics' and the work presented in it are my own. I confirm that:

- This work was done wholly or mainly while in candidature for a research degree at this University.
- Where any part of this thesis has previously been submitted for a degree or any other qualification at this University or any other institution, this has been clearly stated.
- Where I have consulted the published work of others, this is always clearly attributed.
- Where I have quoted from the work of others, the source is always given. With the exception of such quotations, this thesis is entirely my own work.
- I have acknowledged all main sources of help.

Signed: _____

Date: _____

*"The man has no wings... But I think he will fly not relying on the strength of his muscles, but on the strength of his mind"*

Nikolai Y. Joukowsky

CZECH TECHNICAL UNIVERSITY IN PRAGUE

Faculty of Mechanical Engineering
Department of Fluid Dynamics and Thermodynamics

Doctoral Thesis

**Verified Unsteady Model for Analysis of Contra-Rotating Propeller Aerodynamics**

by Ing. Vít Štorch

# *Abstract*

The doctoral thesis is focused on the development of a new computational model for analysis of contra-rotating propellers, its testing and verification, and application on selected important problems of contra-rotating propeller aerodynamics. An insight into both past and current state-of-the-art methods for numerical simulation of propellers is provided with focus on contra-rotating propellers. Two of the discussed methods, simpler lifting line method and 3D panel method complemented by boundary layer, are used for rotating blade representation. An unsteady force-free wake model is attached to both blade models for induced velocity determination. Robust 3D panel method is coupled with a two-equation integral boundary layer with a new interaction law that enables seamless solution of boundary layer in regions of strong interaction. As a result, the instantaneous velocity fields, wake shapes, pressure forces and friction forces on the blades are available together with overall performance data for arbitrary contra-rotating propeller geometry. The components of the complex model are tested and validated step by step using well defined problems. The newly developed computational tool is used for analysis of a propeller set and the results are compared with experimental data. Finally, effects of rotational rate ratio, propeller distance, advance ratio and angle of free stream velocity are described and a comparison of contra-rotating propeller to an equivalent single propeller is performed.

**Keywords:** contra-rotating propellers, 3D panel method, boundary layer, interaction law, vortex wake, transition, lifting line method

# *Acknowledgements*

The writing of this thesis and connected research would not be possible without a friendly attitude and support of colegues at the Department of Fluid Dynamics and Thermodynamics. I would like to thank especially my supervisor, prof. Ing. Jiří Nožička, CSc. for his help and advice. I am also very grateful to my co-supervisor Ing. Jan Čížek, Ph.D. and to prof. Ing. Pavel Šafařík CSc. and doc. Ing. Tomáš Hyhlík, Ph.D. for sharing their opinions, giving me helpful tips and guiding me through my studies. The experimental setup used for validations has been built with a tremendous help from Ing. Martin Brada, Ing. Jiří Gemperle, Ing. Jakub Filipský and Petr Mihalov.

Furthermore, I cannot ommit to mention the most important people in my life, my family, parents and my wife, who contributed perhaps in a different way than those mentioned before, by providing me with a great working environment and peace of mind.

This work was funded in part by the Grant Agency of the Czech Technical University grants No.:
SGS 16/068/OHK2/1T/12
SGS 15/065/OHK2/1T/12
SGS 14/057/OHK2/1T/12

The typesetting of this thesis has been done using LaTeX. Computations except those in Appendix B and generation of most figures have been performed using MATLAB.

# Contents

# List of Figures

# Abbreviations

| | |
|---|---|
| **BEM** | **B**lade **E**lement **M**omentum |
| **BL** | **B**oundary **L**ayer |
| **CFD** | **C**omputational **F**luid **D**ynamics |
| **CRP** | **C**ontra-**R**otating **P**ropeller |
| **CTA** | **C**onstant **C**urrent **A**nemometry |
| **GUI** | **G**raphical **U**ser **I**nterface |
| **L.E.** | **L**eading **E**dge |
| **LIF** | **L**aser **I**nduced **F**luorescence |
| **LL** | **L**ifting **L**ine (method) |
| **LS** | **L**ifting **S**urface (method) |
| **M.A.C.** | **M**ean **A**erodynamic **C**hord |
| **NACA** | **N**ational **A**dvisory **C**ommittee for **A**eronautics |
| **NASA** | **N**ational **A**eronautics and **S**pace **A**dministration |
| **PM** | **P**anel **M**ethod |
| **PS1** | **P**ropeller **S**et 1 |
| **PWM** | **P**ulse **W**idth **M**odulation |
| **PIV** | **P**article **I**mage **V**elocimetry |
| **RANS** | **R**eynolds **A**veraged **N**avier **S**tokes |
| **r.h.s** | **r**ight **h**and **s**ide |
| **rpm** | **r**otations **p**er **m**inute |
| **T.E.** | **T**railing **E**dge |
| **UAV** | **U**nmanned **A**erial **V**ehicle |
| **VAWT** | **V**ertical **A**xis **W**ind **T**urbine |

# Symbols

| | | |
|---|---|---|
| $A$ | area | $m^2$ |
| $A_{i,j}$ | vortex panel influence coefficient matrix | method specific |
| $b$ | chord length | m |
| $c$ | velocity | m $s^{-1}$ |
| $c_\infty$ | free stream velocity | m $s^{-1}$ |
| $C_D$ | boundary layer dissipation coefficient | 1 |
| $C_f$ | skin friction coefficient | 1 |
| $C_\tau$ | shear stress coefficient | 1 |
| $C_{\tau EQ}$ | equilibrium shear stress coefficient | 1 |
| $c_D$ | coefficient of wing drag | 1 |
| $c_d$ | coefficient of airfoil drag | 1 |
| $c_L$ | coefficient of wing lift | 1 |
| $c_l$ | coefficient of airfoil lift | 1 |
| $c_p$ | coefficient of pressure | 1 |
| $c_P$ | power coefficient | 1 |
| $c_T$ | thrust coefficient | 1 |
| $c_Q$ | torque coefficient | 1 |
| $D$ | diameter | m |
| $d_{ij}$ | interaction coefficient | $s^{-1}$ |
| $d_p$ | propeller pitch | m |
| $F_D$ | drag force | N |
| $F_L$ | lift force | N |
| $FoM$ | Figure of Merit | 1 |
| $f$ | frequency | Hz |
| $g$ | gravitational acceleration | m $s^{-2}$ |

| | | |
|---|---|---|
| $H$ | boundary layer shape parameter | 1 |
| $H^*$ | kinetic energy shape parameter | 1 |
| $k_i$ | generally used for various constants | ˜ |
| $l$ | length | m |
| $M, N$ | vector and matrix dimensions | 1 |
| $m$ | mass | kg |
| $\dot{m}$ | mass flow rate | kg $s^{-1}$ |
| $N_b$ | number of blades | 1 |
| $\vec{n}$ | normal vector | m |
| $\tilde{n}$ | Tollmien-Schlichting wave amplification exponent | 1 |
| $P$ | power | W |
| $p$ | pressure (static) | Pa |
| $p_0$ | total pressure | Pa |
| $Q$ | torque | N m |
| $R$ | radius | m |
| $r$ | radial coordinate | m |
| $\vec{r}$ | radius vector | m |
| $Re$ | Reynolds number with respect to chord length | 1 |
| $Re_\theta$ | momentum thickness Reynolds number | 1 |
| $SPL$ | sound pressure level | dB |
| $s$ | coordinate along a curve | m |
| $T$ | thrust force | N |
| $t$ | time | s |
| $u_e$ | boundary layer edge velocity | m $s^{-1}$ |
| $U, V, W$ | velocity influence matrices | 1 |
| $x, y, z$ | global coordinates | m |
| $\bar{x}, \bar{y}, \bar{z}$ | local coordinates | m |
| | | |
| $\alpha$ | angle of attack | ° |
| $\beta$ | incidence angle | ° |
| $\Gamma$ | circulation | $m^2 s^{-1}$ |
| $\gamma$ | circulation density | m $s^{-1}$ |
| $\delta^*$ | displacement thickness | m |

| | | |
|---|---|---|
| $\delta_{99}$ | boundary layer thickness by convention | m |
| $\epsilon$ | strain | 1 |
| $\zeta$ | Glauert's solution coefficient | 1 |
| $\eta$ | propulsion efficiency | 1 |
| $\eta$ | BL coordinate normal to wall | m |
| $\theta$ | momentum thickness | m |
| $\theta^*$ | kinetic energy thickness | m |
| $\lambda$ | propeller advance ratio | 1 |
| $\mu$ | dynamic viscosity | Pa s |
| $\xi$ | streamwise BL coordinate | m |
| $\nu$ | kinematic viscosity | $m^2s^{-1}$ |
| $\vec{\Pi}$ | dipole strength vector | $m^2s^{-1}$ |
| $\rho$ | density | kg $m^{-3}$ |
| $\Sigma$ | source strength | $m^2s^{-1}$ |
| $\sigma$ | panel source strength density | m $s^{-1}$ (2D) $s^{-1}$ (3D) |
| $\tau$ | shear stress | Pa |
| $\phi$ | potential | $m^2s^{-1}$ |
| $\varphi$ | angle of free stream relative to rotational axis | $^\circ$ |
| $\psi$ | stream function | $m^2s^{-1}$ |
| $\Omega$ | angular velocity | $rad^{-1}$ |
| $\vec{\omega}$ | vorticity | $s^{-1}$ |

*Subscripts*

| | |
|---|---|
| $a$ | axial direction subscript |
| $i, j, k, l$ | matrix and vector indexing subscripts |
| $n$ | normal direction subscript |
| $r$ | radial direction subscript |
| $\theta$ | tangential direction subscript |
| $x, y, z$ | global coordinates direction subscript |
| $1, 2$ | index of upstream and downstream propeller |
| $loc$ | local property (i.e. velocity) |
| $OLD, NEW$ | indicator of previous and current iteration |

*Dedicated to my dear wife Radka.*

# Chapter 1

# Introduction

## 1.1 About contra-rotating propellers

A contra-rotating propeller system consists of a pair of propellers sharing the axis of rotation and rotating in the opposite direction. This work is devoted entirely to CRP systems used for propulsion, although other areas of application, such as mixing in chemical processes, are possible. Depending on the propeller distance and direction of free stream velocity, the two propellers interact more or less intensively, producing a very complex problem of rotor aerodynamics.

Benefits that are often mentioned in connection to contra-rotating propellers (CRPs) could be summarized as follows: (1) high efficiency when highly loaded (efficiency is elaborated in Section 2.6.2), (2) low reaction torque, which can be additionally controlled by the rpm ratio, (3) high maximum thrust power for a given diameter. Drawbacks of CRP systems which limit their wider spread include higher mechanical complexity (especially when coaxial shafts are employed), high noise levels, complex aerodynamic design and often lower efficiency when used improperly or in off-design part of the operating range.

Usage of CRP systems is often dictated by design specific issues. An example of such design is Cessna 337 Skymaster (Fig. 1.1), which features engines mounted in the nose and rear of its fuselage. The main benefit of this configuration is centerline thrust in case of an engine failure. Other aerodynamic benefits of the coaxial configuration in this case are questionable since the propellers are mounted large distance apart and the flow between them is disturbed by the fuselage.

One area of CRP application is in coaxial rotor helicopters. Many designs were attempted historically with only few being successful such as coaxial helicopters developed by Russian Kamov company. A brief history with descriptions of various flying machines utilizing CRPs can be found in [1]. As in many CRP applications, important performance indicators are not only the performance parameters of hover flight but also forward and level flight performance. A technical report by Kamov company [2] indicates that efficiency of coaxial rotors in hover exceeds that of an equivalent single rotor. The efficiency benefit of a coaxial propeller is explained by the induced velocity coupling between the rotors, which reduces or eliminates the swirl behind the second rotor. Moreover a conventional helicopter requires a tailrotor. As the helicopter moves forward with increasing velocity the efficiency of a single rotor approaches and exceeds the efficiency of a coaxial rotor.

The efficiency definition of coaxial propellers and comparison to "equivalent" single rotor brings a lot of controversy. In the above example the technical report [2] uses single rotor with $2 \times N_b$ blades as an equivalent rotor to a pair of contra-rotating propellers of the same diameter with $N_b$ blades. In other study [3], when CRP system is compared against a pair of tandem (side by side) propellers, and a single rotor, the final verdict in terms of efficiency depends on the comparison criteria.


FIGURE 1.1: Cessna 337, © John Davies, used under general public license.

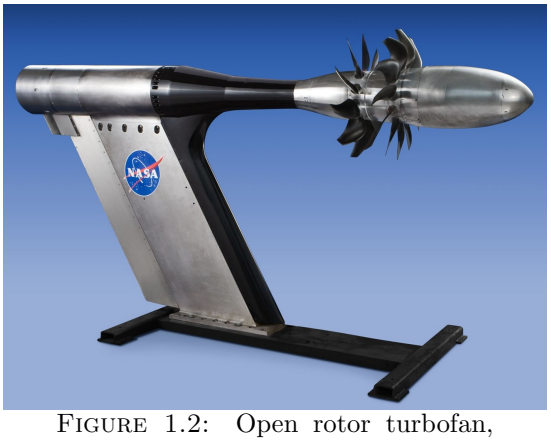


FIGURE 1.2: Open rotor turbofan, ©GE Aviation.

## 1.2 Motivation of current research and preliminary aims

The ultimate decision whether to use a CRP system or not depends on the exact problem definition and especially design limits and operating range of the device. Lack of knowledge of CRP system performance is often a contributing reason why companies in aerospace industry opt for conventional propulsion systems. With the increasing field of UAV industry, vehicles of all sizes and purposes are in need of carefully tailored

mission-specific propulsion systems. Properties of CRP systems have been studied both numerically and experimentally by several researchers, but the available results are fragmented without systematic analysis by an experimentally verified numerical tool that takes into account the unsteady nature of real viscous flow.

Use of current finite volume Navier-Stokes solvers for fast analysis of CRPs is often not practical due to reasons explained in Section 2.5.2 and researchers often develop in-house numerical tools based on potential flow solving methods. These methods are described in Section 2.7. Although some of them are very capable, they are lacking boundary layer model.

For some aerodynamicists, the problematics of contra-rotating propellers has been long time solved, however, the level of simplifications used in the past methods of analysis gives rise to many questions. What happens when the downstream blade passes through the wake of the upstream propeller? How much the thrust and power fluctuate due to unsteady nature of the flow? What is the real benefit of a contra-rotating propeller compared to an equivalent single propeller, when all aspects of the flow are accounted for?

Last but not least, the presented research is driven by curiosity about how much could current numerical methods based on potential flow solving be improved and what other kinds of flow problems could benefit from such improved computational codes.

Following the above motivation, this work is aimed to improve the understanding of flow in contra-rotating propellers through carefull implementation of new advanced modeling techniques. The advances in the computational model itself are equaly important because the resulting methods can be applied to other kinds of engineering problems.

## 1.3 Brief introduction to current state-of-the-art

There are two branches of computational methods currently used for detailed CRP analysis. Both have their advantages and disadvantages (see Chapter 2). In terms of complexity and depth of modeled phenomena, Navier-Stokes solvers offer the most complete and general answer to the problem. The development of these tools (further referred to as CFD codes) requires enormous resources and time and as such, CFD codes are in most cases a commercial product.

With CFD codes, the quality of solution depends not only on the quality of the CFD solver used, but also on the experience of the user with meshing techniques and settings of the solver. Often the solution is sought using a mesh coarser than would be ideally

required, in order to arrive to a solution in a reasonable amount of time. An example of employing state-of-the-art CFD codes are the efforts in development of open rotor CRP turbofan (Fig. 1.2), which is a part of the European research program Clean Sky and NASA's Environmentally Responsible Aviation Project. Onera RANS solver elsA [4] is being used for aerodynamics and aeroacoustics analysis of open rotor configurations (see e.g. [5]). Unsteady solutions operating on very fine sliding meshes require large computer clusters.

For optimization and fast analysis, the second branch of numerical methods is continuously being developed and relied on. These methods employ potential flow solution alone or combined with various viscous corrections. Blade element momentum (BEM) method combined with 2D polars and vortex wake is one example of such methods (see e.g. [6], [7]). Another method being used is a 3D panel method sometimes accompanied with simple viscous losses modelling (appears in [8], [9], [10] and others). Panel methods are given special attention in Chapter 3 as they promise the best compromise in terms of precision and time of solution.

Experimental research in the field of contra-rotating propellers is very scarce. One group of studies concerns marine CRPs for ship propulsion. There are also several published articles on the topic of open rotor turbofan wind tunnel experiments which are narrowly focused on the specific geometry of open rotor blades and serve for validation of numerical tools in the open rotor projects. These experiments require significant amount of funds and are often a joint venture of several companies. Another group of experiments, from which some interesting information about CRPs can be obtained, are the helicopter coaxial rotor experiments.

Standard approach to force, torque and rpm measurement is accompanied with either single pressure probe velocity measurement or more advanced PIV, LIF and CTA methods. The experimental results of various researchers are reviewed in Section 2.8.

## 1.4 Structure of the thesis

Chapters 2 and 3 contain theoretical background and results of literature review needed to summarize the shotcomings of current CRP computational models and to precisely define objectives and approach to the problem. Chapter 2 begins with description of single propeller geometry, parameters and characteristics followed by review of methods for analysis of single propellers. Although not all findings are directly applicable to a contra-rotating system of propellers (CRP), it is important to analyze the case of single propeller first, as many of these findings are transferable to the more complicated case

of CRP. The most basic methods, such as momentum theory and blade-element theory, are covered briefly. More attantion is paid to current research performed using various potential flow solvers and Navier-Stokes finite volume solvers. The remainder of Chapter 2 is devoted to current progress in design and analysis of contra-rotating propellers. After describing existing numerical methods and approaches to contra-rotating propeller design and analysis, the focus is shifted to experimental investigation of CRP performed to this date by various researchers.

Chapter 3 covers the potential flow theory and selected computational methods derived from this theory. It contains the fundamental background required for selecting a sutable type of potential flow solver.

Chapter 4 gives clear formulation of the aims and objectives of the thesis based on research of current knowledge of contra-rotating-propeller aerodynamics and numerical solution methods.

Beginning with Chapter 5, the novel computational model is being described and tested. In this chapter, the unsteady force-free vortex wake is described together with necessary theoretical background and validation tests. In Chapter 6 , the previously defined wake is connected to two different numerical representations of wings and blades and tested on model cases.

Chapter 7 describes the integral boundary layer model that was modified for the presented computational method. In the first part of the chapter, necessary theoretical background and numerical approach is presented. The second part of the chapter is devoted to the novel method of coupling the boundary layer to the inviscid flow.

Chapter 8 is focused on the experimental part of the thesis. It contains information about the design of the measurement stand, measured quantities and measurement methods. At the end of the chapter, description of geometry used for validation and numerical study is provided.

Chapter 9 summarizes the computational and experimental results and compares them in order to establish the level of precision and range of applicability of the numerical model. The results are subject to detailed analysis and discussion. The benefits of the novel approach to calculation of contra-rotating propellers are emphasized.

In the last chapter which concludes the presented thesis, the contribution to the state-of-the-art is explained and the results are summarized. As always, the presented research, while answering some questions, gives rise to others. Therefore some recommendations on the future research are given at the very end of the conclusion.

# Chapter 2

# Propeller Aerodynamics

## 2.1 Introduction to single propeller aerodynamics

The most important contributions to today's understanding of propeller aerodynamics were formulated at the turn of $20^{th}$ century. A review paper on rotor theories [11] divides the historical efforts geographically to three important regions of influence. In Great Britain, the most well-known scientists researching theory connected to propellers, were Rankine, Freude and Lanchester. In Germany, propellers were studied by Prandtl and his follower Betz and in Russia it was Joukowsky and his pupil Vetchinkin.

It is appropriate to mention here, that most of the theory, experimental findings and conclusions, applicable to propellers, are also applicable to horizontal axis wind turbines and vice versa. For this reason some articles that are referenced in this thesis are from the field of wind energy.

The first problem consisting of flow through a rotor with infinite number of blades was successfully solved using the actuator disc theory. This amazingly simple yet powerful theory could solve such problems as the maximum power extracted from wind (Betz limit) or the maximum thrust of an ideal propulsor.

The actuator disc theory could not help much with the design and analysis of real propellers with finite number of blades. In order to overcome this limitation, blade element method together with vortex methods evolved to a useful form just before the second World War [12].

Interest in the field of open rotor aerodynamics was fading after WWII with the invention and spread of jet engines. A renaissance of the research in this topic began with the fuel crises and related onset of wind energy popularity at the end of the last century.

Nowadays, a new field of use of refined computational models of rotors can be also seen in the optimization of UAV propellers, which can be observed by the rising amount of scientific papers on this topic.

## 2.2 Propeller geometry

The most important parameter of a propeller is its diameter $D$, which is twice the distance between the tip of the longest blade and axis of rotation. The area defined by this diameter is the propeller disc area $A_D = 0.25\pi D^2$. For the purpose of this work, only rotor consisting of a finite number $N_b$ of blades with identical geometry is assumed. Propeller blade geometry can be fully described in terms of chord length distribution (blade width) $b(r)$, incidence angle (blade twist) $\beta(r)$ and 2D airfoil section geometry distributions along the span of the blade. Blade span coordinate $r$ reaches zero at the axis of rotation and $r = R$ at the blade tip.

Manufacturers of propellers define a global parameter called pitch $d_p$, which is often described as "Distance that the propeller covers in one rotation". This definition is associated with propeller geometry and the motion of screw cutting through solid material [13]. When the blade is idealized as part of a helicoidal surface, the pitch can be calculated as $d_p = 2\pi r\, tan(\beta(r))$. It is immediately clear that for a propeller with arbitrary incidence angle distribution, pitch will vary with radius. Special case is the constant pitch propeller, with constant pitch along the blade span. Manufacturers designate their propellers with a single value of pitch using $Diameter \times Pitch$ notation so the pitch at a characteristic relative radius $r/R = 0.75$ is used [13].

Distance that the propeller covers in one rotation relative to the moving air during flight is usually lower than the geometric pitch and depends on many factors. In reality manufacturers of small UAV and model aircraft propellers often significantly underestimate the nominal pitch of their propellers compared to their geometry probably due to the fact that users tend to compare the propellers with the same pitch designation using only thrust criteria, with only few measuring also torque or the flight time. Real pitch distributions were measured and documented in author's work [A 1].

A variable pitch propeller is a propeller with blades that can rotate around their span axis. This way the overall propeller pitch can be controlled by the pilot or automatically by various mechanisms. Because the blade is rigid, optimum pitch distribution along blade span occurs only for a certain advance ratio and pitch setting combination, which often happens to be the propeller's design point. In presented work, variable pitch

propellers are not being analyzed or considered. They can be treated as a series of different fixed-pitch propellers.

## 2.3 Propeller performance

Performance of a propeller can be calculated using various numerical methods or measured in a wind tunnel. The operational conditions are defined by density $\rho$, free stream velocity $c_\infty$, propeller angular velocity $\Omega = 2\pi f$ and angle of the free-stream relative to rotation axis $\varphi$. In most experimental studies of fixed wing aircraft propulsion, angle $\varphi$ is chosen zero or a small value simulating thrust angle and angle of attack of the aircraft. In helicopter research, on the other hand, $\varphi$ can reach values between 0° and 180° where $\varphi = 90°$ indicates forward level flight.

For given operational conditions, thrust $T$ as the force in the direction of axis of rotation and torque $Q$ are measured.

To better asses the performance of propellers, non-dimensional values of advance ratio $\lambda$, thrust coefficient $c_T$, torque coefficient $c_Q$ and power coefficient $c_P$ can be defined as follows [14]:

$$\lambda = \frac{c_\infty}{\Omega R}, \tag{2.1}$$

$$c_T = \frac{T}{\rho f^2 D^4}, \tag{2.2}$$

$$c_Q = \frac{Q}{\rho f^2 D^5}, \tag{2.3}$$

$$c_P = \frac{P}{\rho f^3 D^5}. \tag{2.4}$$

$$\tag{2.5}$$

Other definitions of these dimensionless parameters exist in literature that can differ by a constant, so care must be taken in comparisons. Efficiency can be expressed in terms of these coefficients as:

$$\eta = \frac{T c_\infty}{P} = \lambda \pi \frac{c_T}{c_P}. \tag{2.6}$$

Swirl losses are caused by the tangential velocity in the wake, which does not produce any useful work. The power lost due to swirl losses can be derived from the kinetic energy of the rotating wake and is calculated according to Eq. (2.7).

$$P_{swirl} = \frac{1}{2}\rho \int 2\pi r c_a {c_\theta}^2 dr. \tag{2.7}$$

Propeller Reynolds number is based on the blade chord $b$ at characteristic radius $r/R = 0.75$ and local relative velocity $c_{rel}$:

$$Re = \frac{c_{rel} b}{\nu}. \tag{2.8}$$

## 2.4 Research of single propellers performed by simple computational methods

### 2.4.1 Momentum theory

Momentum theory is a 1D rotor theory based on the concept of an actuator disc with a pressure jump across its surface. An actuator disc is in fact a propeller with infinite number of blades which produces no swirl velocity in the wake.

The actuator disk theory (or momentum theory) is most often attributed to Freude [15], who did not invent the idea of an actuator disc, but who first correctly predicted, that half of the fluid acceleration occurs in front of the disc, while the other half of acceleration occurs behind. It took several more decades before this idea was widely accepted [11]. The actuator disc is in some literature [13] described as ideal propulsor.

The velocity far away upstream of the propeller is equal to free stream velocity $c_0 = c_\infty$. As the flow approaches the actuator disc, the velocity increases until it reaches the maximum value $c_2$ far downstream of the propeller (See Figs. 2.1, 2.2). At the propeller disc, the velocity can be calculated as $c_1 = 0.5c_0 + 0.5c_2$. The stream tube area $A$ has to satisfy continuity equation. Its cross section is indirectly proportional to the velocity. Pressure in the streamtube passing through the disc is atmospheric far upstream, decreases all the way to the disc, where it receives a sudden increase above the atmospheric pressure. Pressure behind the actuator disc slowly decreases to atmospheric level in a sufficient distance.

The thrust $T$ of an actuator disc can be found from the change in momentum of the accelerated fluid.

$$T = \dot{m}(c_2 - c_0). \tag{2.9}$$

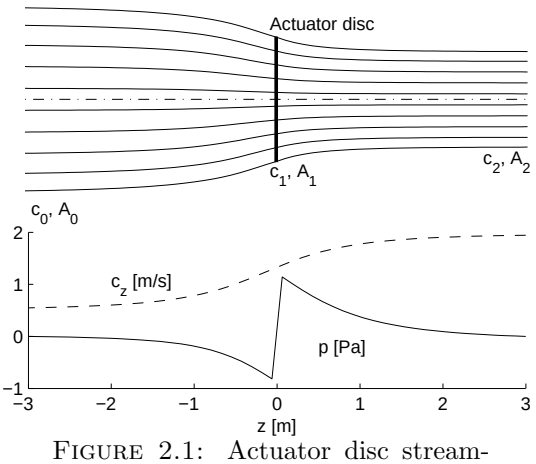


FIGURE 2.1: Actuator disc streamtubes, non-zero free stream velocity.

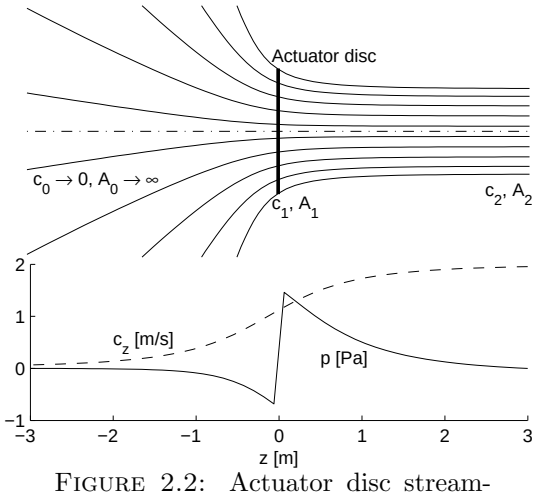


FIGURE 2.2: Actuator disc streamtubes, zero free stream velocity.

The power $P$ required for this thrust can be written based on the change in kinetic energy as [13]:

$$P = \frac{1}{2}\dot{m}(c_2^2 - c_0^2) = Tc_0 + \frac{1}{2}\dot{m}(c_2 - c_0)^2. \tag{2.10}$$

From the second form of expression for power, it can be seen that the power input to the ideal propulsor (actuator disc), can be divided into useful thrust power $Tc_0$, which accommodates the propulsion, and power needed for accelerating the flow $0.5\dot{m}\Delta c^2$. It becomes apparent from these formulas that propulsion efficiency can be calculated as the ratio of useful thrust power to the total power input.

$$\eta = \frac{Tc_0}{0.5\dot{m}(c_2^2 - c_0^2)} = \frac{2}{1 + \frac{c_2}{c_0}} = \frac{c_0}{c_1}. \tag{2.11}$$

The propulsion efficiency can be only increased by approaching $c_2 \to c_0$, which is equivalent to $c_1 \to c_0$. This is practically achieved by lightly loaded large diameter propellers. High efficiency of large propellers is outweighed by high structural weight, large angular momentum, the need of higher undercarriage and limited maximum operational flightspeed.

An important regime of the propulsor is the static thrust regime, where the propeller does not produce any useful work from propulsion point of view, but can accelerate quantity of air to produce thrust, which can be also quite useful (helicopter or multicopter drone in a hover).

The power of ideal propulsor in static thrust (based on Eq. (2.10)) is determined according to Eq. (2.12).

$$P_0 = \frac{1}{2}\dot{m}(c_2)^2 = \frac{1}{2}\rho A_1 c_1 (2c_1)^2 = 2\rho A_1 c_1^3. \tag{2.12}$$

At the same time, static power can be expressed based on thrust and flow rate at the propeller disk as $P_0 = c_1 A_1 \Delta p = c_1 T$. Putting these two formulas together, the power of ideal propulsor based on its thrust can be expressed as:

$$P_0 = \frac{T^{3/2}}{\sqrt{2\rho A_1}}. \tag{2.13}$$

To evaluate the efficiency of real propellers producing thrust in static regime, term Figure of Merit or "static efficiency" $FoM$ is used. Figure of Merit is the ratio of static power of the ideal propulsor at the same thrust as the analyzed propeller to the input power of the analyzed propeller:

$$FoM = \frac{T^{3/2}}{P\sqrt{2\rho A_1}}. \tag{2.14}$$

### 2.4.2 Extending actuator disc theory to 3D flow

1D actuator disc theory can answer elementary questions, such as the relations of the velocity at the propeller and in the far field and establish formulas for calculating maximum thrust and propulsion efficiency of a propeller. Often it is useful to extend the theory to three dimensions. Actuator disc is a rotor with infinite number of blades infinitesimally wide, with even load distribution. This means, that the power density (defined as input power per propeller disc area) over the whole disc is constant, which can be satisfied only with constant circulation distribution over the blade span. Since an ideal propulsor should not produce any tangential velocity in the wake, helical vortices shed by the blades reduce to a cylindrical surface of evenly distributed vortex rings [14]. This surface can be modeled by discrete vortex rings (see Chapter 5 ) and the result is in Fig. 2.3.

### 2.4.3 Blade element method

Blade element methods are methods based on the blade element theory which is often attributed to Stepan Drzewiecki [12] but appears in some form also in the work of Freude and others at that time. The main idea of the theory is very simple. Each blade of the rotor is represented as the sum of separate elements - blade sections. For each blade section the angle of incidence, chord length and relative velocity to undisturbed flow is

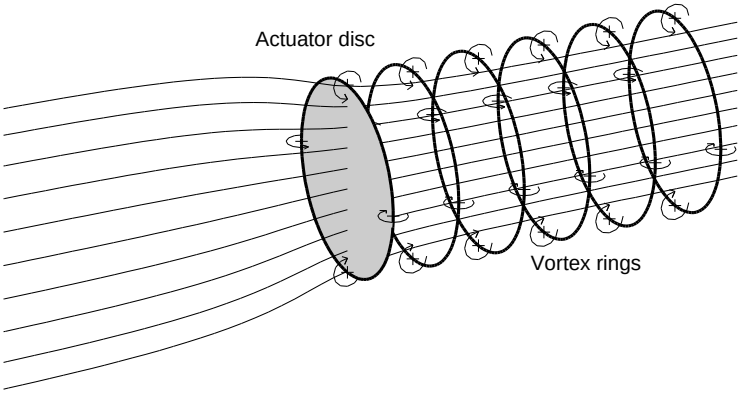


FIGURE 2.3: Simulating actuator disc by a set of equidistant vortex rings.

known. The flow at each blade element is treated as a 2D flow around an airfoil with the same angle of attack. By summing the forces acting on the elements, total thrust force and torque is obtained.

The blade element theory gives incorrect results if the induced velocity is not correctly predicted or even neglected, as was the case of early adopters of the method. When momentum equations are used to determine the induced velocity, the method is often called blade element momentum method (BEM). When a vortex wake is used to determine the induced velocity, the method is named in this work according to the mechanism of creating vortex wake i.e. lifting line or lifting surface, which will be described in the next section.

Velocity triangles of a blade element are in Fig. 2.4. The relative velocity $c_{rel}$ is composed of the rotational component $c_{rot}$ and free-stream velocity in the axial direction $c_\infty$. The angle between this relative velocity and chord line is the angle of attack $\alpha$ that does not include induced velocities and is not used for computation. The induced velocity $c_i$ has an axial $c_{i,z}$ and a small tangential $c_{i,t}$ velocity component. By adding the induced velocity to the relative velocity, the effective relative velocity $c_{eff}$ and effective angle of attack $\alpha_{eff}$ are calculated.

### 2.4.4 Lifting line method

The lifting line methods are based on the Prandtl lifting line theory, that has been widely accepted and described in many low speed aerodynamics text books [16], [17]. The theory was first derived for the case of a symmetric finite wing, however, generalization to a rotating blade followed soon.

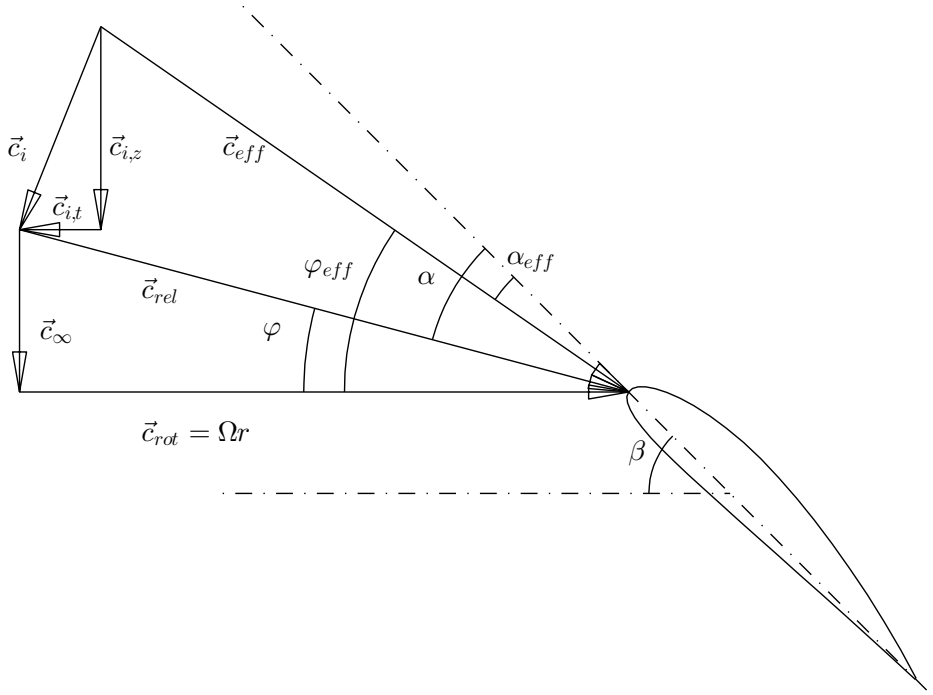


FIGURE 2.4: Velocity triangles of a blade element.

A finite wing is replaced by a bound vortex in the spanwise direction reaching from one wing tip to the other. The circulation strength of this vortex is set to be the same as the circulation of the respective airfoil sections. Since the distribution of circulation over the span is not constant, vorticity equivalent to the change of circulation between wing sections is shed into the wake. An assumption that allows simple solution for wings is that the trailing vortices forming wake are straight lines parallel to the free stream. The theory gives accurate results for wing aspect ratios $AR > 4$. For lower aspect ratios, the circulation distribution along the wing chord starts to play an important role and different approaches such as lifting surface or 3D panel methods are needed. Glauert presented one of the earlier solutions to Prandtl's equations, which is described and used in Chapter 6.

An analytic approach is much more difficult for propeller vortex wakes, since instead of straight vortex filaments, helical vortices are needed. There have been many attempts to obtain usable analytic formula for induced velocity of helical vortex filaments. The resulting formulas are very complex, use more or less severe aproximations and as such are used very seldomly nowadays. For additional information, see [12]. Fortunately, with current computational power, it is possible to effectively discretize the wake by large amount of straight elements (It is done in Chapter 6).

The shape of the wake is often used to define maximum efficiency. Maximum efficiency

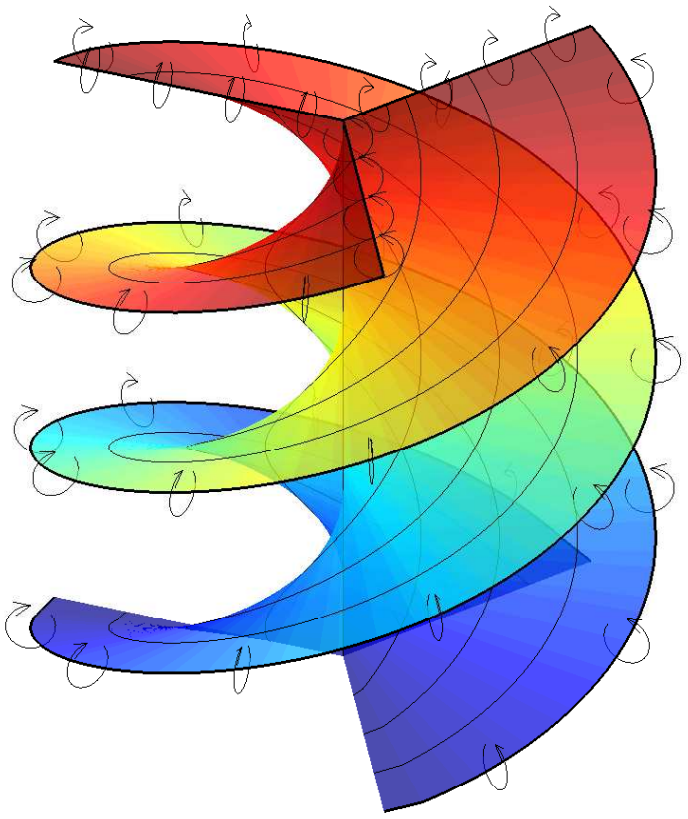

FIGURE 2.5: Helical vortices behind 3 bladed propeller.

at a given thrust is attained when the pitch of the trailing vortices is constant and the force-free wake has a shape of an undeforming regular helicoidal surface [14].

### 2.4.5 Lifting surface method

Lifting surface methods represent a family of methods where the lifting body is discretized by a number of vortex segments placed along the chord line or camber line. The influence of the lifting body's thickness is neglected. A boundary condition is solved at collocation points. Sometimes, lifting surface methods are called vortex lattice methods due to the geometry representation of the lifting body by a lattice of vortices. Overall the method is similar to the 3D panel methods, requiring less panels. It has been used widely before the 3D panel methods become realizable due to computational power increase in the history. It is ideal for quick analysis of low aspect ratio or highly swept wings and also for marine propellers, which have very wide and thin blades. One such early example of a lifting surface panel method is that of Kerwin [18] describing a vortex lattice computational code written in FORTRAN and optimized for the computing machines of that time.

## 2.5 Research of single propellers performed by complex computational methods

### 2.5.1 3D panel methods

An interesting trend can be seen in the use of 3D panel methods for propeller analysis. Almost no reference can be found about the use of 3D panel methods for aircraft propeller design or analysis, on the other hand it is a quite popular tool for marine propeller analysis. An article by Hess and Valarezo [19], describing early panel method for propeller analysis, uses both marine and aircraft propellers for verification. Hess and Valarezo stated that their work seemed to be the first application of panel method on propellers. After this work, the amount of marine propeller research performed using 3D panel methods skyrocketed. The following two examples bring some significant enhancements to the model.

Ching-Yeh Hsin in his doctoral thesis at MIT [20] focuses on an efficient and robust panel method for marine propellers in unsteady flow. The main topic of his work is removing some drawbacks of previous methods developed at MIT, especially the inability to model highly skewed propellers. Emphasis is also given to unsteady model of the wake, since obtaining vibratory forces for shaft and stern bearing design is of high importance. Still the developed method would need modifications to be applicable to a CRP problem.

The impact of using a proper boundary layer model instead of some viscous corrections for propeller analysis is described by Takinaci and Atlar [9]. The authors use turbulent model of Cebeci and Bradshaw without any coupling between boundary layer and inviscid flow. To overcome the difficulty with adverse pressure gradients, velocity smoothing process is applied when required. The recommendation by Takinaci and Atlar to use 3D panel methods together with boundary layer was not implemented by other authors in the field of propeller analysis methods. Although practical implementation of such combination was not found, coupling of a 3D method and a 3D boundary layer has been acomplished by Milewski [21]. The resulting complex method was tested on swept finite wing and does not include transition mechanism.

### 2.5.2 CFD solvers

It is beyond the scope of this thesis to describe Navier-Stokes equation solvers which are the main branch and sometimes even synonym for Computational Fluid Dynamics. Only some aspects of using CFD solvers for simulating contra-rotating propellers, that need to be considered, are mentioned.

Using Reynolds-Averaged Navier Stokes solver is the most widely used approach for CFD analysis of propellers. The other options include large eddy simulation, detached eddy simulation or direct simulation. RANS turbulence models such as k-$\omega$ SST with fine wall mesh to discretize boundary layer properly usually produce acceptable results regarding flow separation at maximum lift. Due to lower mesh density requirements and high robustness, k-$\epsilon$ turbulence model is often used as well.

One of the issues, connected to CFD solvers, is producing suitable mesh with sufficient chordwise and spanwise mesh density, with the specified number of cell nodes well within boundary layer (to keep $y^+$ wall distance as required by turbulence model). The surface of the propeller needs to be wrapped with several layers of very fine mesh before the mesh can smoothly transition to a coarse mesh. Cell number of the order of millions is usually required for meshing one rotor in a small cylindrical domain.

A CRP setup can be made by stacking two domains containing first and second propeller and embedding this set in a third very large domain. Using sliding mesh technique with unsteady solver is a necessity. Only small amount of rotation between time steps can be used and several iterations per time step are generally required. A proper unsteady CRP simulation could typically contain a mesh with 10 million cells, and would require over 100 000 iterations. While many simplifications can be made, CFD has seen only limited use in the analysis or even optimization of propellers, although the trends towards using CFD codes are more and more evident. Especiallly in case of single rotor, which can be often computed using steady solvers, the solution time becomes managable.

An interesting comparison of CFD and 3D panel method results for single ship propellers is that of Brizzolara et al. [10] (no similar study for aircraft propellers was found). In their study, unstructured polyhedral mesh with trimmed type of cells is used to produce $y^+$ values quite below 100 for solution using k-$\epsilon$ turbulence model. To lower the computational time the authors took advantage of periodicity and modeled only one blade. The resulting mesh had only $8 \cdot 10^5$ cells which was sufficiently low number to produce a larger series of computations on different propellers. Both methods agree well with the experimental data, except of some small regions of the blades, where, as authors noted, the boundary layer thickness affects the pressure field and RANS solver provides more accurate results. The authors suggest that the panel method should be coupled with thin boundary layer, which is also one of the topics of this thesis.

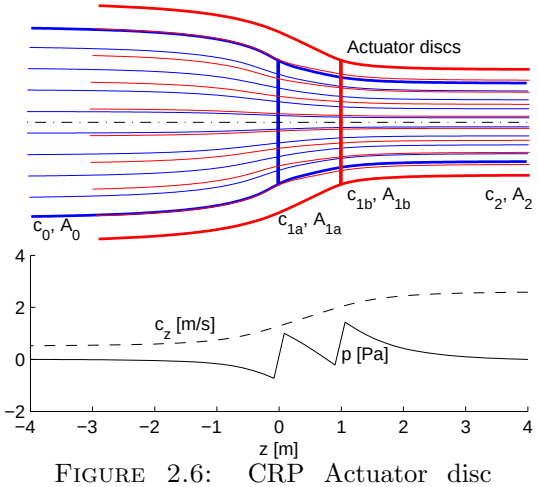


FIGURE 2.6: CRP Actuator disc streamtubes, non-zero free stream velocity.

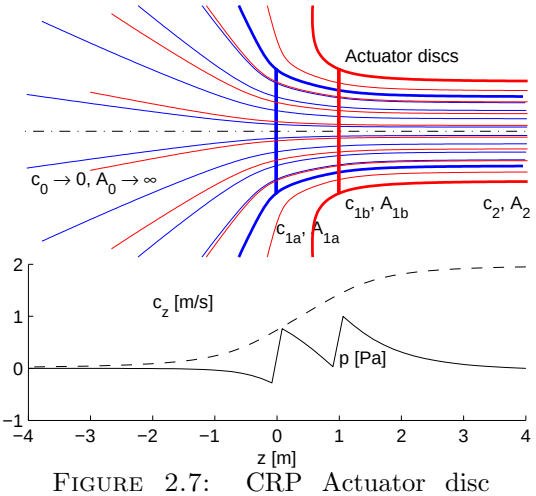


FIGURE 2.7: CRP Actuator disc streamtubes, zero free stream velocity.

## 2.6 Introduction to CRP aerodynamics

Contra-rotating propellers introduce much more complex aerodynamic phenomena compared to the operation of a single propeller. Both CRP system propellers operate in unsteady conditions, which is especially significant for the blades of downstream propeller, which intersect the wakes of the upstream propeller with frequency $f_{int} = N_{b1}(f_1 + f_2)$. The upstream propeller is influenced to a lesser extent by the bound vortices of the downstream rotor and its wake system. The propeller distance plays an important role in the aerodynamic load distribution between the upstream and downstream rotor and also plays an important role in the generation of noise.

### 2.6.1 Momentum theory of CRP

A quick way of analyzing the behaviour of contra-rotating propellers is to use the actuator disc theory. In case of uniform "1:1" thrust distribution between the rotors, there are two pressure jumps of same magnitude in axial pressure distribution. In case of both rotors having the same diameter, the downstream rotor accelerates air that previously passed through the upstream rotor, but also sucks in the air that did not go through the upstream propeller disc as can be seen in Fig. 2.6 and 2.7. As the propeller distance decreases, the portion of additional air sucked by the downstream rotor also decreases. The limiting and very theoretical case of two thin contra-rotating propeller discs with zero distance converges to the single propeller solution.

### 2.6.2 CRP efficiency and performance

The efficiency of a set of contra-rotating propellers can be defined by the same formula (2.6) as in case of a single propeller.

A controversial issue often dicussed in literature is comparing the efficiency of a CRP system with that of an equivallent single propeller or in some cases of two propellers operating side by side. Due to the relation between efficiency and area of an ideal propulsor, operating two side-by-side propellers of the same diameter as the CRP propellers or a single propeller with disk area obtained as sum of CRP propeller disk areas almost always results in a greater efficiency than in case of a CRP unit. This can be explained by the results in Fig. 2.8, which show that propulsion efficiency rises considerably with increasing disk area for the same thrust.

More common approach compares the efficiency of a CRP system with a single propeller with disk area equal to the area swept by the larger of the two contra-rotating propellers.

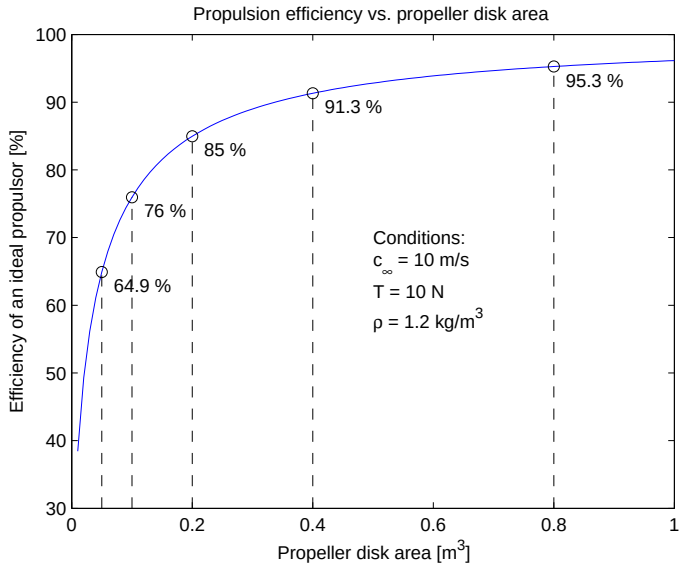


FIGURE 2.8: Efficiency of an ideal propulsor when its area is doubled.

The Figure of Merit definition for CRP systems is discussed in detail by Leishman and Ananthan in [22]. The author concludes, that "fundamentally, any definition of FOM can be adopted, as long as the definition is used to compare like-with-like" and presents a new FOM definition that takes into account relative thrust sharing of the two rotors and unequal disk loadings. For the purpose of this work, the following definition of FOM is used:

$$FoM = \frac{(T_1 + T_2)^{3/2}}{(P_1 + P_2)\sqrt{2\rho\, max(A_1, A_2)}}. \tag{2.15}$$

Since the individual CRP propellers can have different diameters and different rotational rates, the following definitions of dimensionless parameters are used (index 1 indicates parameters of upstream propeller, index 2 indicates parameters of downstream propeller):

$$c_T = \frac{T_1 + T_2}{\rho 0.25(f_1^2 + f_2^2)(D_1^4 + D_2^4)}. \tag{2.16}$$

$$c_Q = \frac{Q_1 + Q_2}{\rho 0.25(f_1^2 + f_2^2)(D_1^5 + D_2^5)}. \tag{2.17}$$

$$c_P = \frac{P_1 + P_2}{\rho 0.25(f_1^3 + f_2^3)(D_1^5 + D_2^5)}. \tag{2.18}$$

$$\tag{2.19}$$

## 2.7 Numerical research of CRP

Blade element momentum method is used in the detailed analysis of contra-rotating propellers by Leishman and Ananthan [22]. An important contribution of their paper is the discussion on the topic of correct Figure of Merit definition. It states that maximum Figure of Merit is obtained for uniform disc loading at balanced torques. According to the blade element momentum theory, optimum twist distribution for the lower (downstream) rotor has a sudden jump at such radius, where the streamline from the upstream rotor tip passes. Only hover and axial flight are concerned since other modes of flight are not predictable by BEM. The paper also compares the results of a BEM calculation and a finite volume method, and highlights the ability of BEM method to predict CRP performance at the fraction of calculation complexity of finite volume method. A similar approach is used by Rand and Khromov [7] to find an optimum rotor design for hover and axial flight using real lookup tables for lift and viscous drag.

A recent (2011) CFD study focused on a coaxial helicopter rotor in forward flight by Heyong and Zhengyin [23] uses unsteady Euler solver on an unstructured dynamic overset grid. The study does not take into account viscous forces neither it attempts to calculate power or torque coefficients. The outcome was, that CRP setup in this scenario reduces performance compared to single rotor. This claim is based on findings, that a single rotor provides greater thrust than the pair of CRP rotors. It is questionable to draw such conclusions without the information about power input. Such articles highlights the importance of using suitable parameters for comparison, such as it is demonstrated in [22].

Vorticity transport model developed by Brown is used in a paper by Kim and Brown [24] to calculate hover, forward flight and maneuvers of a helicopter coaxial rotor system. The computational model is based on the time-dependent solution of the vorticity-velocity form of Navier-Stokes equations. A convection algorithm helps to preserve vortical structures and prevents numerical dissipation. Adaptive grid system is used, which refines the mesh in presence of vorticity and destroys cells once the vorticity has moved away.

The research of literature revealed that the main domain of contra-rotating propellers is the use in marine application as a propulsion system of ships. The findings about CRPs in the field of naval engineering are to some extent transferable to aerospace applications, therefore they have been included in the research. There are two basic differences in modelling of a CRP system for ship and for aircraft. The geometry of a marine propeller includes much wider blades resulting in very high blade solidity. Due to this, lifting line approach is not suitable and lifting surface or panel methods are quite common methods for this application. On the other hand, lifting line is quite suitable for slender airborne blades. Second difference is the issue of cavitation, which needs to be solved only in case of marine propellers, while for aircraft propellers, a different phenomenon - compressibility effects - plays an important role at higher velocities.

Yang et al. [25] used lifting surface in their early work (1992) on contra-rotating ship propellers. The wake is modeled using relaxation method, where the averaged induced velocity of both propellers is used to define the pitch of the trailing wake system. The authors conclude, that although the obtained results are satisfactory, further studies on the trailing vortex interaction are necessary.

Ghassemi [8] in his work describes a software package SPD (Ship Propeller Design) that uses panel method with hyperboloidal quadrilateral elements to model CRP. The method calculates thrusts and torques without including viscous forces. Only 2-3 percent of increase in efficiency was obtained using the CRP system for the studied case compared to single propeller.

A very recent (2015) and detailed study by Paik et al. [26] compares the results of wake development behind ship CRP setup calculated by CFD RANS unsteady solver and results of Stereo PIV measurement. The study focuses mainly on the position and development of blade tip vortices. Satisfactory agreement has been obtained regarding the position of the aft propeller tip vortex. The vortex from forward (upstream) propeller tip almost disappeared in the wake. The computations were carried out using commercial software Fluent.

It is typical that for potential flow methods (such as BEM method, lifting surface method or 3D panel method) the authors of research papers use in-house developed codes of various complexity, while for CFD studies, commercial software packages are the norm. One reason is, that to this date, only few commercial packages exist that take advantage of potential flow methods.

## 2.8 Experimental research of CRP

In the field of airspace CRP usage, only limited number of experimental studies were published, mostly concerning helicopter rotors. Full scale tunnel test as early as 1951 were performed in Langley [27]. The results of hovering performance were compared with numerical methods of that time. Pair of 7.6 m diameter two bladed rotors with rotor distance 9.5% $D$ had NACA four digit symmetrical airfoils used on an untwisted rectangular blade. The coaxial shafts were powered by a 198 kW motor. The maximum $FoM$ for a coaxial rotor was determined to be 0.635 while for single rotor it was 0.615. Three years later, a similar research [28], which included also vizualisation, confirms improved hovering efficiency of a CRP system, but notes that more power is required for level flight than in case of equivalent single rotor. Comprehensive overview of coaxial rotor helicopter experimental research, mostly by the helicopter manufacturers, is given in [1].

The above full scale measurements are quite complex and offer very precise and robust data, however small scale measurements are often the only cost-sensible option. An experimental study about hover performance of single, tandem and coaxial rotors [3] shows a very viable solution of the measurement setup. This paper among others lists the parameters of other previous experiments on this topic. The measurement confirmed, that overall performance is not very sensitive to propeller distance, but the load distribution between rotors changes with propeller distance. CRP system was found to have a 9% higher $FoM$ than an equivalent single propeller, on the other hand CRP system showed 20% increase in induced power compared to a pair of isolated single rotors. It was found that the upper rotor influenced the lower rotor even in case of large distance between the rotors. The lower rotor influences the upper one only at a close distance, at distances over 0.75 D the influence is not measurable.

A different configuration, with motors and support structure placed between the rotors, is presented in an article by Huo et al. [29]. The rotor was equipped with a long shroud. The performance of both rotors and the shroud were measured individually. Similar experimental setup as of Huo et al. but without shroud is used by Simoes [30] who

measured performance of a coaxial system with 14x4.7 propellers. The author compared the two propellers in identical and opposite direction of rotations (yet using left vs. right handed version of the same propeller was not mentioned). Unexpectedly, the author comes to conclusion based on measurement results that identical rotation direction provides similar thrust at the same input power level as opposite direction and by measuring temperature of the electric motors, he determined that propellers rotating in the same direction were a better option. Rest of the paper describes various experiments with coaxial propellers which are rotating in the same direction. When compared with only single propeller, the measured coaxial system showed lower performance, with only benefit being a faster response time, which is beneficial for a multicopter. These results are in disagreement with outcomes of others, which could be either due to erroneous measurement or strong influence of low Reynolds numbers.

As in case of numerical studies, large portion of experimental research on CRPs concentrates on marine applications. A paper about experimental determination of unsteady forces on contra-rotating ship propellers [31] describes a six-component propeller dynamometer and measurement procedure, as well as results of test. A significant simplification was obtained by measuring parameters of one propeller at a time, with swapping the dynamometer between the shafts during break between measurements. An interesting problem arose in this research. It was found that the speed control of the two independent shafts was inadequate, and large phase angle variations were observed, due to the unsteady nature of the problem.

## 2.9 Conclusions

In existing literature, minimum attention is paid to low Reynolds number flow in aircraft contra-rotating propellers ($Re < 5 \cdot 10^5$ occuring in propulsion of UAVs). Moreover, none of the methods described in the review fully respects the viscous character of complex unteady flow in low Reynolds contra-rotating propellers. Very capable method, as illustrated by frequent use on marine propellers analysis, is a 3D panel method. One advantage for CRP analysis is surface discretization of full geometry of blades which can capture the entry and passing of a downstream blade through an upstream blade's wake. Reasons why 3D panel methods are quite commonly used for marine propeller analysis and not for aircraft propellers are not clearly stated by any of the authors reviewed. It can be attributed to the following reasons:

- Low aspect ratio of marine propeller blades: Simple computational models can be sufficiently accurate for high aspect ratio blades of aircraft propellers whereas they

fail to accurately solve low aspect ratio marine propellers with high component of radial velocity.

- Considerable viscous losses in aircraft propellers: Viscous losses play an important role in aircraft propellers. Boundary layer implementation into 3D panel method is complicated as opposed to using 2D polars with BEM methods or similar. In marine propellers, viscous losses are less significant due to high Reynolds numbers and high blade tip losses.

- Compressibility effects in aircraft propellers: Tips of aircraft propellers often reach very high subsonic Mach numbers, where simple compressibility corrections, easily applicable to 3D panel methods, are not sufficient.

Review of results of CRP research done by various authors brings more questions than answers. Topic of comparison of CRP system to equivalent single propeller emerges in several studies with various results. Contra-rotating arrangement seems to be advantageous in hover, but results of coaxial helicopter studies suggest poor performance in forward flight. The effect of free-stream velocity direction on performance is very important for multicopter operation and should be studied in detail. Very comprehensive set of results calculated by BEM method [22] indicates response of CRP system to various changes, however the method itself does not reflect viscous effects, wake shape, unsteady character of flow, blade-wake interactions and other phenomena. It would be beneficial to undertake sensitivity studies of similar extent using more complex model.

# Chapter 3

# Potential Flow Theory and Related Methods

In order to use potential flow theory in a computational method, it is necessary to describe selected properties and fundamental principles of potential flow.

## 3.1 Potential flow

### 3.1.1 Circulation and vorticity, Helmholtz's theorems

For the purpose of describing the properties of the flow field, two quantities, circulation and vorticity, are defined:

**Vorticity** $\vec{\omega}$ (curl of velocity) is a vector field obtained by applying the curl operator on a velocity vector field. For a 2D flow field, the vorticity vector is always perpendicular to the plane of the flow and vorticity can be treated as a scalar. Vorticity is a local property of the flow. If the flow has zero vorticity, it is called irrotational flow. An example of such flow is a potential flow.

$$\vec{\omega} = \nabla \times \vec{c}. \tag{3.1}$$

Vorticity should not be intuitively connected to rotational motion of the particles. As an example, viscous parallel flow between two walls moving at different velocity will introduce nonzero gradient in the velocity profile and therefore non-zero vorticity. Another example of such shear layer is a boundary layer next to a solid body, where non-zero

vorticity is also present. On the other hand potential vortex has zero vorticity (except its singularity point - core, where properties are not defined)

**Circulation** $\Gamma$ (of velocity) is defined as a line integral along a closed curve $C$ placed in the flow field. It is a scalar quantity. By applying Stokes' theorem the circulation can be also expressed as the vorticity flux through a surface bound by a closed curve.

$$\Gamma = \oint_C \vec{c} dl = \iint_S \vec{\omega} \cdot \vec{n} dS. \tag{3.2}$$

An important conservation law is connected to circulation - Kelvin's circulation theorem is valid for flows with absence of viscous stresses (such as potential flow):

$$\frac{D\Gamma}{Dt} = 0. \tag{3.3}$$

In a similar manner as streamlines and streamtubes are defined for velocity vector field, analogous structures can be defined for vorticity field. The curves tangent to the vorticity vectors are called vortex lines which, if they pass through a closed curve, can form together a vortex tube. A vortex tube of infinitesimal cross-section is called a vortex filament, which is a cornerstone of many numerical models. The Helmoltz's theorems for inviscid incompressible flows describe the behavior of vortex structures and can be summarized as follows [16]:

- The strength of a vortex filament is constant along its length.
- A vortex filament cannot start or end in a fluid (it must forma closed path or extend to infinity).
- The fluid that forms a vortex tube continues to form a vortex tube and the strength of the vortex tube remains constant as the tube moves about.

### 3.1.2 The potential flow equation

Potential flow is an inviscid irrotational flow which can be expressed by Laplace's equation:

$$\nabla^2 \phi = \Delta \phi = \frac{\partial^2 \phi}{\partial x^2} + \frac{\partial^2 \phi}{\partial y^2} + \frac{\partial^2 \phi}{\partial z^2} = 0, . \tag{3.4}$$

where $\phi$ is a velocity potential, which is a function of space and time. Laplace's equation is an elliptic partial differential equation. Solutions to the Laplace's equation are called harmonic functions.

Another important function in potential flow is the stream function $\psi$, which is defined only for two-dimensional flow (or for special cases of three-dimensional flow, such as axisymmetric flow):

$$\frac{\partial^2 \psi}{\partial x^2} + \frac{\partial^2 \psi}{\partial y^2} = 0. \tag{3.5}$$

The following relations apply for stream function, velocity potential and velocity components:

$$c_x = \frac{\partial \phi}{\partial x}\ , \qquad c_y = \frac{\partial \phi}{\partial y}\ , \qquad c_z = \frac{\partial \phi}{\partial z}. \tag{3.6}$$

$$c_x = \frac{\partial \psi}{\partial y}\ , \qquad c_y = -\frac{\partial \psi}{\partial x}. \tag{3.7}$$

Isocurves of constant stream function are tangent to velocity vectors and form streamlines. The isocurves of constant potential and streamlines are perpendicular everywhere.

Laplace's equation does not contain a pressure term. To obtain information about pressure, it is necessary to use the Bernoulli's equation in the form for incompressible irrotational flow with conservative forces [16]:

$$gz + \frac{p}{\rho} + \frac{c^2}{2} + \frac{\partial \phi}{\partial t} = C(t), \tag{3.8}$$

where $z$ is a coordinate in opposite direction to gravitational acceleration and $C(t)$ is a constant only changing with time.

### 3.1.3 Boundary conditions

To solve the Laplace's equation for a submerged body, boundary condition must be specified at the surface of the body and in the infinity. In the infinity the assumption of vanished induced velocity due to presence of the body must be valid, therefore the total velocity in sufficient distance from the body is equal to the free stream velocity:

$$\lim_{r\to\infty} c = c_\infty. \tag{3.9}$$

This condition is in most cases fulfilled automatically by superposition of suitable singular solutions of Laplace's equation. Impermeability condition is applied on the surface of the body. In every moment the velocity vector on the surface of the body, expressed in the coordinate system fixed to the body, must be tangent to the surface, or zero. This condition is equivalent to the requirement of zero normal velocity on the surface. It is a Neumann type of boundary condition:

$$\frac{\partial\phi}{\partial n} = \nabla\phi \cdot \vec{n} = 0. \tag{3.10}$$

### 3.1.4 The solution of Laplace's equation and boundary conditions using superposition of sigular solutions

There are several methods for solving Laplace's equation. Since Laplace's equation is linear, it is possible to use a linear combination of simple solutions. The most common solutions are the potential vortex, potential source and sink. If a source and sink of the same strength are positioned at a distance approaching zero, they form a dipole (doublet). All of these solutions contain a singular point, thus being referred by the term singular solutions. Another important component of the final solution is a uniform stream, which does not contain a singular point and does not diminish in infinity. The uniform stream is used to create the free undisturbed flow. The method of solution using superposition of singular solutions is based on distributing the solutions in the domain and specifying their strengths in such way, that the resulting solution satisfies the boundary condition. The oldest 2D methods for example placed the singular solutions on the camber line, first 3D methods idealized the wing by a simple lifting line forming the front portion of a horseshoe vortex. The largest success and widespread use has been achieved by panel methods, both 2D and 3D - a method involving distribution of singular solutions over panels forming the surface of the body.

### 3.1.5 Basic solutions of the flow and their properties

#### 3.1.5.1 Uniform stream

Uniform stream contains no singular point and does not vanish towards infinity. It is used to model free stream in the frame of reference connected to the solid body. The formula for calculating the potential takes the following form:

$$\phi(x, y, z) = c_x x + c_y y + c_z z. \tag{3.11}$$

#### 3.1.5.2 Source and sink

Sink is in fact a source with a negative source strength. Therefore, in the rest of the text, sink will be referred to as source. If a point source of strength $\Sigma$ is placed at a point defined by a radius vector $\vec{r}_1$, then the potential at any other point defined by radius vector $\vec{r}$ is defined as follows:

$$\phi(x, y, z) = -\frac{\Sigma}{4\pi\|\vec{r} - \vec{r}_1\|}. \tag{3.12}$$

The induced velocity obtained as the gradient of potential:

$$\vec{c}(x, y, z) = \frac{\Sigma(\vec{r} - \vec{r}_1)}{4\pi\|\vec{r} - \vec{r}_1\|^3}. \tag{3.13}$$

#### 3.1.5.3 Dipole

Dipole (doublet) is formed by two sources of opposite strenghts (i.e. source and sink) in a specific distance. Point dipole is formed when this distance approaches zero. To define the properties of a dipole, it is necessary to specify not only the strength of the dipole, but also its direction, so the strength of dipole is specified as a vector $\vec{\Pi}$. In a similar manner as for point source the potential and velocity of dipole are obtained as follows:

$$\phi(x, y, z) = -\frac{\vec{\Pi} \cdot (\vec{r} - \vec{r}_1)}{4\pi\|\vec{r} - \vec{r}_1\|^3}. \tag{3.14}$$

$$\vec{c}(x, y, z) = -\frac{\vec{\Pi} \cdot (\vec{r} - \vec{r}_1)}{2\pi\|\vec{r} - \vec{r}_1\|^5}(\vec{r} - \vec{r}_1) - \frac{\vec{\Pi} \cdot \nabla((\vec{r} - \vec{r}_1)/\|\vec{r} - \vec{r}_1\|)}{4\pi\|\vec{r} - \vec{r}_1\|^2}. \tag{3.15}$$

#### 3.1.5.4 Vortex

(also free vortex, irrotational vortex or potential vortex) Free vortex is a vortex in a potential flow which complies with the irrotational condition. The particles of the flow follow circular paths but remain oriented in the same direction. In 2D flow the vortex position is defined by its center - singular point - where the irrotational flow condition is

not satisfied. In three dimensional flow the vortex is defined by a vortex filament, where the solution is also singular. In 2D, the potential is calculated based on the orientation angle $\theta$ of the radius vector $(\vec{r} - \vec{r}_1)$ :

$$\phi(x, y, z) = -\frac{\Gamma}{2\pi}\theta. \tag{3.16}$$

The flow surrounding a vortex filament in 3D space is described by Biot-Savart law:

$$h\vec{c}(x, y, z) = \frac{\Gamma}{4\pi}\int_{-\infty}^{+\infty}\frac{d\vec{l}\times\vec{r}}{\|\vec{r}\|^3}. \tag{3.17}$$

Where $d\vec{l}$ is a section of the vortex filament and $\vec{r}$ is a position vector pointing from this section to the investigated point in space. Generally it is not possible to express the potential field around a curved vortex filament analytically, superposition of short straight sections is used instead.

## 3.2 2D panel methods

Although the computational model descibed in Chapter 6 uses three-dimensional panel method, 2D panel method is described here for two reasons. The general methodology of solution is common for both two and three-dimensional methods and furthermore, 2D panel method is used in this work to test coupling of the boundary layer. 2D panel method solves 2D Laplace's equation with a boundary condition. There are many modifications of panel methods. Common to all methods is the discretization of the streamlined body into separate panels (line segments or less often curved segments). The most basic panel methods use point singular solutions only at the panel nodes, but more often the singular solutions are continuously distributed over the length of the panels. Instead of a point source strength $\Sigma$ a continuous distribution of source strength density $\sigma = d\Sigma/dL$ is considered over the panel length $L$. Different formulations of panel methods use different singularity elements or their combinations. The solution using only source panels and uniform flow for example allows the calculation of symmetric flow, but does not provide realistic solution for lifting bodies. Another combination is the uniform stream together with both sources and dipoles, which allows simulation of lift and circulation [32]. Apart from different order of panels (linear segments, quadratic segments) and different type of singular solutions used, 2D panel methods also differ in the order of distribution of the singular solution over the panel length. Most common are constant and linear strength distributions, although higher order methods were also

developed. Last but not least the form of potential flow equation being discretized and form of boundary conditions influence the 2D panel method behavior, precision and suitability for a specific case. The Laplace's equation with velocity potential used together with Neumann boundary condition is one option. Another option is the stream function formulation of potential flow equation. In this case, a Dirichlet boundary condition (constant stream function on the surface) is used. Also velocity formulation, where the velocity components of each singular solution are combined directly, is often used in panel methods. One of the most widespread implementations of 2D panel method is the excellent code XFOIL by prof. M. Drela. Drela describes in a very well written paper [33] the theoretical background of the 2D panel code XFOIL including boundary layer model.

### 3.2.1 Stream function formulation

The panel code XFOIL [33] is based on a stream function formulation of Laplace's equation. Although using stream function is possible only in 2D, it carries some inherent advantages such as very simple boundary condition implementation. The value of the stream function at a point $P$ in the neighborhood of a closed curve $s$ (body) forming e.g. an airfoil is:

$$\psi(x,y) = c_{x\infty}y - c_{y\infty}x + \frac{1}{2\pi}\int \gamma(s)\log r(s,x,y)ds. \tag{3.18}$$

Here, the line integral follows the surface of the body and computes the product of circulation density and logarithm of distance $r$ between the actual location on the curve during integration and point $P$ in space. For numerical calculation the curve is divided into straight segments, panels, with linear circulation density distribution $\gamma_j$. The influence of one panel of length $l$ on point $P$ using the local coordinates $\bar{x}, \bar{y}$ is computed as follows:

$$\begin{aligned}\psi_j(\bar{x},\bar{y}) =& \frac{\gamma_j}{2\pi}\left\{-\frac{1}{2}(\bar{x}-l)\log((\bar{x}-l)^2+\bar{y}^2) - \bar{y}\arctan\left[\frac{\bar{x}-l}{\bar{y}}\right]\right. \\ &\left. +\bar{x} - l + \frac{1}{2}\bar{x}\log(\bar{x}^2+\bar{y}^2) + \bar{y}\arctan\left(\frac{\bar{x}}{\bar{y}}\right) - \bar{x}\right\}.\end{aligned} \tag{3.19}$$

From this formula it is clear, that the influence of the panel at point $P$ depends only on the circulation density and geometry. This influence is in fact a linear combination of geometry influence and circulation density. For the influence of j-th panel on i-th point

it is possible to reformulate the Equation (3.19) into the product of influence coefficient $A_{ij}$ and circulation density.

$$\psi_i(x, y) = A_{ij}\gamma_j. \tag{3.20}$$

The boundary condition of zero normal velocity is forced indirectly by the requirement of constant stream function value on the body surface. This requirement is based on the fact that the surface of a body is also a streamline. For the existence of a unique solution of the system of linear equations, the number of points, where the boundary condition is checked, must be the same as number of unknown circulation densities (i.e. number of panels). These points are called collocation points. The position of the collocation point on a panel depends on the exact formulation of the panel method, most often it is placed at the panel center, but the placement of the point on one end of the panel, or at 1/4 of its length is also possible in some cases.

$$\psi_i(surf) = konst = \psi_0. \tag{3.21}$$

For i=1...N collocation points there are generally j=1...N unknown circulation densities and an additional unknown value of stream function $\psi_0$ on the surface. The i-th equation takes the following form:

$$c_{x\infty}y - c_{y\infty}x - \psi_0 + \sum_{j=1}^{N} A_{ij}\gamma_j = 0. \tag{3.22}$$

**Kutta condition**

When the potential flow equation is applied on a lifting body problem, the flow will separate at a specific point on the body, such that the overall lift is zero. This separation point will generally not coincide with the trailing edge and will move along when angle of attack is changed. When the potential flow around the trailing edge is observed in detail, it shows some unrealistic (approaching infinity) values of velocity. Kutta condition in one of its forms states, that there must be finite velocity at the trailing edge. This condition in a sort of way simulates the effect of viscosity - the flow will not reach unprecedented velocities, but will separate instead. As Hess explains [34], Kutta condition is only a workaround which brings the potential solution closer to the real lifting flow solution. For sharp trailing edges of a wing, the resulting lifting force is surprisingly accurate. For blunt trailing edges, correct application of Kutta condition becomes more difficult. For

some bodies with very blunt or missing trailing edge, it is not practical and appropriate to use potential flow solution at all.

The above system of N equations with N+1 unknowns is completed by the Kutta condition in the form of required zero trailing edge circulation. If the panels are indexed starting at upper trailing edge, continue over the leading edge towards the lower trailing edge node, the Kutta condition becomes:

$$\gamma_1 + \gamma_N = 0. \tag{3.23}$$

This is not the only possible implementation of Kutta condition, other more complex implementations are described by Drela [33], or Lewis [35]. The Kutta condition will be also revisited in the section describing 3D panel methods.

The unknown circulation densities, and stream function value on the surface of the body, can be solved by either direct or iterative solution of the system of equations. Since the fictional internal flow inside the body (airfoil) must be completely still, the circulation density on the surface becomes equivalent to the surface velocity [33]. For the calculation of induced velocity in an arbitrary point outside of the body, it is necessary to compute the influence coefficients of all the panels on the given point in space and then use a linear combination using already known circulation densities to obtain the stream function value at the given point. For induced velocity calculation in case of stream function formulation, it is necessary to differentiate using at least three points in close proximity.

## 3.3 3D panel methods

### 3.3.1 Introduction to 3D panel methods

Hess and Smith were among the first authors to describe a three-dimensional panel method in their work *Calculation of non-lifting potential flow about arbitrary three-dimensional bodies* [36]. In their pioneering work, the surface of a body was discretized by flat quadrilateral panels with constant source density. Each collocation point was chosen carefully as the point, where the induced velocity of the respective panel was perpendicular to its plane. The method used velocity formulation (note, that the only other option is potential formulation, stream function is not defined in 3D). An important contribution of this work lies in the mathematically exhaustive derivation of induced velocities by a quadrilateral flat panel with constant source density distribution.

Ten years later, Hess published a paper [34] extending the theory to asymmetric bodies which produce lift. In the beginning of the paper, Hess notes, that the method he describes is, in fact, an exact solution to the 3D potential flow problem, unlike the other methods of the time, such as lifting line, lifting surface and small perturbation methods. The exactness of the method is described as the ability to reach any level of precision by refining the numerical discretization. The body in Hess 3D lifting method is split into lifting and non-lifting parts, such as wings and a fuselage. The lifting parts must have a trailing edge defined. The panels forming lifting parts contain both linear dipole strength distribution and a constant source strength distributions, while the panels of non-lifting parts contain only sources. In this method Hess places the collocation points simply in a point obtained as an average of corner points coordinates. First, the boundary condition of zero normal velocity in the collocation point is obtained by solving the system of equations for the correct distribution of source strengths. Then the Kutta condition can be fulfilled by an appropriate dipole distribution. The panels are still flat quadrilaterals, which means, that for complex geometries, gap between panels is inevitable. To speed up the solution, the neighborhood of the panel is divided into three regions depending on the distance from panel. In the near-filed, the induced velocity is calculated using the continuous linear distribution of the dipole strength. For the mid-field points, the panel consists of several dipoles. For the points in far field, the panel consists of only one point dipole. Both non-lifting and lifting methods of Hess and Smith gave rise to a number of modified panel codes, which are in some cases used to this date.

In 1974 a very different formulation of panel method has been published by Morino and Kuo [37]. The family of methods, later named after Morino, use a potential formulation, hyperboloidal panels, constant source and dipole distributions and a different form of boundary conditions.

### 3.3.2 Classification of 3D panel methods

- **By the boundary condition implementation:** The boundary condition in form of zero normal velocity $\vec{c} \cdot \vec{n} = 0$ can be expressed directly or indirectly. A detailed review of various boundary conditions is available by Erickson [38].

  *Direct formulation (Hess):* Geometric coefficients of the influence of i-th panel on j-th collocation point take form of velocity components $U_{ij}, V_{ij}, W_{ij}$.

$$\left\{ \sum_j \left( [U_{ij}, V_{ij}, W_{ij}] \cdot \gamma_j \right) + \vec{c}_\infty \right\} \cdot \vec{n}_i = 0. \tag{3.24}$$

*Indirect formulation (Morino):* The geometric influence coefficients of i-th panel on j-th collocation point take form of a velocity potential - scalar $A_{ij}$. As long as the body surface is impermeable, the fictional internal flow inside the body must remain still, which can be enforced by a zero potential inside the body. By displacing the collocation points in the middle of panels a small distance inside the interior of the body, the boundary condition becomes:

$$\phi_{int} = 0. \tag{3.25}$$

An example of production panel codes that use Morino formulation is SOUSSA (Steady, Oscillatory, Unsteady Subsonic and Supersonic Aerodynamics), VSAERO and QUADPAN [38].

- **By the singularity distribution:** The most simple is a point singularity, which is mostly used only for far field induced velocities calculation. The most common distribution is a constant singularity strength density distribution with the advantage of fast implementation and low computational time required. The singularity strength values experience jumps across panels. As a result, precision is impaired, however this shortcoming is more than balanced by the possibility of using more panels. Linear distribution of singularity strengths is less common, but also used. Higher order singularity distributions are not very practical, computationally demanding, and easily surpassed by low order methods with higher panel densities.

- **By the panel geometry:** High order panel methods use quadratic and cubic definitions of the panel surface, but more common are low order panel methods that use either quadrilateral or triangular flat panels. As Smith and Hess note [36], a quadrilateral surface mesh can be easily made structured, on the other hand with triangular elements it is possible to cover a complex body without gaps.

- **By the singularity type:** Dipole (doublet), source, and vortex filament are used as singularity types. Hess proved [34] that a quadrilateral flat panel with a constant dipole distribution induces an equivalent velocity field (and potential) as the same panel with a vortex filament along its edges instead. As a consequence, panels with constant dipole strength distribution can be replaced by a vortex ring panel. In case of symmetric flow, either dipole or source or both can be used. As an analogy to 2D flow, also in 3D a lifting non-symmetric flow must be modeled by dipoles or vortex rings, source panels alone are not enough.

  Using vortex ring panels has also a physical significance, as Lewis points out [35]. A boundary layer is formed in a real flow around a body. Its thickness depends on the flow Reynolds number. By analyzing the velocity in the thin boundary layer,

a circulation of velocity can be discovered. For inviscid flow, characterized by Reynolds number approaching infinity, the boundary layer thickness is approaching zero. This scenario is then equivalent to an infinitesimally thin vortex sheet.

- **According to time dependence:** All panel methods in principle allow the solution of both steady and unsteady flows. Single rotating propeller is an example of a quasi-steady flow, which occurs when the flow around a blade is not a function of the blade position. In this case, steady flow approach can be used directly. In case of unsteady flow such as in contra-rotating propellers, some modifications need to be performed.

- **According to the type of flow:** Most panel methods are designed for external flow. Some modifications also solve internal flow problems. Application of panel methods on internal flow problems in some cases brings some difficult to solve issues with panel leakage and continuity.

### 3.3.3 Kutta condition in 3D

The three-dimensional Kutta condition implementation differs considerably from the 2D implementation. Kelvin's circulation conservation law must be fulfilled, the bound vortex circulation cannot end in the fluid and zero trailing edge circulation must be forced. To lead the circulation away from the wing a system of trailing vortices is shed from the trailing edge. This is in practice performed by either a sheet of semi-infinite vortices connected to the trailing edge, or by a force-free wake sheet composed of vortex ring panels. Either way, the circulation of the wake vortices is calculated as the difference between upper $\gamma_U$ and lower $\gamma_L$ trailing edge panel circulation.

$$\gamma_W = \gamma_U - \gamma_L. \tag{3.26}$$

## 3.4 Conclusions

Information presented in this chapter describes the historical development of different panel codes and their advantages and drawbacks. This leads to the ultimate selection of the variant of 3D inviscid flow solver used in Chapter 6.

Based on the brief review of panel methods, low order panel method is a preffered option, with quadrilateral vortex panels and constant source panels as singularity elements. Direct formulation is more suitable for a complex computational model due to an easier

formulation of boundary condition in a rotating reference frame under the influence of wake induced velocity field. Formulation of Kutta condition for three-dimensional problems stresses the necessity of modeling wake when calculating flow over finite lifting body. Without a proper wake model, 3D panel method cannot provide relevant results. Building and testing of a wake model should therefore precede the implementation of a 3D panel method.

# Chapter 4

# Formulation of Aims and Objectives

The aim of this thesis is to develop a computational model capable of detailed analysis of contra-rotating propellers subject to low Reynolds number flow accounting for various aspect of the flow ignored by other researchers. The aim is also to describe the properties of contra-rotating propellers using such advanced computational model and answer important questions regarding CRP system performance. The formulation of three main objectives is based on the review of literature and is given as follows:

## 4.1 Creating viscous-inviscid interaction model

***Background:*** 3D panel method is a suitable method for detailed CRP analysis thanks to full blade geometry representation allowing realistic blade-wake interactions. Drawback of the method is unavailability of effective viscous inviscid interaction models for coupling of a viscous boundary layer that would allow low Reynolds number flow analysis including modeling of laminar boundary layer, laminar bubbles, and transition and separation detection. Implementation of boundary layer relies on proper viscous-inviscid interaction model and when resolved successfully, it might allow using 3D panel methods for detailed analysis of viscous flow in aircraft propellers.

***Objective formulation:*** Finding a viscous-inviscid interaction model that would allow coupling of an advanced integral boundary model to a 3D panel method. This model must be fast enough to maintain the important advantage over CFD codes - speed of solution.

## 4.2 Creating force-free vortex wake

***Background:*** Induced velocities of vortex wakes in many cases of CRP analysis are averaged across time and space for the purpose of mutual interaction between rotors. The main issue impairing accurate resolving of downstream blade passage through wake of upstream blade is the singularity of solution at the wake surface formed by discretized vortex elements and unphysical velocities near the wake.

***Objective formulation:*** Creating an unsteady force-free wake model compatible with contra-rotating propeller configuration with emphasis on blade-wake interactions, which would allow accurate resolving of instantaneous wake shapes and induced velocity fields.

## 4.3 Describing properties of a CRP system

***Background:*** Unlike in case of marine applications, aircraft contra rotating propellers have been overlooked in numerical and experimental studies. Extensive research has been performed using simpler numerical methods neglecting viscosity, flow separation or free form of the wake shape. Influence of propeller distance on CRP performance and comparison to an equivalent single propeller has been studied using these methods. Practically no research has been conducted on small aircraft propellers in low Reynolds number flow, which are used in the propulsion of small to medium sized UAVs (approximately 1-20kg)..

***Objective formulation:*** Describing properties of a contra-rotating propeller system under low Reynolds number flow regimes, specifically:

- Fluctuation of forces and torques during revolution
- Influence of propeller distance
- Sensitivity to the angle of free stream flow
- Comparison of a CRP system to an equivalent single propeller
- Influence of the ratio of rotational speeds of both propellers

## 4.4 Secondary goals and other planned steps

The following secondary goals and steps are considered necessary or beneficial to the topic:

- Preparing simpler blade representation using proven lifting line approach. This simpler representation could be used as a reference for assessment of the capabilities of the new model.
- Selecting a suitable 2D boundary layer model and verification of its performance. The boundary layer model should handle transition.
- Design of simple experimental setup allowing measurement of small scale CRP systems under static conditions. This is owing to the fact that no suitable data by other authors was found that could be used for numerical model verification.
- Performing various experiments on a CRP system for numerical model verification.
- Performing supplementary measurement of noise spectra in selected cases, which can provide some additional information for CRP evaluation.
- Verification of numerical model using experimental data, including verification of results using case of single propeller.

# Chapter 5

# Vortex Wake Model

Vortex wake model consists of vortex filaments. A 2D vortex and its formations are studied first to obtain relevant infomation about induced velocity field, motion of vortices under self induced velocity and impact of numerical differencing method. Using simple 2D algorithms, tip vortex wake rollup and vortex street behind oscillating airfoil can be already studied. Sufficient attention is also paid to simulating viscous core with focus on computational effectivness which can severely impair the overall usability of a computational tool. 3D vortex filament dynamics is studied using segmented vortex rings, which can be compared to analytic expression of vortex rings found in literature. Effects of number of segments and viscous core size is studied in detail, as it helps with understanding the behaviour of segmented helicoidal wake behind propeller. After the vortex filament has been analyzed, the method of constructing unsteady vortex wake using quadrilateral vortex panels is described at the end of this chapter.

## 5.1 2D free vortex velocity field

Free vortex is defined in Chapter 3 dedicated to potential flow theory. The main information necessary to study the free-vortex and its formations is the velocity in a point defined by a radius vector $[R_x, R_y]$ induced by a point vortex. Here, it is presented in a form suitable for numerical calculations:

$$\vec{c} = \frac{\Gamma[-R_y, R_x]}{2\pi R^2}. \tag{5.1}$$

The flow field of a single vortex and constant velocity contours are shown in Figs. 5.1 and 5.2. In case of a free vortex, the constant velocity contours are also streamlines.

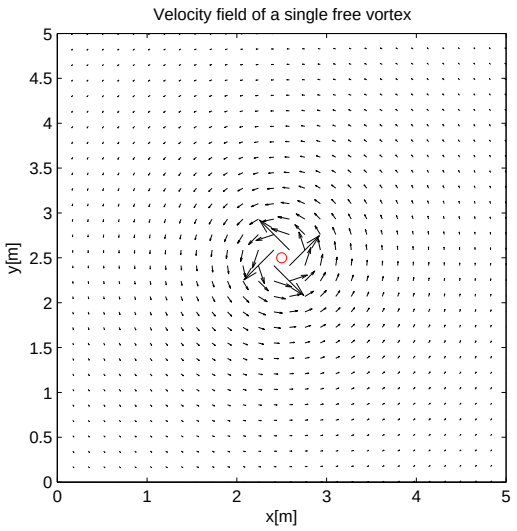


FIGURE 5.1: Velocity field around single free vortex.

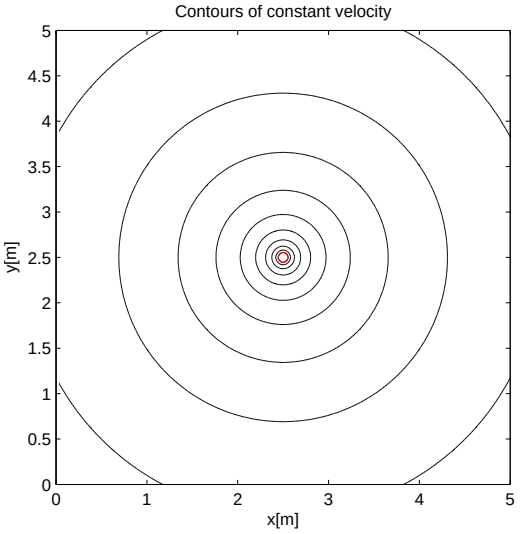


FIGURE 5.2: Constant velocity contour around single free vortex.

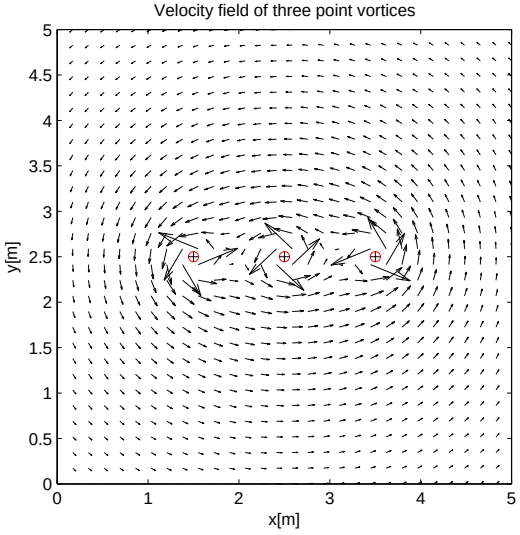


FIGURE 5.3: Velocity field around three vortices.

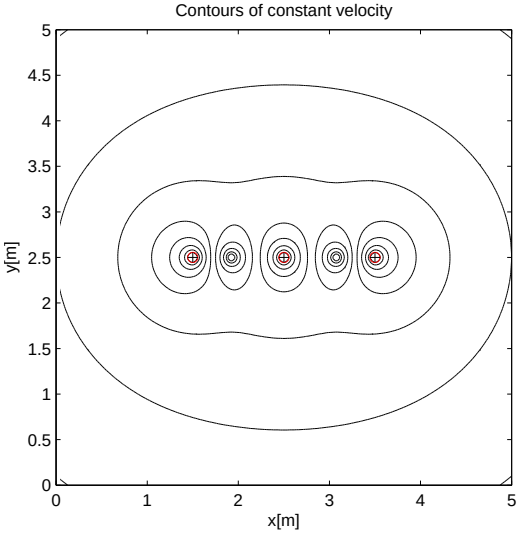


FIGURE 5.4: Constant velocity contour around three vortices.

When several vortices are present in the domain, the resulting flow is formed as a superposition of the flow fields around the respective vortices. As an example, three vortices, one unit length apart with the same circulation, are combined to form the resulting flow in Figs. 5.3 and 5.4. In the near field of the three singularities, the discrete character is very pronounced. Low velocity region can be observed between each pair of vortex centers, as a result of induced velocities canceling each other. In the far field, the three vortices already begin to induce flow field resembling that of a short vortex sheet panel, with constant vorticity distribution.

When more vortices are added equidistantly close to each other to form a straight segment, a vortex sheet is formed. The discrete character can be recognized only a very small distance from the sheet. The result of superposition of 30 vortices in close

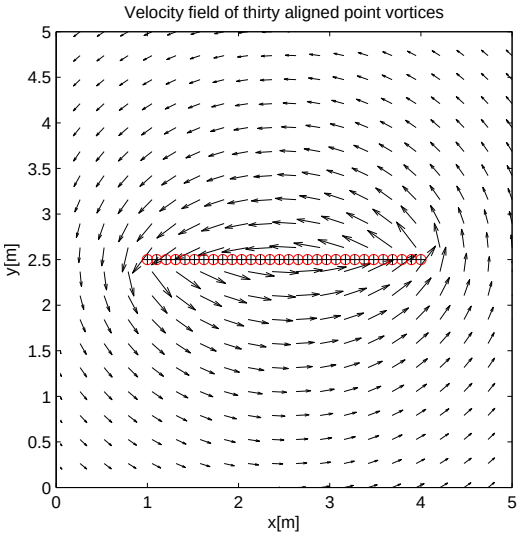


FIGURE 5.5: Velocity field around a large aligned group of vortices.

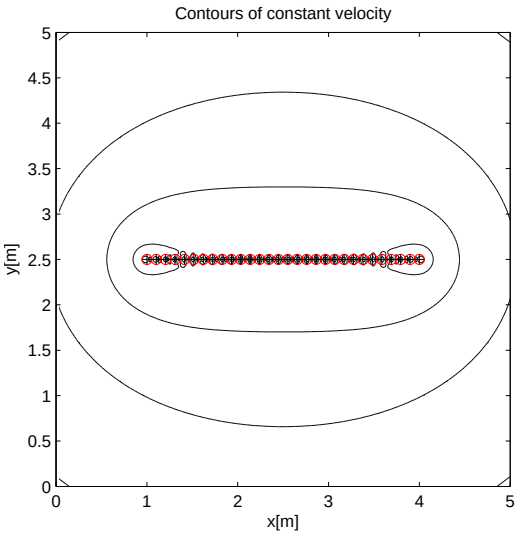


FIGURE 5.6: Constant velocity contour around a large aligned group of vortices.

proximity is plotted in Fig. 5.5 and 5.6. This approach would be computationally very inefficient, therefore, analytic expression for a constant strength vortex distribution panel can be derived [16] in panel coordinates $\bar{x}, \bar{y}$:

$$c_{\bar{x}} = \frac{\gamma}{2\pi}\left(tan^{-1}\frac{\bar{y}-\bar{y}_2}{\bar{x}-\bar{x}_2} - tan^{-1}\frac{\bar{y}-\bar{y}_1}{\bar{x}-\bar{x}_1}\right). \tag{5.2}$$

$$c_{\bar{y}} = -\frac{\gamma}{4\pi} ln \frac{(\bar{x}-\bar{x}_1)^2 + (\bar{y}-\bar{y}_1)^2}{(\bar{x}-\bar{x}_2)^2 + (\bar{y}-\bar{y}_2)^2}. \tag{5.3}$$

As can be seen in Fig. 5.7 and 5.8, the induced velocity field of a panel formed by constant vortex strength distribution and by 30 discrete vortices is nearly the same. The above definition of panel with constant vortex distribution is used in 2D panel methods.

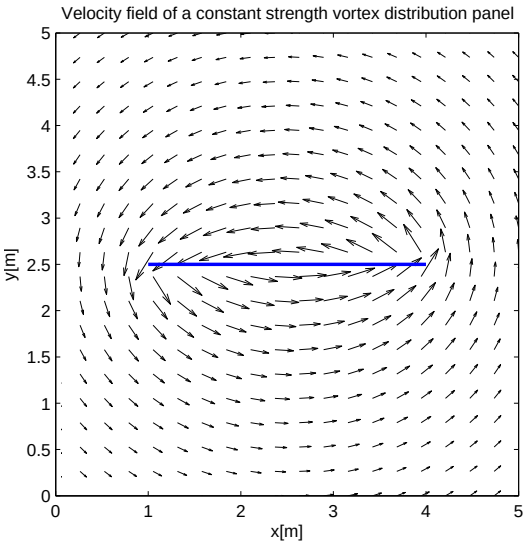


FIGURE 5.7: Velocity field around a constant vortex strength panel.

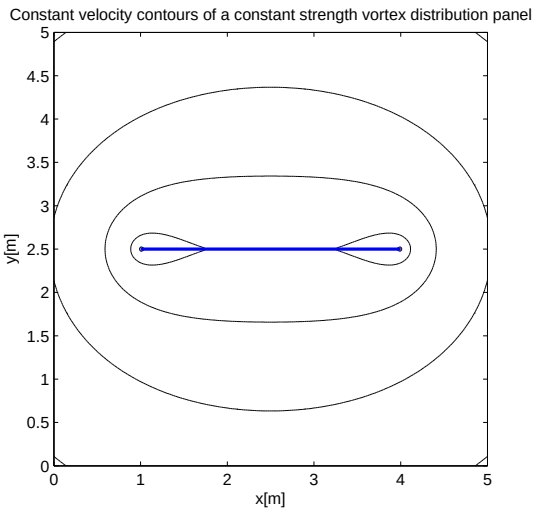


FIGURE 5.8: Constant velocity contour around a constant vortex strength panel.

## 5.2 Vortex dynamics in 2D

Whenever there is more than one vortex element in the domain, good chance is, that the induced velocity by other vortices at a vortex center is other than zero. In such case, the vortex starts to move in the direction of the induced velocity. The self-induced velocity of a vortex on its singular center is taken as zero. As an example of simple case of vortex dynamics, 3 vortices of the same strength are placed equidistantly on the same line. Without the need of any calculation, it is clear that the induced velocity at the middle vortex will be always zero and the velocities of the other two vortices will be perpendicular to the line connecting these two vortices. The middle vortex will remain in the same position while the other two will spin anticlockwise (in case of positive vortex strength) with the center of rotation being the middle vortex. The most simple numerical time stepping method is forward differencing, which uses the instant induced velocity at vortex centers multiplied by the time step to produce the position of the centers in the next time step.

$$\vec{r}_{n+1} = \vec{r}_n + \vec{c}_n \Delta t. \tag{5.4}$$

As seen in Fig. 5.9, the resulting path of the vortices depends on the chosen time step and deviates from the expected path considerably. Solution is to use the central differencing scheme (Eq. (5.5)), where the velocity vector used for translation is produced as the average velocity of current and next time step. Since the induced velocity at the next time step is not known a priori, forward differencing step is used to compute the

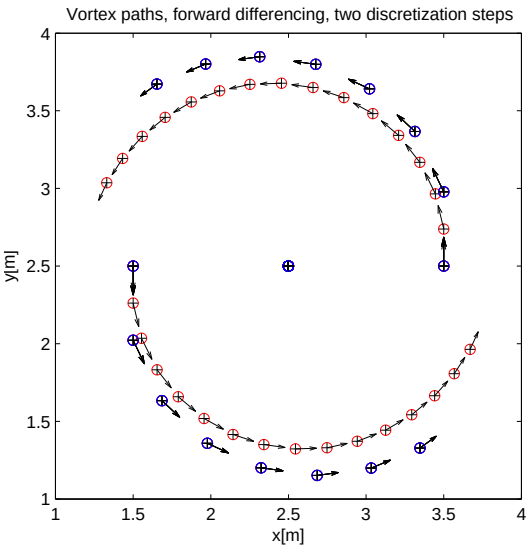


FIGURE 5.9: Vortex paths for two values of discretization step, forward differencing.

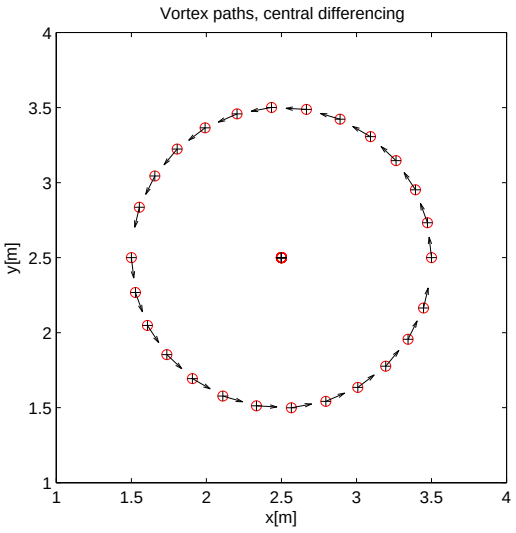


FIGURE 5.10: Vortex paths, central differencing.

$n+1$ velocity. The average of $n$ and $n+1$ velocities is then used for the displacement calculation. This approach has a disadvantage of requiring twice as many induced velocity computations compared to forward differencing method.

$$\vec{r}_{n+1} = \vec{r}_n + 0.5(\vec{c}_n + \vec{c}_{n+1})\Delta t. \tag{5.5}$$

The study of dynamic behavior of large groups of 2D vortices could be seen as distant from the topic of three-dimensional contra-rotating propeller wake problem, however some very important aspect of the 3D flow can be already tackled using 2D analysis.

### 5.2.1 Shape of a finite wing wake using 2D vortex dynamics

The distribution of circulation along the span of a low-aspect ratio finite wing can be (for the purpose of this test) simplified to an elliptic loading such as that in Figure 5.11. A continuous vortex wake sheet is shed from the trailing edge of the wing. In case of steady flow this wake can be discretized into separate vortex filaments of strengths $\Gamma_{shed} = \Delta\Gamma_{bound}$. The distribution of the shed circulation depends on the trailing vortices distribution. (see Fig. 5.11). In this example, the shed circulation distribution and trailing vortex positions on the finite wing are used to define the positions and circulation strenghts of 2D point vortices. The motion of the point vortices can be observed in a 2D plane (Fig. 5.12). If the resulting vortex paths are plotted in the $x, y, t$ coordinate system, the result is equivalent to a 3D vortex wake behind a wing with elliptic loading as in Fig. 5.13.

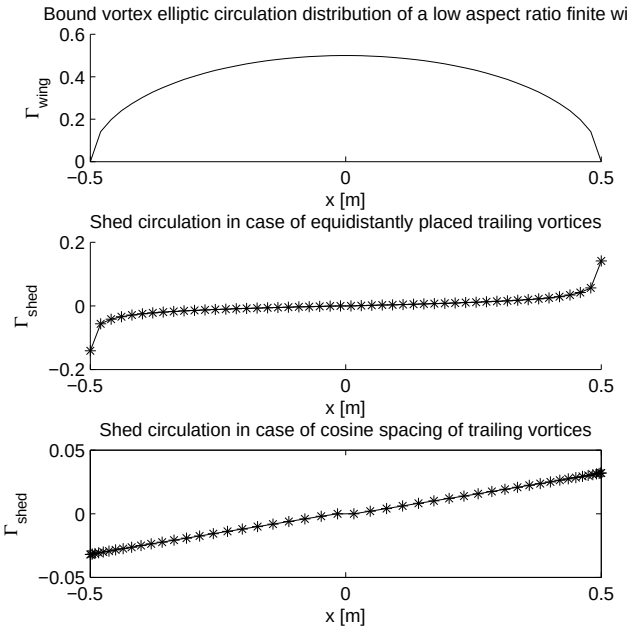


FIGURE 5.11: Example of bound circulation and shed circulation distributions.

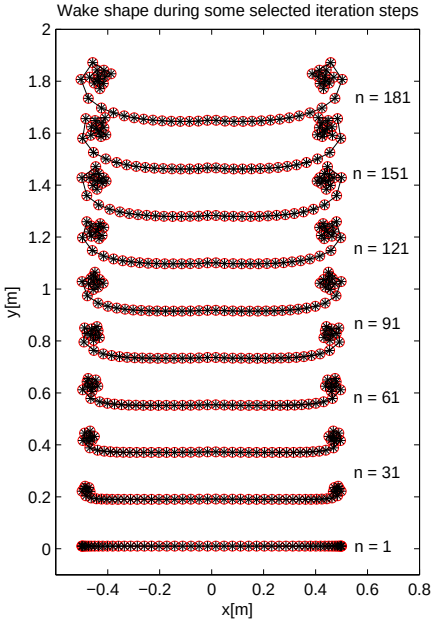


FIGURE 5.12: 2D vortex sheet shape at different iteration steps.

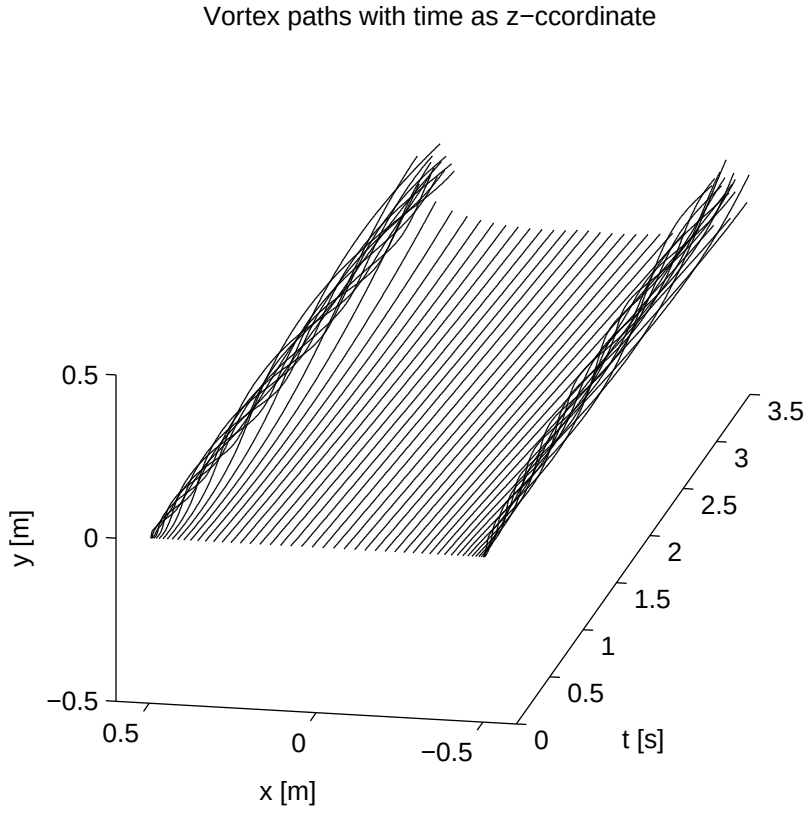


FIGURE 5.13: 2D point vortex positions as a function of time.

### 5.2.2 2D wake of an oscillating infinite wing

Last test of 2D vortex wake model is a case of an oscillating airfoil in a free stream. To verify the time stepping unsteady algorithm, experimental results [39] were found, which describe NACA 0012 airfoil oscillating with incidence angle being a sinus function of time. If the induced velocity by the vortex trail is neglected and the lift curve is assumed linear for given incidence angle amplitude, then also the bound circulation on the airfoil is a sinus function of time $\Gamma_{bound} = \Gamma_{max} sin(2\pi ft)$ Then, after each time step, a new 2D vortex with circulation strength $\Gamma_{shed} = \Gamma_{max}(sin(2\pi ft_n) - sin(2\pi ft_{n-1}))$ is created at the trailing edge. Based on the maximum angle of attack, 80 mm chord length, free stream velocity of 0.15 m/s and lift coefficient at maximum angle of attack, maximum circulation can be estimated as $\Gamma_{max} = 0.0012 m^2/s$.

The circulation shed in this unsteady case is perpendicular to the circulation shed due to spanwise bound vortex distribution simulated in the previous case. In general, time-change of the bound circulation results in shedding of vortex filaments parallel to the trailing edge, whereas spanwise change of the bound circulation (as in finite wings) results in shed vortex filaments parallel to the flow direction. The stability and shape of the wake depends on the frequency of oscillation, magnitude of circulation and velocity of the free stream (See results in Fig. 5.14). The thin vortex sheet is in fact a thin shear layer with a jump of velocity across the layer. The formation of the vortex structures can be also explained as a Kelvin-Helmholtz instability.

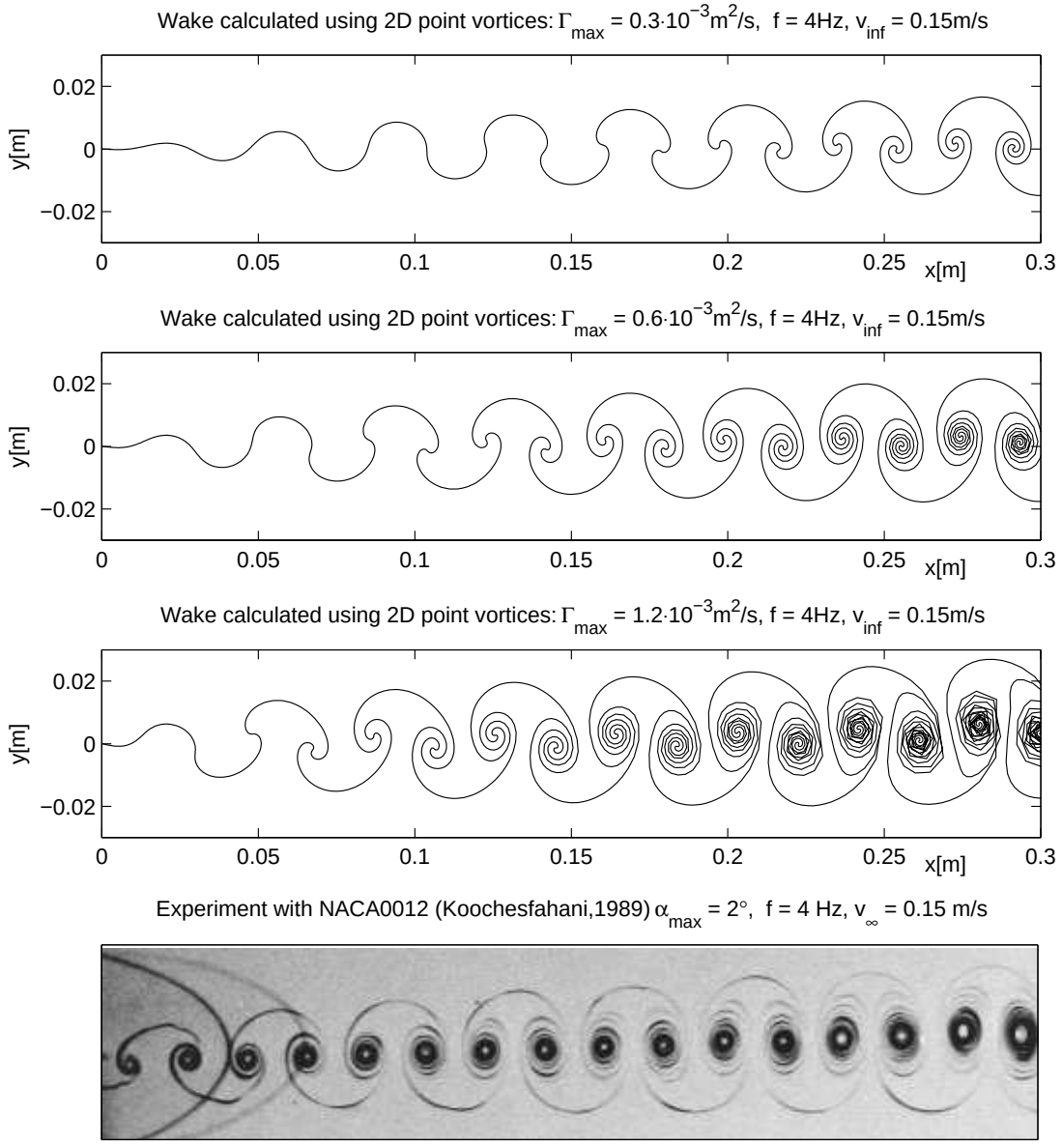


FIGURE 5.14: 2D wake of an oscillating airfoil, Source of photo:[39].

## 5.3 Vortex core models

In case of a free vortex, the local velocity of the flow $c = \Gamma/2\pi r$ approaches infinity as the vortex center $r \to 0$ is approached. Real vortices, on the other hand, can be artificially divided into two parts. Let $R_C$ be the vortex core radius. Then the outer part of the vortex tends to behave as a free vortex and the inner part forms a vortex core with almost linear velocity profile [17]. A very complete review of available vortex core models together with experimental verification is presented in [40]. Some of the vortex core models are very complex with different formulas for different regions and often

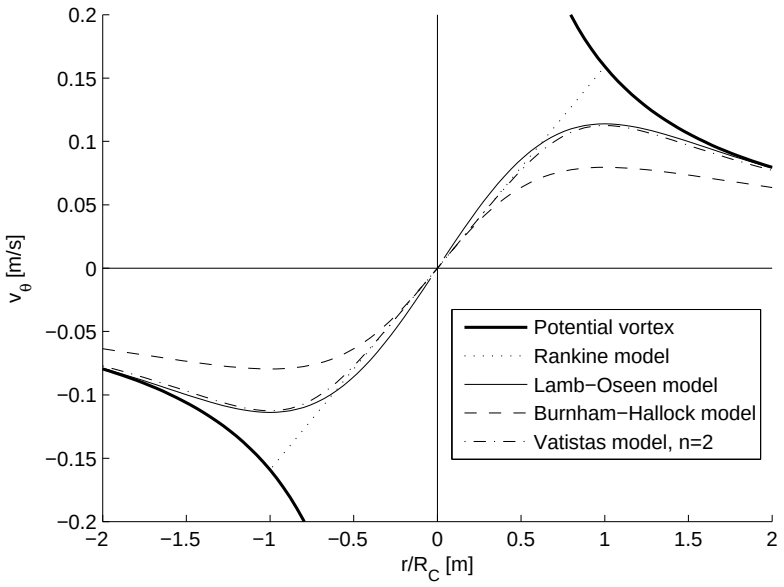


FIGURE 5.15: Comparison of 2D vortex core models.

including tunable parameters. The most important yet simple formulas are presented below and in Fig. 5.15.

**Rankine vortex core model**

$$c = \frac{\Gamma r}{2\pi R_C^2},\ \frac{r}{R_C} \leq 1, \tag{5.6}$$

$$c = \frac{\Gamma}{2\pi r},\ \frac{r}{R_C} > 1. \tag{5.7}$$

**Lamb-Oseen vortex core model** [41]

$$c = \frac{\Gamma}{2\pi r}\left[1 - exp\left(-1.2526\frac{r^2}{R_C^2}\right)\right]. \tag{5.8}$$

**Burnham-Hallock vortex core model** [42]

$$c = \frac{\Gamma}{2\pi}\frac{r}{R_C^2 + r^2}. \tag{5.9}$$

**Vatistas vortex core model** [43]

$$c = \frac{\Gamma}{2\pi R_C}\frac{r}{R_C\left[\left(\frac{r}{R_C}\right)^{2n} + 1\right]^{1/n}}. \tag{5.10}$$

According to a review [40], the most accurate fit to the experimental data is obtained using a complex model with two tuning parameters. A good fit was obtained with Vatistas model (for n=1.06) as well as with Burnham-Hallock (which is essentially Vatistas

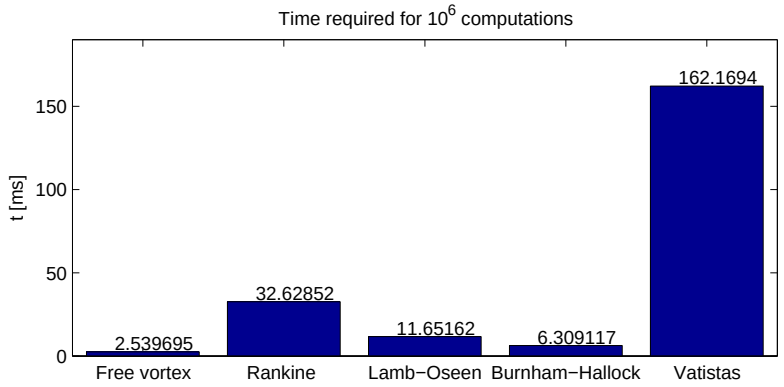


FIGURE 5.16: Comparison of the 2D vortex core models in terms of computational time.

model with n=1). Both the Rankine and Lamb-Oseen models gave slight over prediction of the velocity in the core.

For choosing a suitable vortex core model, an important aspect is also the computational time required for various models. To test this, $10^6$ subsequent induced velocity computations were performed with slightly varying random values of $r$ in MATLAB and the results are shown in Fig. 5.16.

As a conclusion, Rankine core model is both not very realistic and takes considerable computation time and therefore should be avoided. According to the the review [40], Vatistas model, when tuned, is quite accurate. However, it demands the most resources of all models. Burnham-Hallock and Lamb-Oseen models seem to provide fast and realistic vortex core simulation, the first of which is preferred by the review. These models will be also implemented into 3D vortex filament and used for simulating viscous effects and removing problems connected to singularity.

The initial size of the trailing vortex core is difficult to precisely determine and can be subject to fine-tunning according to experimental results. A simple formula is given by Saffman [44] for the vortex core growth. It simulates the effect of dissipation over time which is introduced by the core growth model.

$$R_C = \sqrt{4\nu t}. \tag{5.11}$$

In case of non-zero initial vortex core size $R_{Ci}$ the core growth is calculated as follows [44]:

$$R_C = \sqrt{R_{Ci}^2 + 4\nu t}. \tag{5.12}$$

## 5.4 Vortex filament in 3D space

Flow induced by a point vortex in 2D is equivalent to a flow induced in a plane by an infinite straight 3D vortex filament, which is normal to this plane. To be able to model different discretized geometrical shapes of the vortex filament, such as force-free wakes, it is necessary to obtain the formula for velocity at a point $P$ induced by a vortex segment leading from point 1 to point 2 [16]. The vector leading from point 1 to $P$ is defined as $\vec{r}_1$, the vector from point 2 to point $P$ is $\vec{r}_2$ and the vector from first to second point of the vortex segment is defined as $\vec{r}_0$ - see Fig.5.17.

$$\vec{c} = \frac{\Gamma}{4\pi} \frac{\vec{r}_1 \times \vec{r}_2}{|\vec{r}_1 \times \vec{r}_2|^2} \vec{r}_0 \cdot \left( \frac{\vec{r}_1}{|\vec{r}_1|} - \frac{\vec{r}_2}{|\vec{r}_2|} \right). \tag{5.13}$$

The Lamb-Oseen vortex model has been extended to a 3D filament case in [A 2] by the author. The velocity field induced around the midpoint of the filament by the Formula (5.14) in case of large $\vec{r}_0/R_C$ ratio is equivalent to the 2D vortex core Lamb-Oseen model.

$$\vec{c} = \frac{\Gamma}{4\pi} \frac{\vec{r}_1 \times \vec{r}_2}{|\vec{r}_1 \times \vec{r}_2|^2} \vec{r}_0 \cdot \left( \frac{\vec{r}_1}{|\vec{r}_1|} - \frac{\vec{r}_2}{|\vec{r}_2|} \right) \left[ 1 - exp\left( -1.2526 \frac{|\vec{r}_1 \times \vec{r}_2|^2}{R_C^2 |\vec{r}_0|^2} \right) \right]. \tag{5.14}$$

The same procedure is applied on Burnham-Hallock vortex, i.e. the formula for a 3D free vortex filament is multiplied by an expression derived from the 2D Burnham-Hallock model and the result is below (Formula (5.15)):

$$\vec{c} = \frac{\Gamma}{4\pi} \frac{\vec{r}_1 \times \vec{r}_2}{|\vec{r}_1 \times \vec{r}_2|^2} \vec{r}_0 \cdot \left( \frac{\vec{r}_1}{|\vec{r}_1|} - \frac{\vec{r}_2}{|\vec{r}_2|} \right) \left( 1 + \frac{R_C^2 |\vec{r}_0|^2}{|\vec{r}_1 \times \vec{r}_2|^2} \right)^{-1}. \tag{5.15}$$

In conclusion, both Burnham-Hallock and Lamb-Oseen models were successfully applied on a finite 3D vortex segment. Induced velocity profiles at different z-coordinates are shown for various core models in Fig. 5.18. The total computational time (in miliseconds) of $10^6$ subsequent calculations is ploted in Fig. 5.19. As can be seen, the calculation of the influence of a finite 3D vortex filament on a point in space is about one order of magnitude slower than calculation of the influence velocity of a 2D point vortex. However, the proposed 3D core model implementation does not impact the calculation time as significantly as in case of the 2D vortex. The final selection of the 3D vortex core model will be made according to the simulation results, although presumably the impact of this choice will be very small.

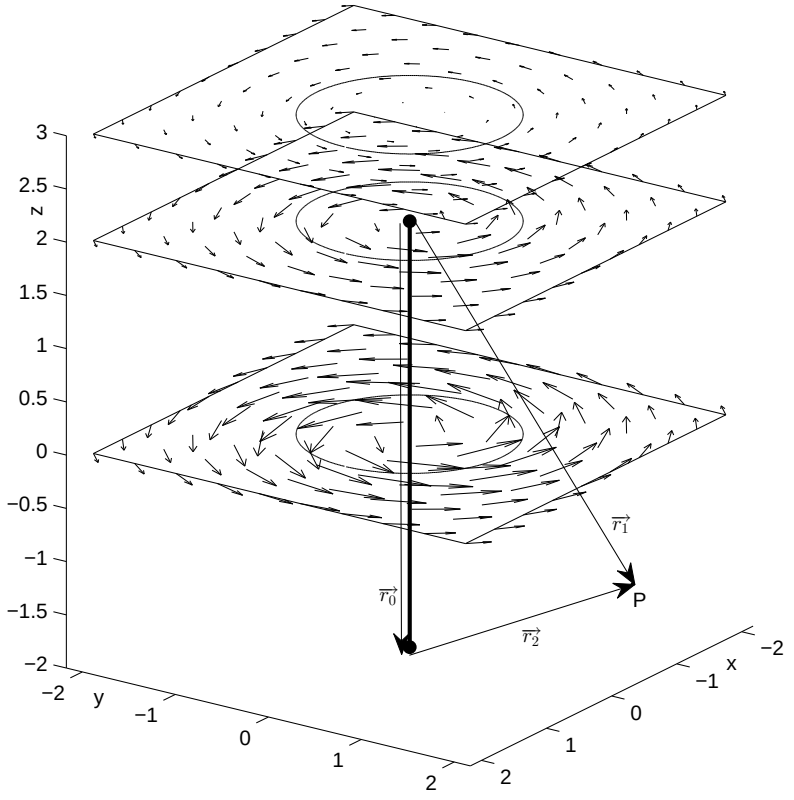


FIGURE 5.17: Flow field around a vortex segment, with Lamb-Oseen core implemented.

### 5.4.1 Vortex rings

One of the simplest shapes which a vortex filament can form is the vortex ring. Desingularized expression for the velocity induced by a circular vortex ring filament was derived analytically and can be found in [45].

$$c_r = \frac{\Gamma}{2\pi k_1}\frac{a}{r}\left[\frac{r^2+R^2+a^2+R_C^2}{k_2}E(k_3) - K(k_3)\right], \tag{5.16}$$

$$c_a = \frac{\Gamma}{2\pi k_1}\left[\frac{-(r^2-R^2+a^2+R_C^2)}{k_2}E(k_3) + K(k_3)\right], \tag{5.17}$$

where $K(k_3)$ and $E(k_3)$ are complete elliptic integrals of first and second kind and where:

$$k_1 = \sqrt{(r+R)^2+a^2+R_C^2},\ k_2 = (r-R)^2+a^2+R_C^2,\ k_3 = \frac{4rR}{k_1^2}. \tag{5.18}$$

This new vortex structure will be called a circular vortex ring. Apart from helping validate the behavior of a vortex filament ring made of segments, it can be also used to simulate e.g. ducts or hubs in the contra-rotating propeller problems.

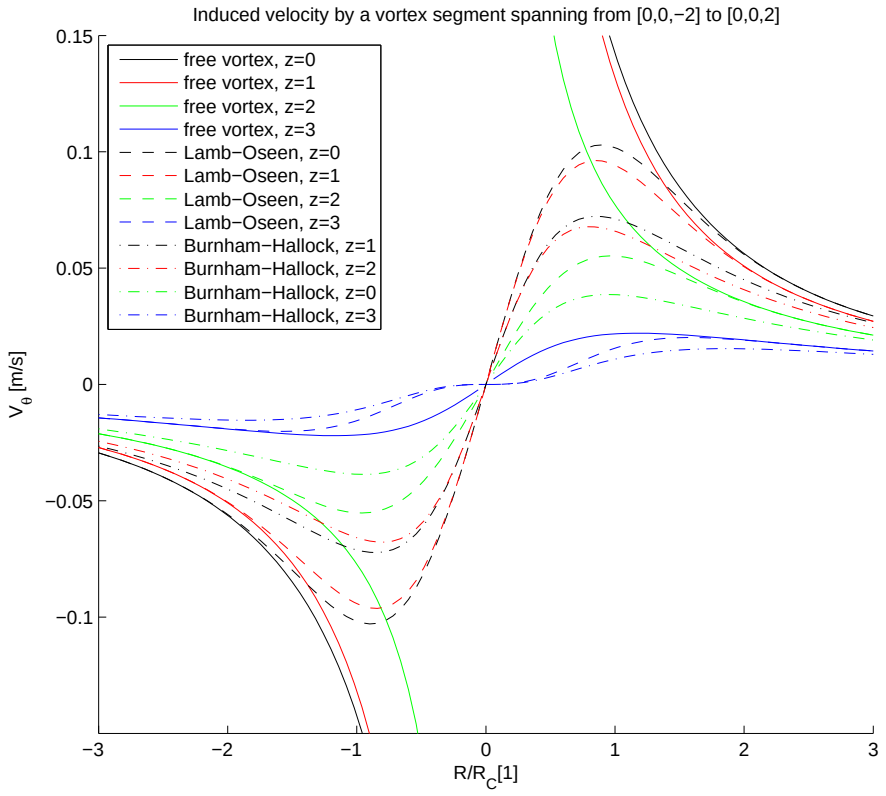


FIGURE 5.18: Comparison of the 3D vortex core models at various z-coordinates. Note, that z=3 plane does not intersect the vortex segment.

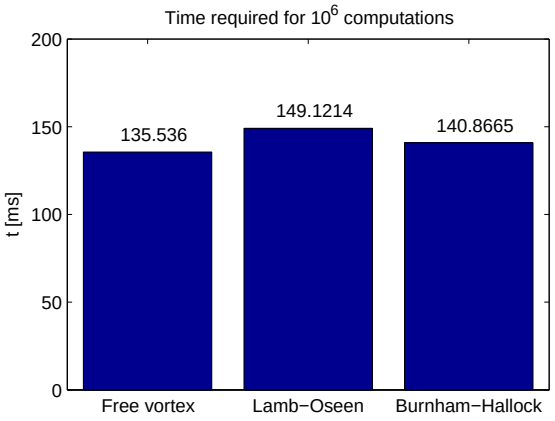


FIGURE 5.19: Comparison of the 3D vortex core models in terms of computational time.

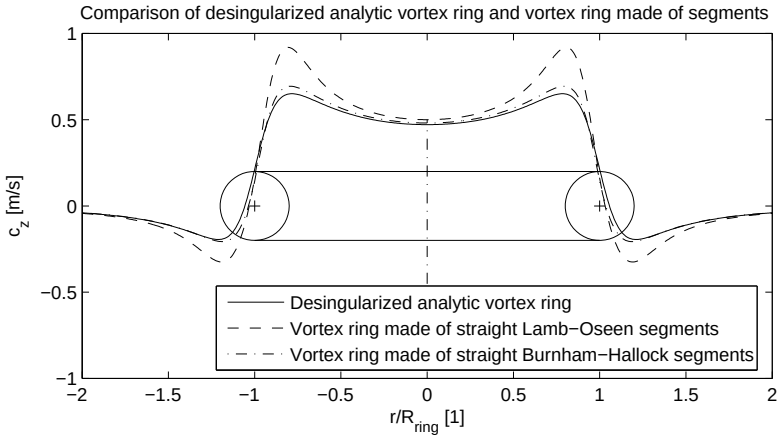


FIGURE 5.20: Comparison of analytic vortex ring and a vortex ring made of segments.

As can be seen in Fig. 5.20, using the analytic formula for desingularized vortex ring ( Formula (5.17)), the resulting axial velocity distribution differs slightly from the segmented vortex ring made of 100 straight segments of Lamb-Oseen vortex especially near and inside the core. This difference can be contributed to different vortex core model of the analytical vortex ring, which resembles Burnham-Hallock core model.

After modifying various parameters of the segmented vortex ring, such as number of segments, core size and core type, it becomes clear, that these changes do not affect the far field influence of the ring. However the near-field is affected by these parameters significantly. As a representative component of the velocity field, axial velocity along a line passing through the ring center and perpendicular to the ring itself has been evaluated. Influence of core size on axial velocity distribution is in Fig. 5.21.

The number of segments also influences the axial velocity distribution as seen in Fig. 5.22, but the distribution quickly converges for sensible number of panels. If the point of interest lies very close to the vortex ring filament, or lies directly on the filament (i.e. self-induced velocity), the solution is very sensitive to the core size and number of segments. The self-induced velocity of the ring has been investigated and the results is in Fig. 5.23. For every core size, there is a number of segments such that when increased, the self-induced velocity does not change. The smaller the core size, the higher is the required number of segments.

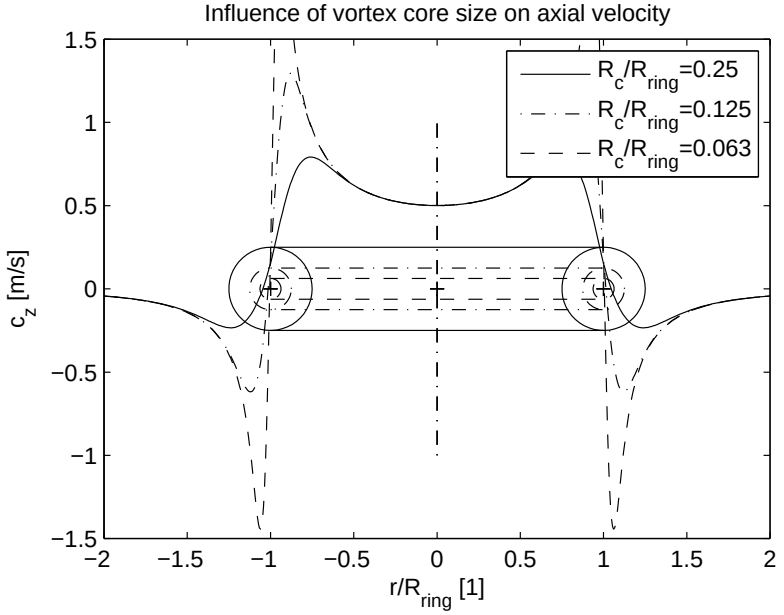


FIGURE 5.21: Influence of core size on axial velocity.

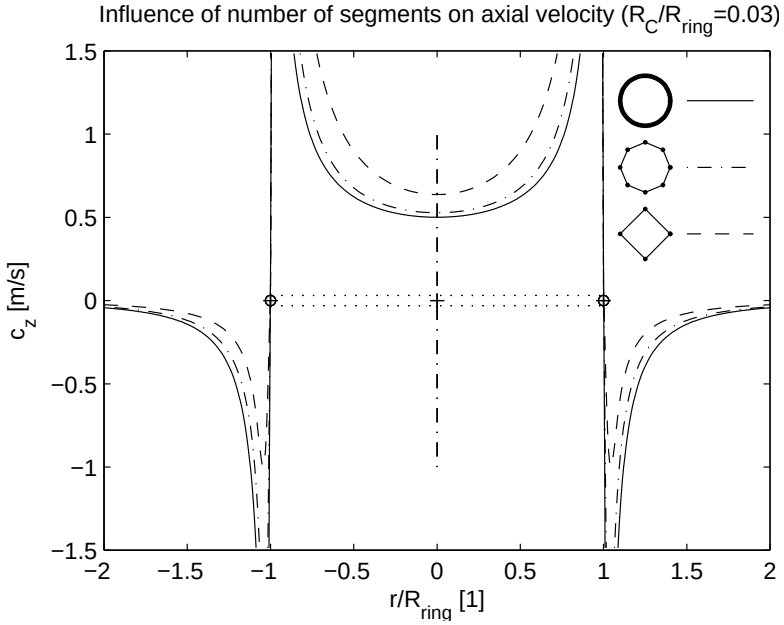


FIGURE 5.22: Influence of number of segments on axial velocity.

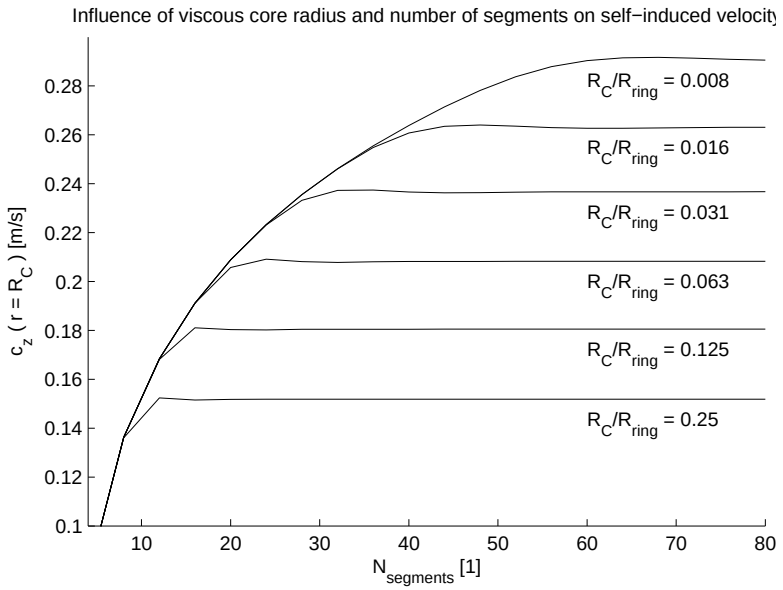


FIGURE 5.23: Influence of number of segments and core size on self induced velocity.

## 5.5 3D vortex dynamics

All vortex filaments in fluid should form a closed loop or extend to the fluid boundary, according to Helmholtz's second theorem. These vortex filament structures induce velocities on each other and also on itself. A detailed analysis of the self-induced velocity of a straight and a curved vortex filament segment by Batchelor [46] shows that a curved vortex filament moves with infinite speed under the action of the self-induced velocity field. Batchelor [46] concludes, that the mathematical notion of the line vortex is "Of limited direct value in problems involving development with time " and another limitation of its use is the instability described by Kelvin and Helmholtz. The wide spread of methods, both steady and unsteady, that use some form of vortex filament segments shows, that when suitable workarounds are implemented, the vortex filament based models can be quite valuable.

### 5.5.1 Vortex filament growth and stretching

The vortex filament in three-dimensional space is subject to the same core growth, as in the 2D case (Eq. (5.12)). As a reaction to the free stream velocity field and induced velocity by other vortices, the vortex filaments can translate, rotate and change shape. Additionally, the vortex segments are also stretched or compressed, vortex stretching being statistically much more probable process of the two. The influence of the vortex stretching on the rotor dynamics results is discussed in [47], together with the explanation of the process of stretching, which can be simulated by decrease in the viscous

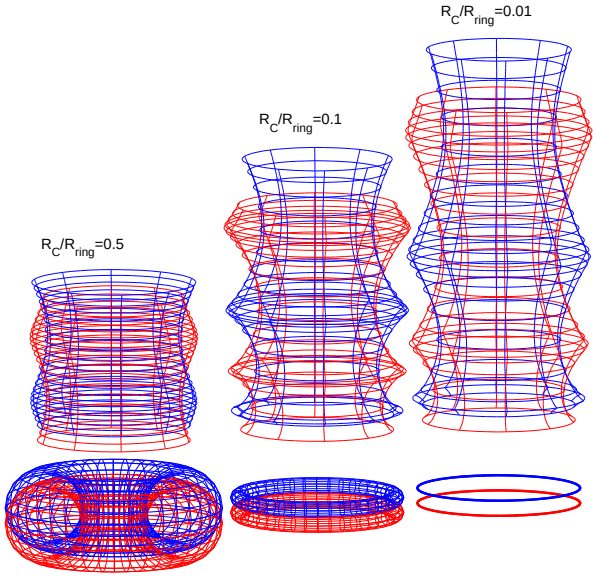


FIGURE 5.24: Paths of a pair of leapfrogging vortex rings, depending on core size.

core size while maintaining constant circulation. The change of core radius $\Delta R_C$ due to strain $\epsilon = (l + \Delta l)/l$ is given in Eq. (5.19) [47].

$$\Delta R_C = R_C \left(1 - \frac{1}{\sqrt{1+\epsilon}}\right). \tag{5.19}$$

### 5.5.2 Vortex rings interaction

When a vortex ring is formed, it is being propelled by a self-induced velocity. Some preliminary research of this motion using vortex rings made of segments presented in the previous section showed, that this motion does not depend only on vortex strength and radius of the ring, but also on the number of elements (discretization) and the vortex core size. With the vortex core size approaching 0, the self-induced velocity approaches infinity.

To test the behavior of the vortex ring, first the phenomenon called leapfrogging is observed. Two identical vortex rings that share common axis of symmetry are placed some distance from each other. They start to move in the same direction under their self-induced velocity, but at the same time their radiuses and velocities oscillate due to the mutual influence of the rings. The paths for different core sizes are plotted in Fig. 5.24. As can be seen, the main difference is the overall velocity of the rings, which increases with the decrease of core radius. This is in agreement with previous findings.

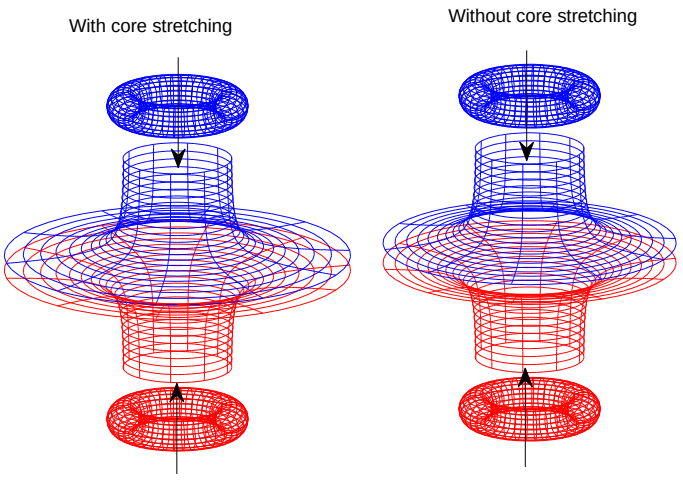


FIGURE 5.25: Paths of a vortex ring and its mirrored counterpart.

Next, a pair of identical vortex rings with opposite circulation sharing the axis of symmetry is observed. This time, the vortex rings will approach each other and rapidly increase their radius. This is a good case to illustrate the influence of vortex stretching. As the ring radius grows, the overall length of the filament also grows and therefore the core size is reduced. The comparison is in Fig. 5.25.

As can be seen, the vortex rings with incorporated vortex stretching model will increase their radius faster, due to the reduction of vortex core size.

## 5.6 Unsteady 3D vortex wake model

### 5.6.1 Vortex wake description

As a result of spanwise change of bound circulation over wing, vortex sheet is shed from the trailing edge of the wing. This continuous sheet of vorticity simulates the wake of a wing. Defining a continuous vorticity distribution wake would be complicated, if not impossible, so a discretized version of the wake model is used in numerical calculations.

The wing can be approximated by a lifting line, lifting surface or a 3D panel surface (see Fig. 5.26). Regardless of the wing representation type, the wing model provides a bound circulation distribution, which needs to be shed into the wake.

Vortex lattice wake model (see Fig. 5.27) is based on the same rectangular vortex ring segments (equivalent to constant doublet distribution) as those used for 3D panel

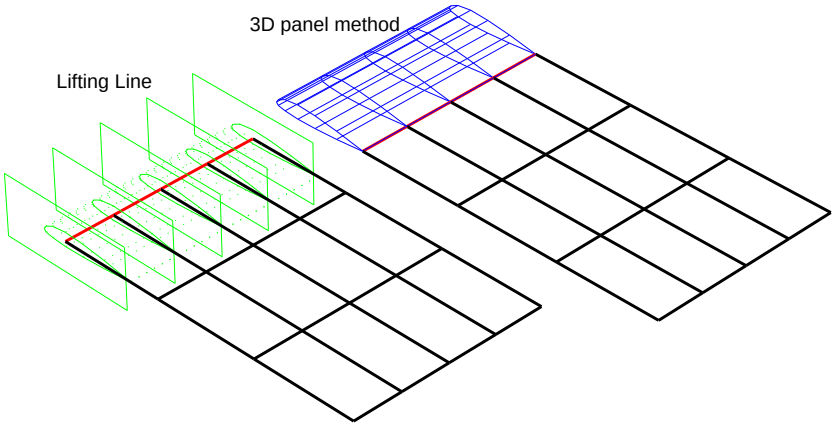


FIGURE 5.26: The same wake model attached to a lifting line(left) and to the trailing edge of a wing made of 3D panels (right).

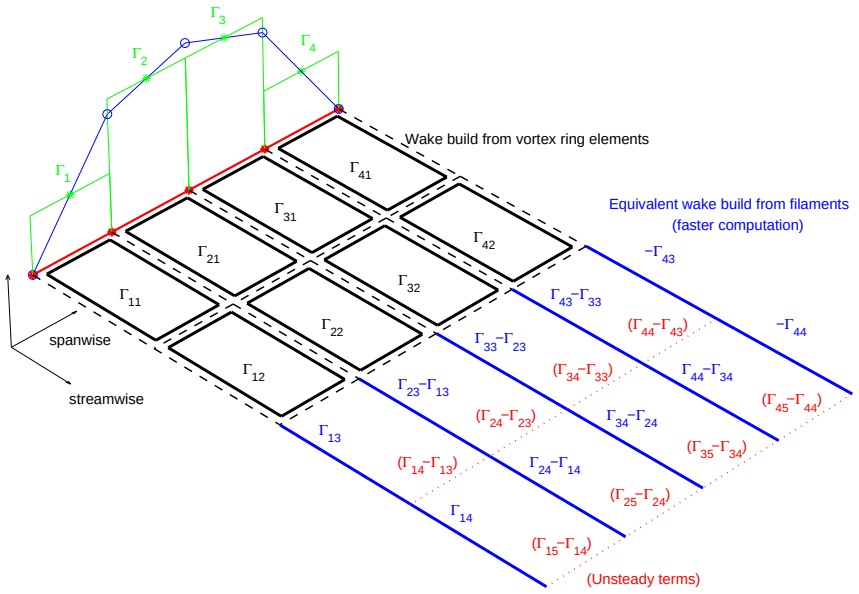


FIGURE 5.27: Vortex wake structure and nomenclature. Both vortex filament and vortex ring approaches are shown.

method surface discretization. At each time step the existing wake panels are convected downstream using the local velocity value. A new vortex panel per spanwise station $i$ is shed, with circulation $\Gamma_{i1}$. The original vortex panels being convected downstream increase their row number by one $\Gamma_{i,j} = \Gamma_{i,j+1}$.

Excluding the vortex panels on the edge of the wake surface, each vortex ring panel shares its edges with 4 neighboring panels. In other words, during calculation of a wake formed by vortex ring panels, each filament edge of a vortex panel is calculated twice, but each time with different circulation strength. To reduce computational time

twice, the influence from two coinciding edges is calculated once and the superposition of the two circulation strenghts is used. Further simplification is possible for steady cases. When the calculation is steady, the superposition of circulation strengths of two neighboring panels in streamwise direction results in zero influence and these filaments can be omitted. The resulting wake is not formed by vortex ring panels any more, but rather by separate vortex filaments, although the induced velocity field is equivalent.

This concept of an unsteady wake was tested by the author et al. in an investigation of vertical axis wind turbines both numericaly and experimentaly [A 3]. The main importance of this work lies in describing the issues of wake-to-wake and wake-to-blade close interactions with an attempt to solve them using local manipulation with induced velocity and velocity cut-off. Velocity cut-off at a presribed distance is in fact the simplest model of a vortex core, superseded by the Lamb-Oseen model used in this thesis. Without any vortex core model, the wake will lose stability under induced infinite velocities and wake shapes such as that in Fig. 5.28 are not possible.

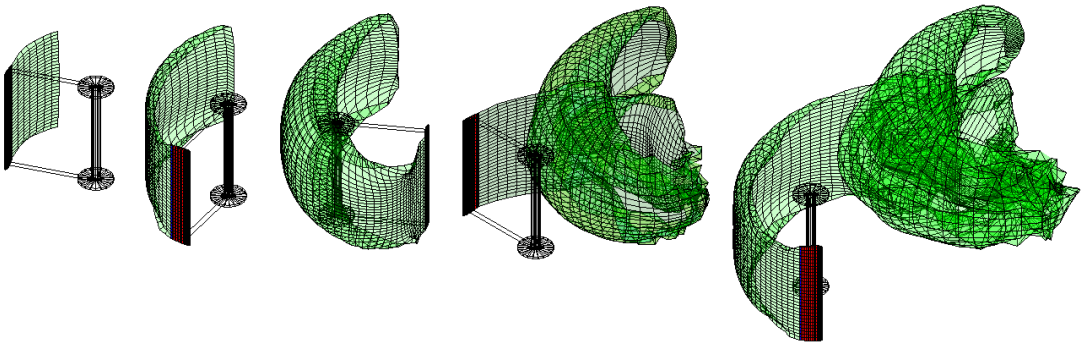

FIGURE 5.28: Single-bladed VAWT turbine force-free wake evolution. Also appeared in [A 3]

# Chapter 6

# Propeller Blade Representation

Two models for representing the propeller blades were developed and tested. Lifting line model is relatively simple, yet powerful tool that evolved from Prandtl lifting line theory. The advantage of this model is the fact that it can use very robust experimental or computed polar data for establishing the local lift and viscous drag coefficients under the conditions of induced velocity by the wake. Drawbacks include reduced accuracy for cases where strong three-dimensional flow is present, such as in case of low aspect-ratio blades and blades with large sweep angle.

The second model is using 3D panel method to represent each blade and a sophisticated and rather complex procedure of coupling a 2D boundary layer model. Each of the models will be further described after they are introduced. As a validation, the behavior of both models is tested using case of a finite wing, for which it is relatively simple to obtain reference using commercial CFD codes.

## 6.1 Lifting line model

The lifting line model presented in this thesis is validated using Glauert solution to Prandtl's equations.

### 6.1.1 Glauert solution to Prandtl's equations

In case of a symmetric wing, half of the wing of wingspan $l$ is divided into $m = 1...M$ span positions described by coordinate $x$. Cosine span position distribution or any other distribution with higher density at the tip is desirable. Wing tip position $x = l/2$ should not be included in the distribution. Transformation $\beta = acos(-2x/l)$ is used to describe

the span position by a position angle $\beta$. The following system of M equations is solved for $N = M$ unknown coefficients $k_n$ [17].

For m = 1...M

$$\sum_{n=1}^{N} sin((2n-1)*\beta(m))\,(sin(\beta(m)) + (2n-1)*\zeta(m)k_n) = \zeta(m)\alpha_\infty(m)sin(\beta(m)), \tag{6.1}$$

where $b(m)$ is chord length at span position $m$ and where:

$$\zeta(m) = \frac{b(m)}{4l}\frac{dc_l}{d\alpha_\infty}. \tag{6.2}$$

After solving the system of equations for $k_n$, the circulation distribution is found as follows:

$$\Gamma(m) = 2lc_\infty \sum_{n=1}^{N} k_n sin[(2n-1)\beta]. \tag{6.3}$$

The total lift, induced drag of the wing and their respective coefficients are calculated as follows [17].

$$F_L = \rho c_\infty \int_{-l/2}^{l/2} \Gamma(x)d(x), \tag{6.4}$$

$$c_L = \frac{2}{c_\infty A_{wing}} \int_{-l/2}^{l/2} \Gamma(x)d(x), \tag{6.5}$$

$$F_D = \rho c_\infty \int_{-l/2}^{l/2} \Gamma(x)\alpha_i(x)d(x), \tag{6.6}$$

$$c_D = \frac{2}{c_\infty A_{wing}} \int_{-l/2}^{l/2} \Gamma(x)\alpha_i(x)d(x). \tag{6.7}$$

To demonstrate the use of the Glauert's solution, a rectangular wing of unit wingspan, aspect ratio $AR = 5$ and an angle of attack $\alpha = 5°$ is analyzed. For comparison, the parameters of an elliptic wing of the same area and wingspan are also computed. For a fair comparison, the angle of attack of the elliptic wing is varied until the lift coefficients (and in this case also absolute lifts) are equal. This occurs for $\alpha_{el} = 4.83°$. The results are in Fig. 6.1. The induced drag coefficients are 0.0034 and 0.0031 for rectangular and elliptic wings respectively with the same $c_L = 0.22$ value. In this case the rectangular wing has about 9% higher induced drag compared to the elliptic wing. An elliptic wing

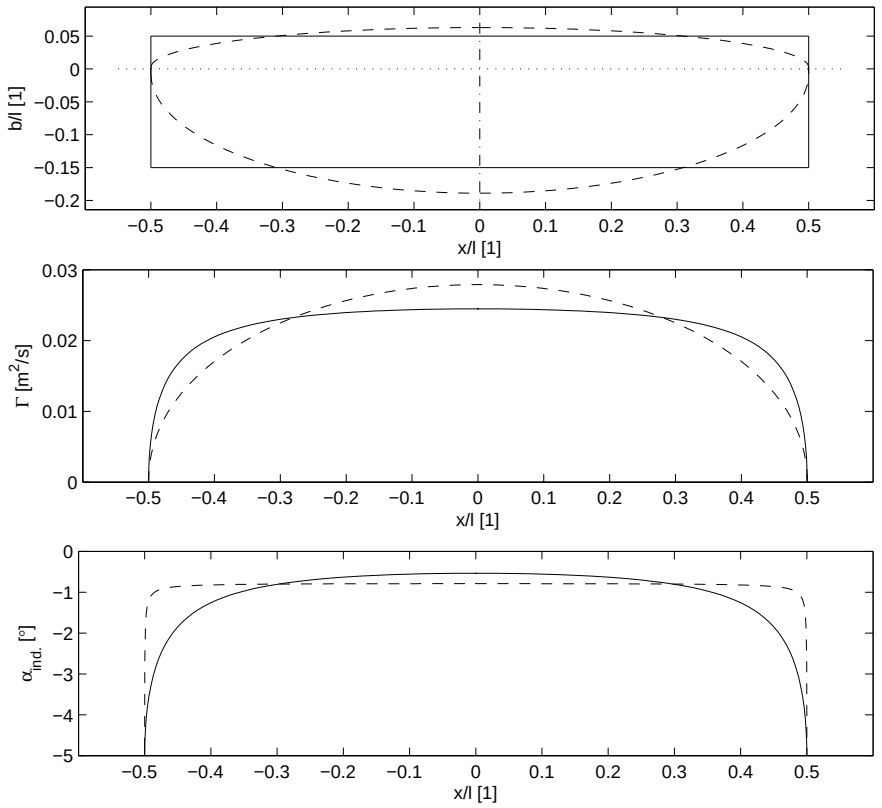


FIGURE 6.1: Circulation and induced angle distributions for a rectangular and an elliptic wing calculated using Glauert's solution.

is used for establishing span efficiency factor of the planforms due to the fact that it produces the least induced drag possible.

### 6.1.2 Discretized lifting line model description

The lifting line model can be used as a method of solving a simplified finite wing representation described by Prandtl's lifting line theory. For a symmetric wing with frozen (predefined) flat wake and small angles of attack the solution of Glauert (Eq. (6.1)) can be used, which is however not suitable for the case of propeller blades.

A general lifting line model allowing arbitrary wake shape, non-linear lifting curve of the airfoils and to some degree also non-zero sweep angle is required for the simulation of propeller blades. The topology of the wake has been already defined, the lifting line model and its link to the wake will be described here.

The solution procedure (see Fig. 6.2) is iterative and begins with lifting line with no wake and thus no induced velocities. The induced velocities are calculated at specific points on the lifting line called span positions. These points are distributed using linear or cosine distribution or combination of both. During first iteration step, the effective

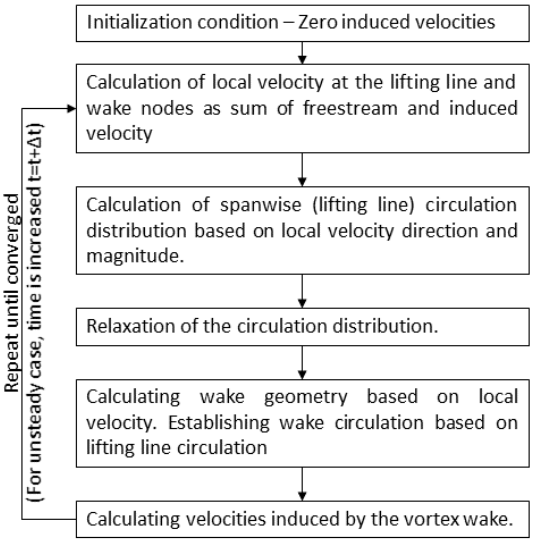


FIGURE 6.2: Block diagram of the iterative solution procedure.

angle of attack at each span position is equal to the angle of attack of the whole wing, which creates a lifting line circulation distribution with no decay towards the tips. Such distribution produces strong wing tip vortices, which eventually (during iteration) spread more evenly until the distribution converges to the final solution. Under-relaxation is usually required to keep the solution stable. Under-relaxation is carried out by computing circulation distribution as weighted average of new solution and solution of previous iteration step. The amount of under-relaxation (weight of the previous solution) needed for stable solution depends on many factors such as the wing aspect ratio.

For reliable results and stable solution it is important to make sure that a smooth lifting line circulation distribution produces smooth induced velocity distribution. The way in which the lifting line is linked to the vortex wake is visible in Fig. 6.3. The simplest approach consists of averaging the circulation distribution over a lifting line segment, which produces a piecewise constant distribution of circulation that can be directly used in the wake model.

As can be seen in Fig. C.1 (Appendix C), this approach leads to good agreement of the induced velocity with Glauert solution for the midspan area, the span positions near tip however show unrealistic velocities - the induced velocity distribution produced by the simplest model is not smooth. Note, that a viscous core model is used (otherwise the induced velocity would approach infinity near span positions). Also note, that the induced velocity oscillates due to presence of the discrete vortices, however the line connecting induced velocities at span position coordinates is observed and denoted "induced velocity distribution".

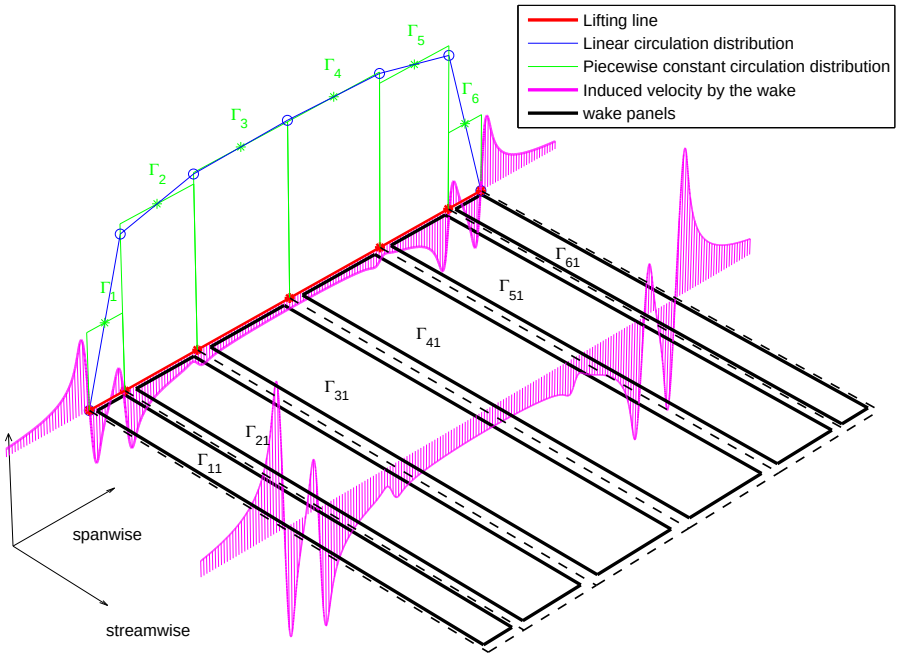


FIGURE 6.3: The simplest model of the lifting line directly connected to the wake model.

When the number of segments is increased (Fig. C.2, Appendix C), the span length that is in agreement with Glauert solution increases until only small tip section is influenced. However even this small departure from smooth distribution at the tip can spread during iteration and compromise the stability and precision of the solution.

### 6.1.3 Tip treatment of the lifting line model

Two different treatments are proposed to overcome the difficulty described in previous paragraphs.

*Option 1.* - The i-th bound circulation segment between i-th and (i+1) span position is not calculated as the mean but as the maximum of the two neigboring span position circulation strengths $\Gamma_i = max(\Gamma_{i+1}, \Gamma_i)$. The resulting induced velocity is smooth and close to the Glauert solution except the last point at the very tip. (Figures C.3 and C.4, Appendix C) This last point doesn't affect the solution, because its influence is replaced by the boundary conditions. The boundary conditions are zero effective angle of attack and zero circulation at the tip.

*Option 2.* - The second treatment of the tip circulation behavior is based on moving the last shed vortex from the lifting line tip to the last segment center. The piecewise

constant circulation distribution is based on the interpolated value at the center of each lifting line segment. The interpolation method is a shape-preserving piecewise cubic interpolation (Fig. C.5, Appendix C). The tip span point is now positioned outboard of the last shed vortex and the negative of induced velocity at this point is used. The resulting induced velocity field shows the best agreement with Glauert solution (Fig.C.6, Appendix C), at the expense of having to modify the wake geometry by shifting the outermost vortex filaments.

### 6.1.4 Alternative drag and lift evaluation of the lifting line model

Lift and induced drag can be evaluated based on the circulation (Eq. (6.5), (6.6), (6.7), (6.7)) as was demonstrated in Section 6.1.1. When viscous drag is considered in the calculation, the following approach is used instead. The lifting line model in this work uses airfoil polars for determining angle of attack vs. lift coefficient and drag coefficient relations. The polar data can be either based on experiment or calculated numerically using 2D panel method with boundary layer model (i.e. XFOIL software or similar). The lift and drag coefficients of a section of a finite wing $c_L, c_D$ is calculated based on the 2D lift and drag coefficients $c_l, c_d$ and local induced angle of attack $\alpha_i$:

$$c_L = cos(\alpha_i)c_l - sin(\alpha_i)c_d, \tag{6.8}$$

$$c_D = c_{Di} + c_{Dvisc} = sin(\alpha_i)c_l + cos(\alpha_i)c_d. \tag{6.9}$$

### 6.1.5 Rectangular wing set to a sudden motion

In order to test the behavior of the vortex wake, several cases have been computed. In the first case, an untwisted rectangular wing with small angle of attack is set to a forward motion. A starting vortex forms at the moment of impulsive start (Fig. 6.4), and as the distance between starting vortex and the wing increases, the flow conditions around the wing converge to a steady state solution (Fig. 6.5). The small angle of attack was chosen because the lift curve can be approximated by a straight line $dc_l/d\alpha_\infty = 2\pi$ for angles of attack $\alpha_\infty$ smaller than approximately 10°. As a reference, Glauert solution to Prandtl's lifting line theory is used.

### 6.1.6 Oscillating rectangular wing

Experimental results of a rectangular finite wing with semispan of 60 inches (wingspan $l = 3.048m$), chord $b = 0.3048m$ and NACA 0015 airfoil section were found in [48]. The wing was performing a sinusoidal pitching motion, with axis of rotation at quarterchord.

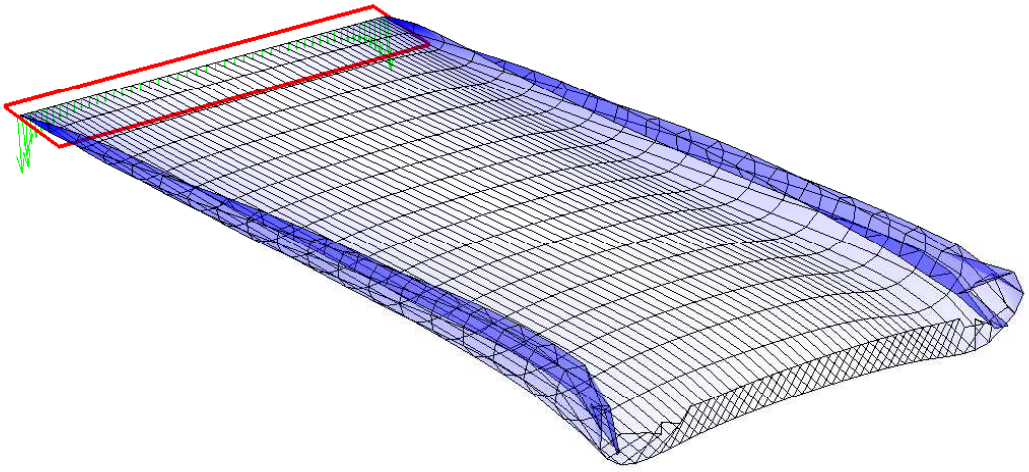

FIGURE 6.4: Impulse start of the rectangular wing. Note the starting vortex roll-up.

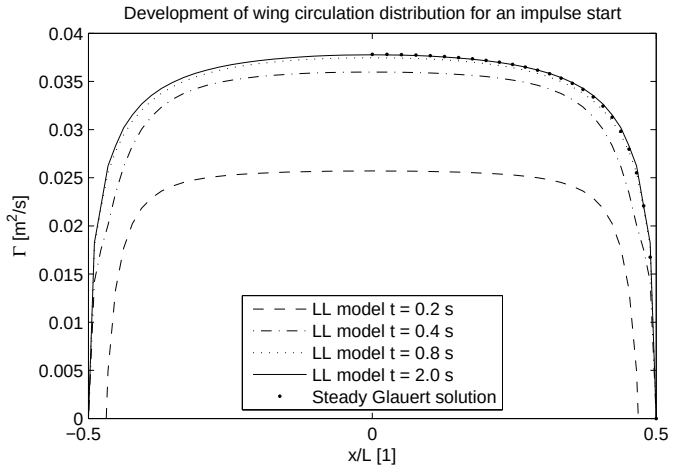


FIGURE 6.5: Development of the bound circulation over time during impulse start.

For the comparison, one of the many measured conditions was selected. Mean angle of attack was 3.96° and amplitude of oscillation 4.25°. Other parameters were: $c_\infty = 102.26\,m^{-1}s$, $f = 14.04\,Hz$. The experimental [48] and lifting line model (numerical) results of the local section lift coefficient vs. angle of attack are plotted in Fig. 6.6 at 25% and 80% span position. As can be seen the results agree very well as far as the lift slope is concerned. The width of the $c_l$ vs. $\alpha$ loop agrees well for 80% section close to the tip and is a bit overestimated for the root section compared to experimental results.

The behavior of the unsteady force-free wake is demonstrated on a similar case with higher frequency of oscillation $f = 40\,Hz$, mean angle of attack 0° and amplitude of oscillation 10°. Although there is no experimental data to compare to, the shape of the wake is plotted in Fig. 6.7

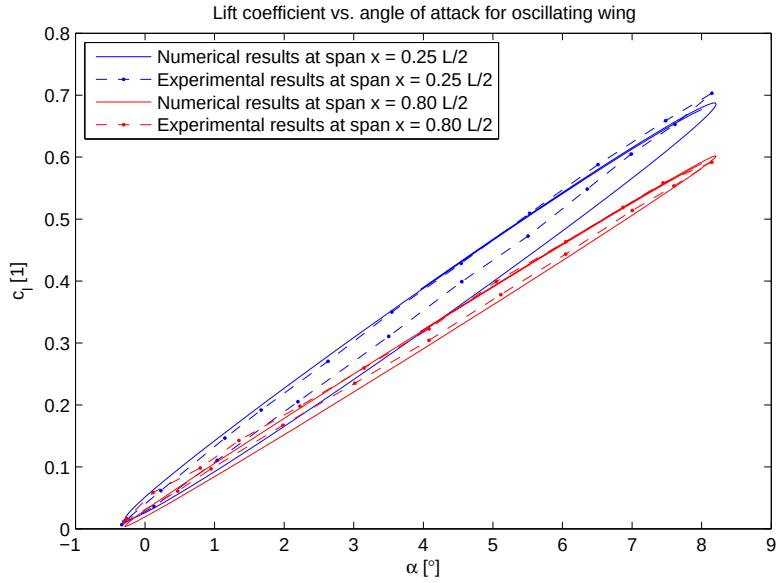


FIGURE 6.6: Comparison of experimental (Source:[48]) and numerical data for oscillating finite wing.

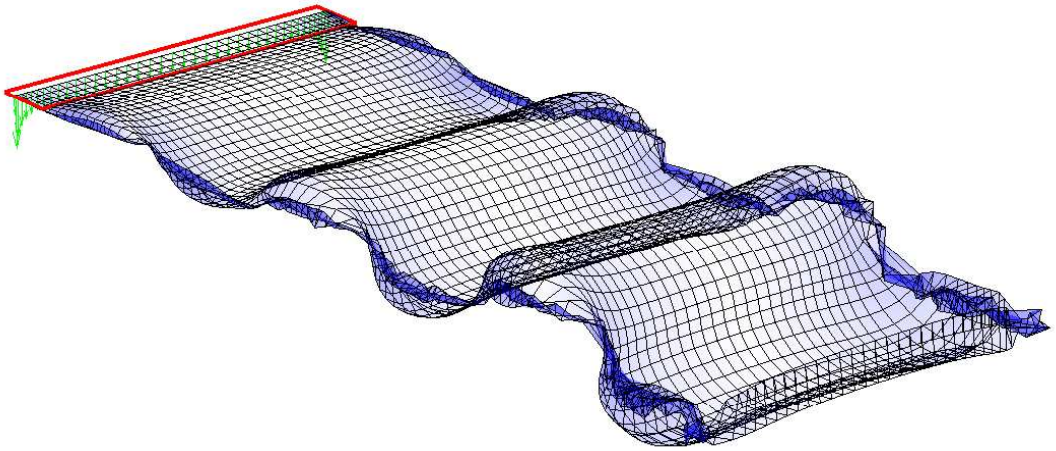

FIGURE 6.7: Wake of an oscillating wing with high oscillation frequency and large pitch angle amplitude.

## 6.2 Model based on 3D panel method

For the three dimensional model of the propeller blades, velocity formulation (Direct, Hess-type formulation) of panel method using quadrilateral panels was chosen. Two types of singularity distributions over the panels are used. Each panel consists of a rectangular vortex ring coinciding with the four panel edges and a constant strength source panel. The vortex ring is equivalent to a constant doublet distribution. One of the advantages of a vortex ring panel is the fact that it can be twisted. The formula for

the influence of this panel is simply the sum of the influences of all 4 edges, which are straight filament segments described by Eq. (5.13).

The constant strength source panel is formulated according to Smith and Hess [36], and Hess [34]. The formulas are rather lengthy and are given in Appendix A. The formulas are valid only for flat panels so the panel is artificially flattened before the source panel induced velocity is calculated.

Some experiments with using only doublet panels on a wing showed, that although the resulting velocity field fulfills the boundary condition of zero normal velocity across panels, the resulting velocities near the trailing edge are not physical. Of course, source panels alone produce solution without circulation over the wing and cannot be used for lifting bodies. Therefore both types of panels must be used at the same time.

### 6.2.1 Surface mesh of a lifting body

Quadrilateral panels forming a structured surface mesh were chosen as the basic elements. Every simple wing or a blade can be unwrapped into a 2D mesh. This 2D mesh is consistent with 2D matrices which store the geometry data. Matrix rows represent the data in the streamwise direction and matrix columns represent the data in the spanwise direction. There are $M \times N$ panels, each with a collocation point placed in the panel center. Collocation point is the place where the evaluation of boundary condition takes place. There are $(M+1) \times (N+1)$ panel corners (nodes). The data structure that was developed for this 3D panel method model is shown in Figs. 6.8 and 6.9.

The trailing edge can have either small finite thickness (in this case the wake begins in the middle of the T.E. gap) or it can be sharp (in this case the dummy panel area reduces to zero). The dummy panel row is in fact only a helper object which helps to overcome the problem with finite edge thickness, where the lower T.E. panel coordinates do not coincide with the wake panel coordinates. The circulation strength and source strength density are both set to zero for the dummy panels.

The wake panels are different from the rest of the panels. First, the source strength density is set to zero for all wake panels. Second, the wake panel circulation strength is not treated as an unknown, but is set as the difference between the circulations of corresponding upper T.E. and lower T.E. panels. This is just an implementation of three dimensional Kutta condition (Eq.(3.26)) in a discretized form. The length of the wake panels in the streamwise direction can be set to several chord lengths, which produces a steady solution with frozen wake shape. For an unsteady case of a finite wing or

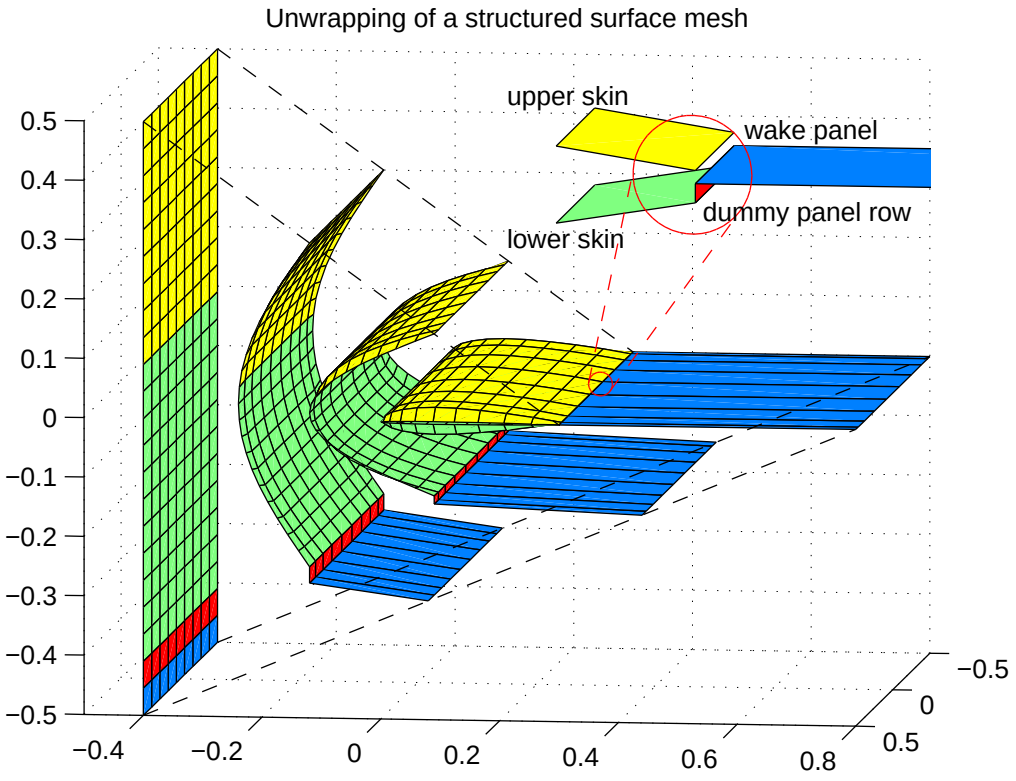


FIGURE 6.8: Structured surface mesh of a wing (applies also to a propeller blade).

for rotating blades the wake panel is rather short and is connected to the wake model described in previous chapter (Chapter 5).

The upper skin and lower skin panels are the same panels from the algorithmic point of view, they were only assigned different color in Fig. 6.8 for better clarity.

### 6.2.2 Single body steady case solution procedure

The procedure of the steady case solution is shown in the diagram in Fig. 6.10. Each of the steps will be described briefly in the following paragraphs.

**Step 1 - Mesh.** In the first step the mesh is created as a series of 2D airfoil shapes with the same number of segments. For each span section, different airfoil with different chord length and quarter chord position can be used. This way virtually any shape of a blade or a wing can be created including swept blades of arbitrary planforms. To produce a smooth mesh, the spanwise variations in chord length, quarter chord location and airfoil shape must be as smooth as possible. The collocation points $\vec{P}_{c,i,j} = [x_{c,i,j}, y_{c,i,j}, z_{c,i,j}]$ are calculated as the mean value of corner point coordinates $\vec{P}_{i,j} = [x_{i,j}, y_{i,j}, z_{i,j}]$.

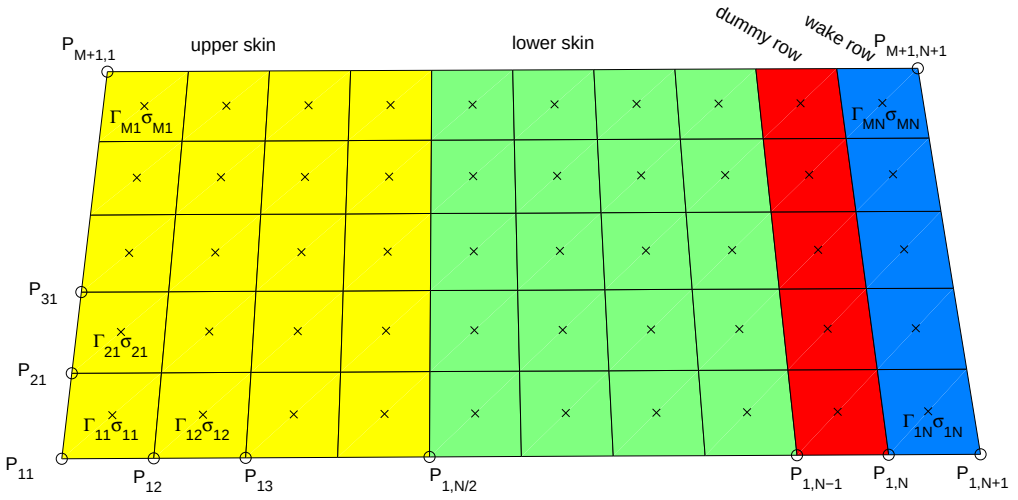


FIGURE 6.9: Unwrapped 2D mesh corresponds to geometry stored in a matrix data structure.

$$x_{c,i,j} = 0.25(x_{i,j} + x_{i+1,j} + x_{i+1,j+1} + x_{i,j+1}), \tag{6.10}$$

$$y_{c,i,j} = 0.25(y_{i,j} + y_{i+1,j} + y_{i+1,j+1} + y_{i,j+1}), \tag{6.11}$$

$$z_{c,i,j} = 0.25(z_{i,j} + z_{i+1,j} + z_{i+1,j+1} + z_{i,j+1}). \tag{6.12}$$

The panel normal vector is calculated as the vector product of the two vectors connecting diagonal corners of the panel. One half of the length of the normal vector is stored as the panel area and then the normal vector is normalized by its length to produce unit normal vector $\vec{n}_{i,j}$.

**Step 2 - Local velocity.** The whole calculation occurs in a translating but non-rotating frame of reference. For a forward moving wing, the frame of reference is fixed to the wing. In case of a rotating propeller blade, the frame of reference is connected to the axis of rotation but does not rotate. In case of an oscillating wing, the frame of reference is connected to the wing's axis of oscillation, but does not oscillate. The local velocity $\vec{c}_{loc}$ at each collocation point is calculated as the sum of free stream velocity (due to translation), which is the same for every point, and relative rotational velocity, which is generally different at each point. The local velocity in this sense is the undisturbed velocity seen at collocation point coordinates without the influence of the body.

**Step 3 - Source panel velocity influence.** For each panel at position i,j on the surface, the influence of this panel on all the collocation points in the domain is computed. The number of panels is $m = M \cdot N$, the number of collocation points

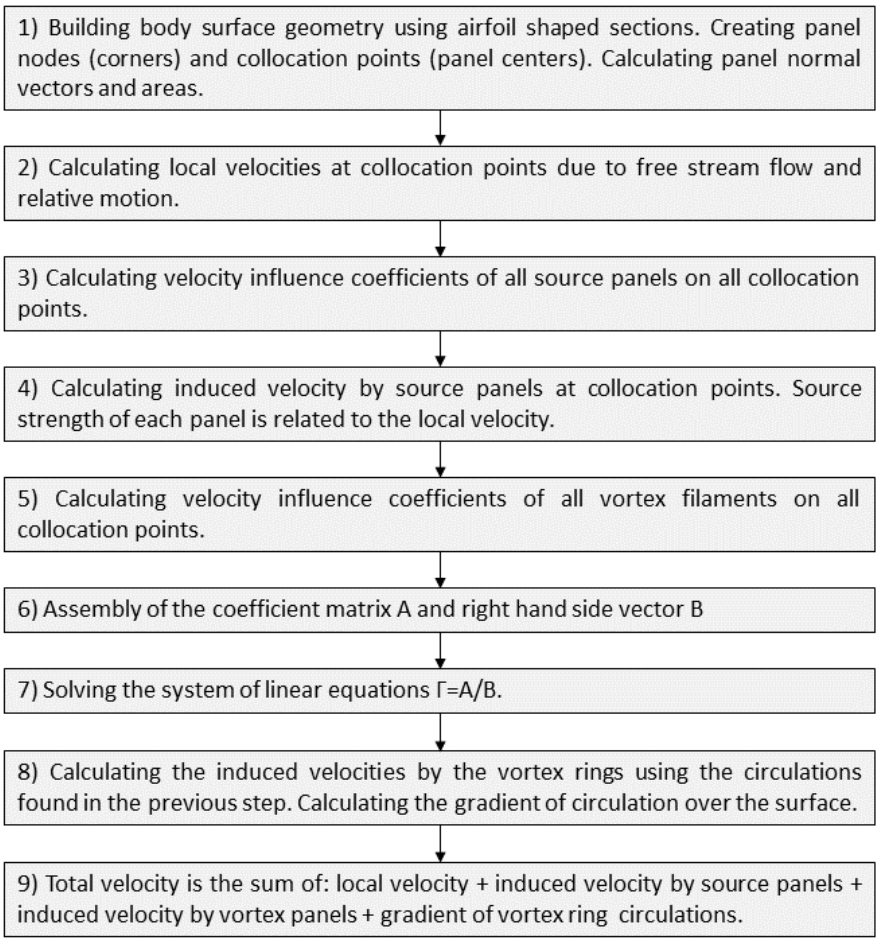


FIGURE 6.10: Block diagram of a steady 3D panel method calculation.

is the same $n = M \cdot N$. For the purpose of influence coefficient calculation, the panels are re-indexed with new single index $J = 1, 2, ..., m$; $J = M(j-1)+i$ and collocation points are indexed accordingly by $I = 1, 2, ..., n$.

Since unit source strength density is used in the formula for induced velocity (Appendix A), the result are three influence coefficient matrices $C_{x,I,J}, C_{y,I,J}, C_{z,I,J}$ depending solely on the geometry. These coefficients have a physical meaning of velocity components induced at I-th collocation point by a panel with source strength density $\sigma_J$ equal to 1 m/s. If the collocation points lies directly on the panel (important case of self influence, which happens when $I = J$) the induced velocity has direction of the panel normal and magnitude $c_n = \pm\sigma/2$ which is a limiting case of normal distance $\bar{z} \to \pm 0$ .

**Step 4 - Induced velocity by source panels.** The main purpose of the source panel is to remove the normal velocity component. As desribed in [A 4], the vortex elements alone are not sufficient to produce smooth and accurate pressure distribution. If the normal-to-panel component of local velocity is used to set the source

strength density (according to the computer program PMARC [49]), the resulting velocity field does not satisfy perfectly the boundary condition, but removes most of the normal flow through the panel without the need of solving system of equations. The formula for calculating source strength density in Eq. (6.13) [49].

$$\sigma_J = -\vec{n}_J \cdot \vec{c}_{loc,J}. \tag{6.13}$$

Panels with such source strength density would cancel out the normal velocity nearly perfectly only in case of a thin wing and symmetric flow, but combined with vortex panels it is sufficient for arbitrary geometries. At this point the source strength of last two panel rows (Dummy row and wake row) is forced to be zero. The resulting velocity at point $I$ due to source panels needs to be calculated as follows:

$$\vec{c}_{\sigma,I} = [C_{x,IJ} \cdot \sigma_J,\ C_{y,IJ} \cdot \sigma_J,\ C_{z,IJ} \cdot \sigma_J]. \tag{6.14}$$

**Step 5 - Vortex filament velocity influence.** In order to save some computational time, the vortex ring panels with 4 edges each are not calculated separately, since every edge (except at the mesh border) is shared by two neighboring panels. Instead, the induced velocities of $(M + 1) \cdot N$ streamwise vortex segments and $M \cdot (N + 1)$ spanwise segments are calculated. Again, unit circulation is used to produce geometric influence coefficients, which have a physical meaning of induced velocity by a vortex filament with unit circulation.

**Step 6 - Constructing system of equations** Again, and for the last time, the linear indexing of $J - th$ vortex ring panel and $I - th$ collocation point is used. As in the case of source panels, there are $m = M \cdot N$ panels and $n = M \cdot N$ collocation points. First, the influence coefficient matrices of $J-th$ panel on $I-th$ collocation point $A_{x,IJ}, A_{y,IJ}, A_{z,IJ}$ are computed as the sum of the influences of all four edges (vortex filament segments) calculated in previous step. Now it is time to construct the system of equations. For every collocation point, the total velocity component normal to the surface should be zero.

$$A_{x,IJ} \cdot n_{x,J} + A_{y,IJ} \cdot n_{y,J} + A_{z,IJ} \cdot n_{z,J} + (\vec{c}_{\sigma,I} + \vec{c}_{loc,I}) \cdot \vec{n}_I = 0. \tag{6.15}$$

This leads to a system of equations $A \cdot \Gamma = \vec{B}$ where the coefficient matrix $A$ is:

$$A_{IJ} = A_{x,IJ} \cdot n_{x,J} + A_{y,IJ} \cdot n_{y,J} + A_{z,IJ} \cdot n_{z,J}. \tag{6.16}$$

and the right hand side vector $\vec{B}$ is:

$$B_I = -(\vec{c}_{\sigma,I} + \vec{c}_{loc,I}) \cdot \vec{n}_I. \tag{6.17}$$

The system of equations is not ready for solving yet. First, the boundary condition should not be evaluated at the dummy panel row and wake panel row. Coefficients representing the influence of these panels are positioned conveniently at the bottom of the matrix and r.h.s vector, so dropping last $2M$ rows will remove the unnecessary set of equations. Now the matrix of coefficients has size $(m-2M)\cdot n$ and new right hand side vector $\vec{B}^*$ is $(m-2M)$ members long.

After this operation, there are more matrix columns ($n = M \cdot N$) than there are rows ($M \cdot N - 2M$), which means too many unknowns. The circulation $\Gamma_J;\ J = n-2M+1, ..., n-M$ at dummy panels should not be computed (it is zero), so these M columns are removed from the matrix.

The circulation of wake panels is a linear combination of upper trailing edge and lower trailing edge panels circulation (Kutta condition). Either an additional set of $M$ equations needs to be added to the system to express this relationship, or the matrix columns corresponding to the wake panels (last $M$ columns) are removed and added to the corresponding columns of upper and lower trailing edge panels. The latter approach is used, which can be expressed programmatically as:

$$A^*_{IJ} = A_{IJ},\ \text{where: } I = (1, ..., m-2M),\ J = (1, ..., n-2M)$$
$$\text{- dropping last 2M rows and columns} \tag{6.18}$$

$$A^*_{IJ} = A^*_{IJ} - A_{KL},$$
$$\text{where: } I, K = (1, ..., m-2M),\ J = (1, ..., M),\ L = (n-M+1, ..., n-2M)$$
$$\text{- subtracting wake coefficients from upper trailing edge panel coefficients} \tag{6.19}$$

$$A^*_{IJ} = A^*_{IJ} + A_{KL},$$
$$\text{where: } I, K = (1, ..., m-2M),\ J = (n-3M+1, ..., n-2M),\ L = (n-M+1, ..., n-2M)$$
$$\text{- adding wake coefficients to lower trailing edge panel coefficients} \tag{6.20}$$

$$B^*_I = B_I,\ \text{where: } I = (1, ..., m-2M) \text{ - dropping last 2M members from r.h.s} \tag{6.21}$$

**Step 7 - Solving the system of linear equations.** The coefficient matrix $A^*$ and right hand side vector $\vec{B}^*$ defined in previous step form a system of $m-2M$

equations with $m - 2M$ unknowns. By solving the system of linear equations the unknown values of circulation are found.

$$\Gamma_I^* = (A^{*-1})_{IJ} \cdot B_J^*. \tag{6.22}$$

**Step 8 - Calculating the vortex panel induced velocities.** After the unknown circulations of panels on the surface of the lifting body are found, the circulations of the dummy panels are set to zero and the circulations of the wake panels are set to $\Gamma_w = \Gamma_{lowerT.E.} - \Gamma_{upperT.E.}$ according to Kutta condition. After this operation, circulation $\Gamma^*$ of all $n = M \cdot N$ panels is known and the induced velocities at $I = (1, ..., m)$ collocation points can be calculated as:

$$\vec{c}_{\Gamma,I} = [A_{x,IJ} \cdot \Gamma_J^*,\ A_{y,IJ} \cdot \Gamma_J^*,\ A_{z,IJ} \cdot \Gamma_J^*]. \tag{6.23}$$

The induced velocity of the vortex rings is calculated correctly everywhere but near the surface. The surface gradient of $\Gamma$ needs to be calculated to correct the induced velocity at the surface:

$$\vec{c}_{\nabla\Gamma} = \frac{\nabla\Gamma}{2}. \tag{6.24}$$

**Step 9 - Calculating the total velocity.** The total velocity due to free stream, relative motion, source panels and vortex panels is calculated as the combination of all these components:

$$\vec{c} = \vec{c}_{loc} + \vec{c}_{\sigma} + \vec{c}_{\Gamma} + \vec{c}_{\nabla\Gamma}. \tag{6.25}$$

### 6.2.3 Mesh sensitivity

Mesh sensitivity study is carried out on a case of a finite wing. Chord is divided into 4 to 30 segments in 7 incremental steps which produces 8 to 60 panels around the airfoil. The span is also divided into 8 to 60 panels.

The chordwise node distribution in this mesh sensitivity study and also the one used throughout the whole work is half-cosine. Half-cosine distribution (dense at leading edge, sparse at trailing edge) is given by the formula $x = 1 - \cos\theta$ with a constant spacing of angle $\theta \in (0, \pi/2)$. This distribution is very commonly used for its good behavior with panel methods since the round leading edge with pressure peaks is covered with denser mesh.

Two types of spanwise node distributions and their combinations are used in this work. One of them is a simple linear distribution, the other one is full cosine spacing $x = (1 - \cos\theta)/2;\ \theta \in (0, \pi)$. In this mesh sensitivity study, a linear combination of 50% constant and 50% cosine distribution has been used.

The influence of chordwise and spanwise paneling density is examined separately on $7 \times 7$ combinations of chordwise and spanwise paneling densities (cell counts). The smallest surface mesh contains 64 panels while the largest mesh contains 3600 panels. The results are plotted as a surface of lift force error in Fig. 6.11.

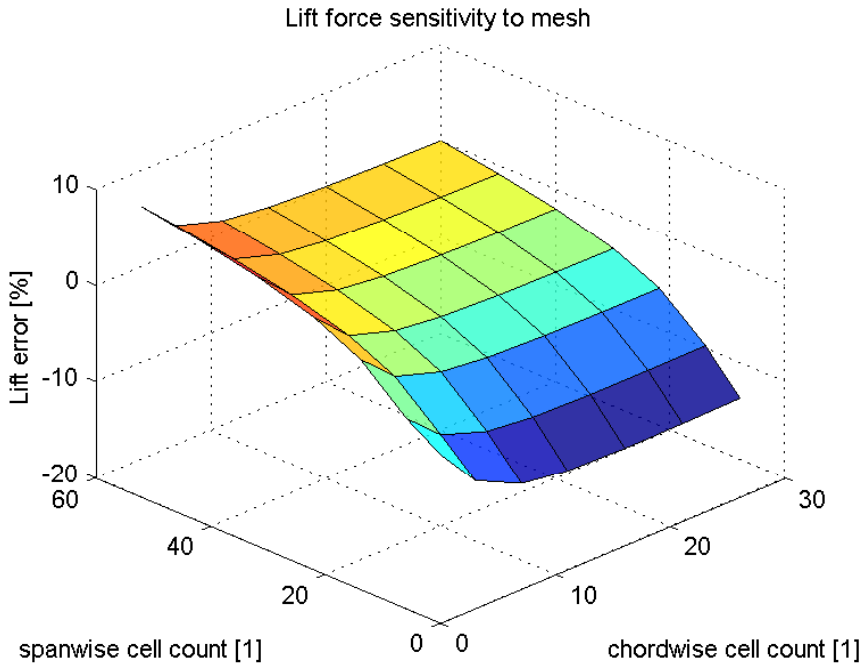


FIGURE 6.11: Spanwise and chordwise mesh sensitivity.

### 6.2.4 Validation of a steady 3D panel method

The computational model is tested on a finite wing case consisting of a body modeled by a 3D panel method with steady (predetermined, "frozen") wake panels reaching a sufficient distance behind the wing. The scenario is the same as in the case of lifting line model validation. Finite wing with NACA0012 cross section and aspect ratio 5 is under 5° angle of attack. Both rectangular and elliptic wings are tested.

As can be seen from the results in Fig. 6.12 the 3D panel method under predicts the overall lift and there is a small yet important difference in the circulation distribution near the tip of the rectangular wing. This difference is in fact a shortcoming of the lifting line idealization. As shown by Sørensen et al. [50], the error is introduced by the blade

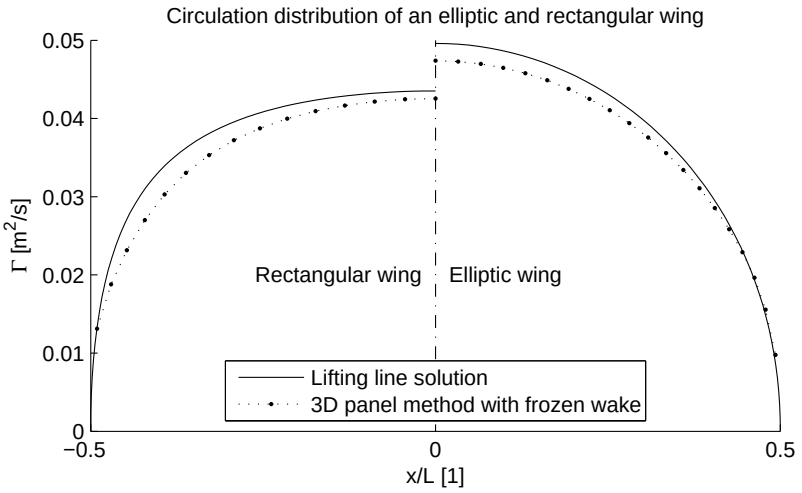


FIGURE 6.12: Comparison of a lifting line and 3D panel method results for finite wing.

being represented by a line instead of a surface. The author also explains a workaround model, that he calls decambering approach, which is quite similar to the lifting surface theory.

A NACA0012 rectangular wing circulation distribution calculated using CFD can be found in [51]. The results of this work also show a similar small deviation of computed lift distribution from the lifting line theory.

### 6.2.5 Unsteady case solution procedure for K bodies

The solution procedure is similar to the steady case except the global time stepping iteration procedure that will be described in detail on the case of several rotating blades. The simplified block diagram of the solution process is in Fig. 6.13.

**"Step 0" - Initialization** Each blade is initialized in its starting position, together with a short row of wake panels in the direction intersecting the trailing edge angle. These wake panels belong to the 3D panel method blade model and serve as a link between this 3D blade model and the force-free wake model described in the previous chapter. The border between wake panels belonging to the 3D panel method blade model and the wake panels belonging to the unsteady force-free wake model is marked with red line in Fig. 6.14 and will be called the wake connection line.

Also, during this step, the first force-free wake panel row is created by shifting the nodes of the wake connection line downstream.

**Step 1 - Body rotation** The body rotation is handle by a standalone function, which first rotates the body by specified angles around $x, y, z$ axes. When the body

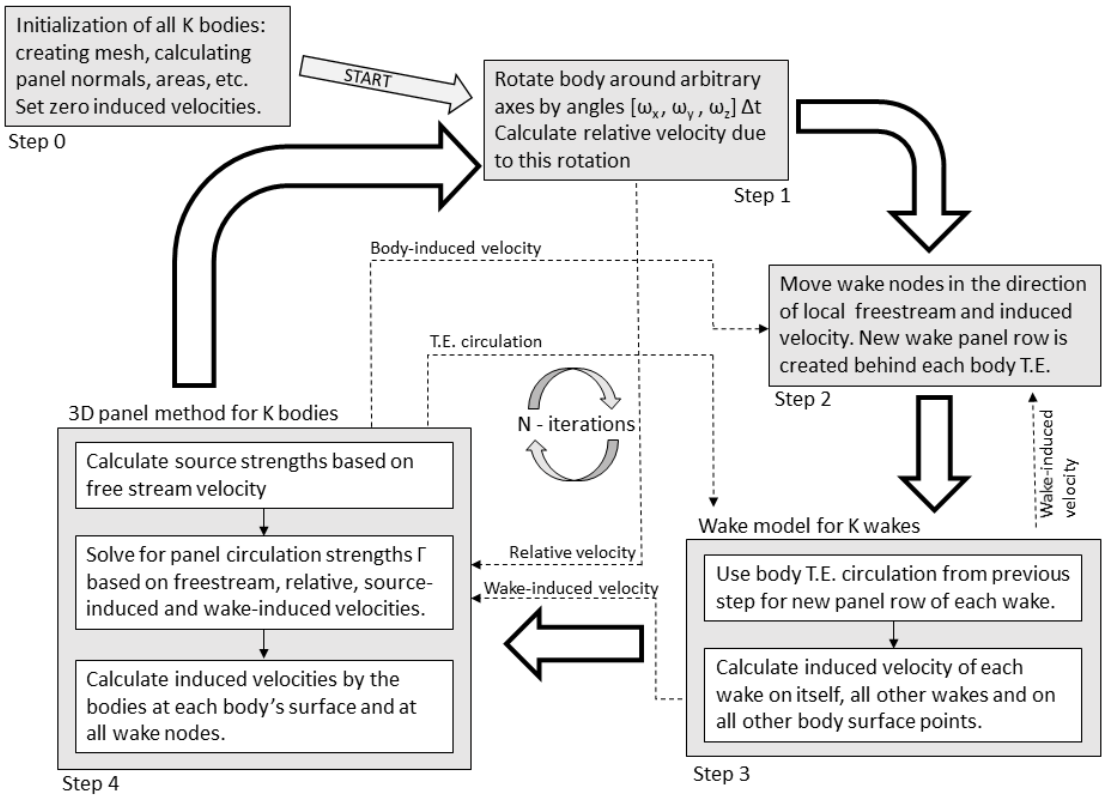


FIGURE 6.13: Simplified block diagram of the developed unsteady solver.

is rotated into new position, the local relative velocity due to this rotation is calculated.

**Step 2 - Wake convection** The principle of wake convection can be seen in Fig. 6.14. The wake nodes are convected in the direction of total velocity at each node, calculated as the sum of free-stream, self-induced and body-induced velocities calculated in previous iteration. The magnitude of the node shift is proportional to the time step.

**Step 3 - Wake model** In this step the induced velocities by the wake on itself, on all other wakes and on all bodies are calculated. The new wake panel row created in previous step is assigned circulation of the trailing edge wake panels of the body from previous iteration.

**Step 4 - 3D panel method** The calculation procedure for the body using 3D panel method is very similar to the steady case described earlier. The only notable difference is that the velocity induced by the wake model must be added to the surface velocity induced by source panels, and to free stream and relative velocities, before the system of equations for finding the vortex panel circulation is solved.

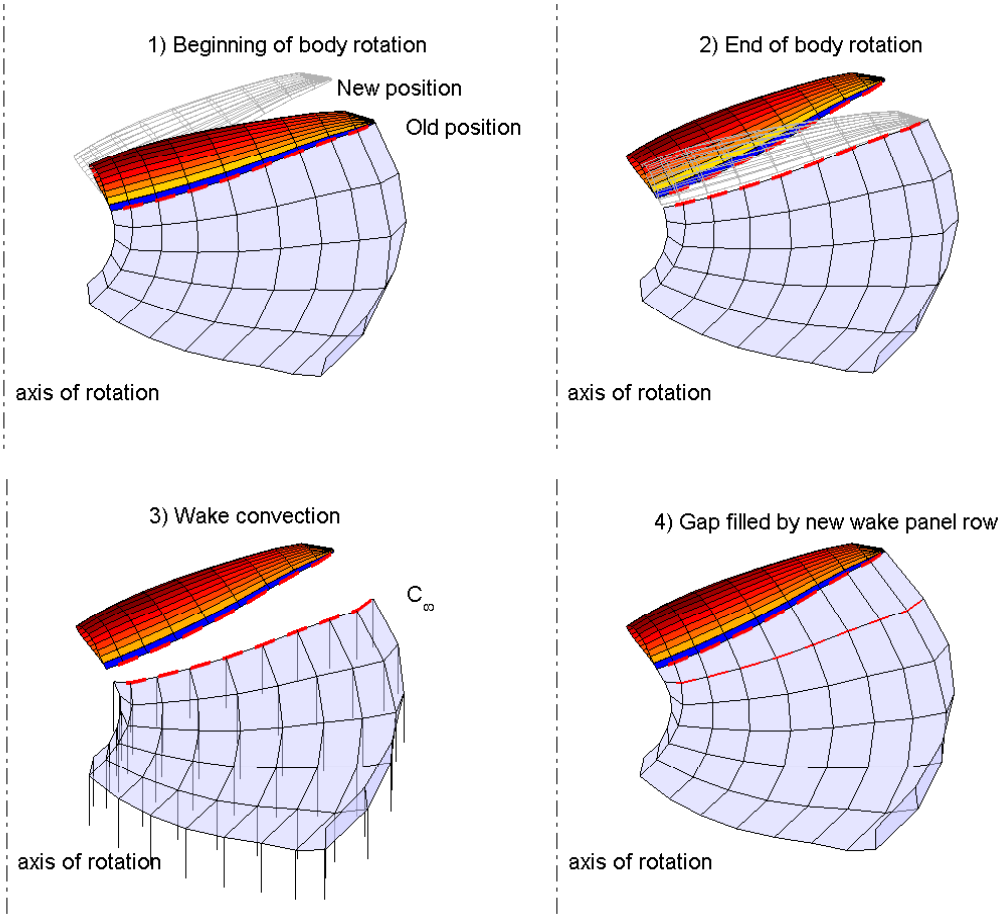


FIGURE 6.14: Body to wake linkage has 4 phases.

### 6.2.6 Rectangular wing set to a sudden motion

The unsteady case of a rectangular wing set to a sudden motion quickly converges to a solution provided by the steady 3D panel method (Fig. 6.12). The difference between the steady and unsteady case is mainly in the shape of the wake, which can be seen in Fig. 6.15. The different shape of the wake in this case does not cause any significant difference in circulation distribution.

### 6.2.7 Oscillating rectangular wing

The case of oscillating wing calculated by 3D panel method is set up the same way as in case of the oscillating wing simulated by lifting line (See Section 6.1.6) The plot of lift coefficient vs. angle of attack in Fig. 6.16 shows again good agreement with experiment. The calculated maximum lift is a bit overestimated (which is a common case with panel methods). Also the width of the lift curve at 25% of half span is greater in case of numerical result compared to the experiment. Except the slight lift

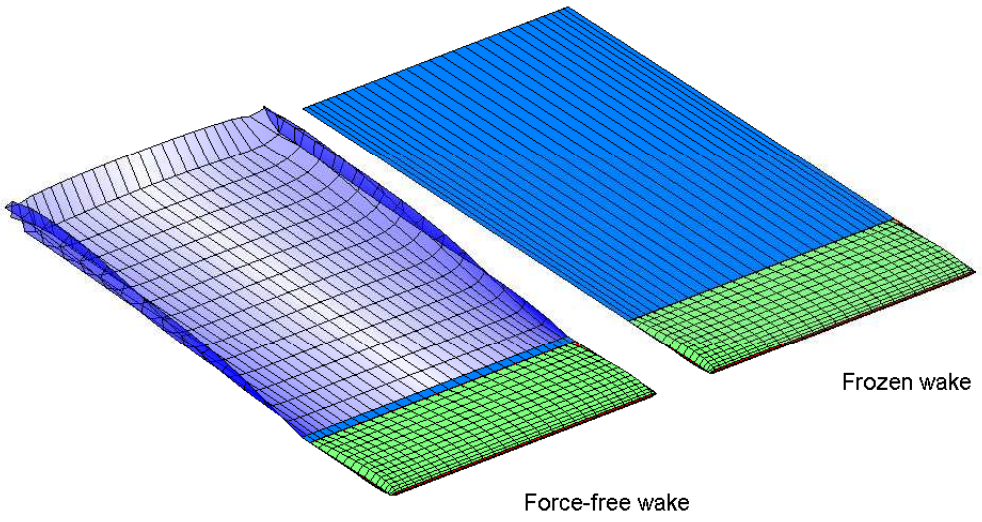


FIGURE 6.15: Difference between a frozen wake and a fully unsteady force-free wake.

over prediction, the results are the same as in lifting line model validation (compare to Fig.6.17). Qualitatively, the wake behind a body looks very similar to the one behind the lifting line (compare Fig. 6.7 and Fig. 6.17). Closer examination reveals larger wake sheet amplitude behind wing modeled by panel method, which is due to the fact that the wing's trailing edge emitting unsteady wake is actually flapping (moving up and down), while the lifting line model has no such movement.

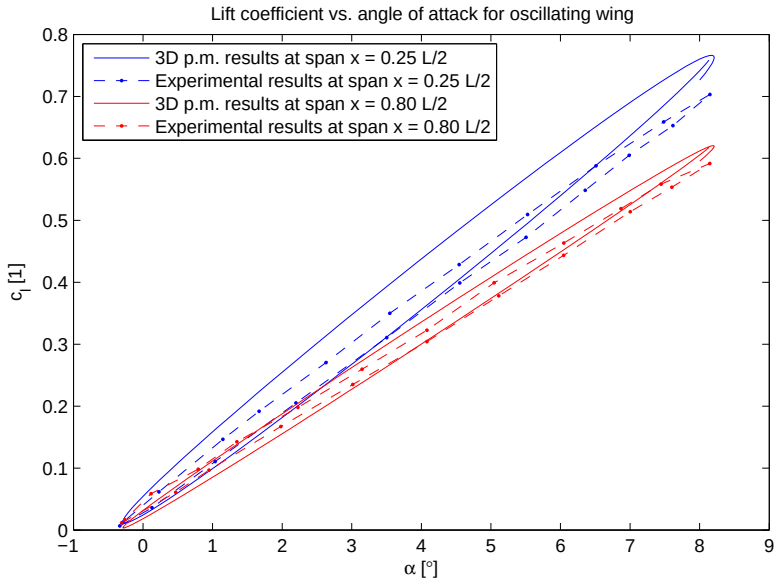


FIGURE 6.16: Comparison of experimental (Source:[48]) and numerical results of panel method for oscillating finite wing.

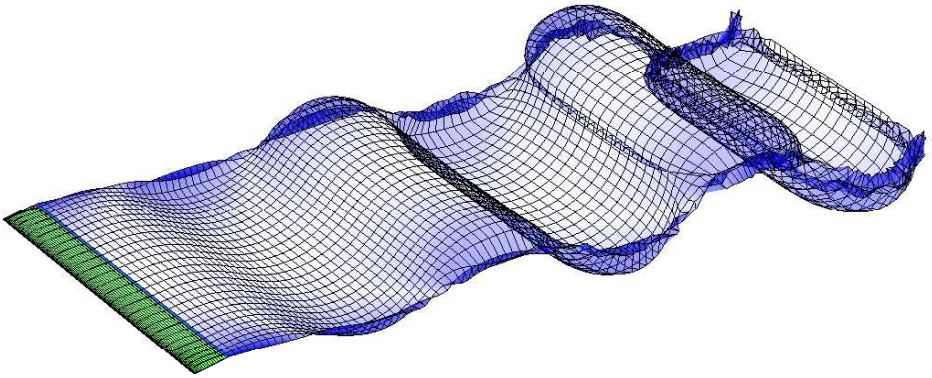

FIGURE 6.17: Wake of an oscillating wing with high oscillation frequency and large pitch angle amplitude.

### 6.2.8 Application to propeller blades

Several issues have to be solved in order to apply the computational model to propeller blades and specifically to contra-rotating propellers. These issues and their solutions are discussed in the following paragraphs, whereas the results of simulations are provided in a separate chapter (Chapter 9), since simulation of propellers is the main interest of this work.

Propeller geometry must be modified to remove problematic root section. A procedure named "wake blow off" helps to solve the issue of low aspect ratio wake development. Blade-to-wake interaction is observed in detail to minimize singularity effects. Finally, some measures are taken to reduce the computational time without affecting calculation precision.

#### 6.2.8.1 Blade root modification

The geometry of upwind propeller from propeller set PS1 was used for single blade calculations. First measure that had to be taken was a modification of the root section to better suit the computational model. In propellers, inner 25% of the radius is providing fraction of the total thrust due to low circumferential velocity. To maintain a constant thrust distribution all the way from tip towards the axis of rotation, the root section would have to have an infinite chord length. For these two reasons the root section of a propeller is not streamlined but it is designed with regards to stiffness and to fit easily into a propeller hub. There are two options to deal with the root section and avoid separated flow over bluff body. One option is to create a hub body and extend

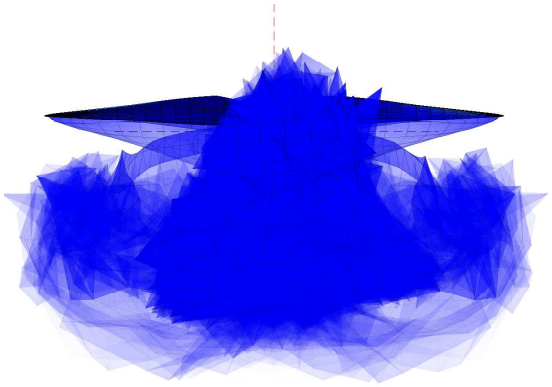

FIGURE 6.18: Wake behind propeller, without wake blow off.

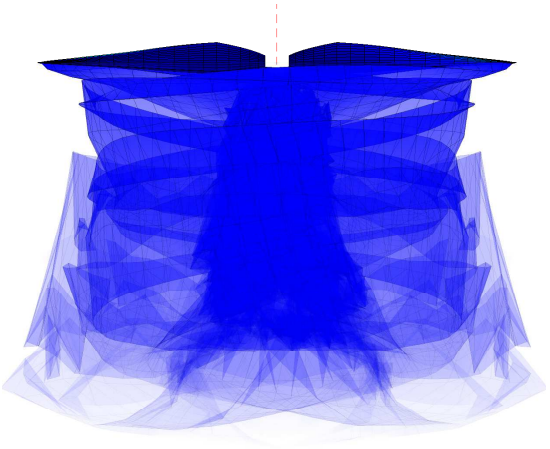

FIGURE 6.19: Wake behind propeller, with wake blow off.

the propeller blade from the hub. The other option, which was chosen, is to provide a modified root ending of the propeller blade and treat each blade as a finite wing.

#### 6.2.8.2 Wake blow off

Each calculation starts with the propeller(s) sudden start of rotation. Starting vortex forms behind each blade and it is convected in the direction of the flow, until it disappears at a predetermined time (age). For advance ratios close to zero, the wake motion is dictated strictly by the induced velocity of the wake, which is, however, not developed at the beginning of calculation. As a result, the vortex wake represented by vortex filaments stays in the propeller disc region and tends to loose stability before it is sufficiently developed to produce reasonable induced velocity through the propeller disk. This does not happen in case of moderate advance ratios, where the wake is convected downstream and retains its shape.

To correct this behavior, a procedure that can be described as "wake blow off" is performed for low advance ratio calculations. At the beginning of calculation, advance ratio is set to some reasonable value, such as $\lambda = 0.1$. During calculation, the advance ratio is gradually reduced to the desired value of advance ratio, which can be zero or even negative. This helps to keep the initial wake stable. The evaluated performance parameters are obtained from data sample of last one or two revolutions, where there is no influence of wake blow off procedure on advance ratio. The effect is illustrated in Fig. 6.18 and 6.19 on a case of single propeller, $\lambda = 0$, after 2 rotations.

#### 6.2.8.3 Close interaction between blade and wake

Close interaction between blade and wake occurs when a blade intersects wake of another (upstream) blade or, in some special cases, its own wake. If the blade and wake model were represented by continuous sheets of vorticity and not by a discrete number of vortex filaments, the interaction as seen by the blade would result in sudden jump of induced velocity above and below the wake. The wake sheet would be simply deformed by the passing blade which would help to promote any existing instabilities in the wake. Because the wake and body are modeled by discrete vortex filaments, the induced velocity is realistic only around collocation points. Almost everywhere else in the close proximity of the wake or body surface, induced velocity can reach virtually any value up to infinity. Without proper treatment, this could lead to unphysical break-up of the wake and to erroneous singularity distribution on body surface.

In the presented computational scheme, the wake takes advantage of the standard wake core growth model (see Chapter 5), which means that a short distance behind the trailing edge of the blades the wake core is already sufficiently large to prevent inducing unphysical velocities on the 3D panel body's collocation points. The vortex ring panels on the blade surface, on the other hand, could induce unrealistic velocities on the wake points. This is prevented by introducing viscous core to surface panels as well. Two options of treating the surface panels viscous core were considered. One option is to use an infinitesimal core for calculation of self induced velocities (velocities induced by the body on itself), while using a large core for calculating induced velocities of the body on all wakes. A special treatment would be necessary near the trailing edge, where the body and wake panels are very close, but previously described close interaction measures are not desirable. The second option, which is implemented in current model, uses an appropriate single core size for each vortex filament on the blade surface such that the core is as large as possible without influencing neighboring collocation points.

#### 6.2.8.4 Measures to reduce computational time

To take advantage of MATLAB fast matrix operation, the influence of all vortex filaments on all collocation points in the domain during one time step is computed at once in a large matrix operation. Still, when each of four blades is discretized for example by $20 \times 40$ panels, the computational time becomes prohibitive after approximately 100 time steps, when each of the wakes reaches size $20 \times 100$ panels. This is due to the fact that 23000 vortex filaments are present in the domain which produces influence matrices of size $23e3 \times 23e3$ requiring over 4GB RAM each. To reach a stable and developed unsteady solution and to remove the influence of starting vortex, last wake rows are being

deleted after 100 time steps. Approximately 200 time steps are considered sufficient to produce stable solution with developed wake. Boundary layer computation over the surface of all blades takes about 1 minute on a current i7 computer, which is a fixed value independent of the wake length. To reduce computational time, boundary layer is considered only during last rotation.

#### 6.2.8.5 Propeller performance sensitivity to mesh

Mesh sensitivity of the 3D panel method was performed in Section 6.2.3 for a case of finite wing. Similar sensitivity study is performed here for the case of a single propeller. The main difference is that here the performance of each mesh was computed across all advance ratios using full model including boundary layer to produce performance curves, which are compared. Spanwise and chordwise panel density is not varied independently, but three reasonable combinations were chosen instead. Each blade of the single propeller was discretized by $14 \times 13$ (coarse) $22 \times 19$ (medium) and $38 \times 29$ (fine) mesh panels. Upstream propeller from propeller set PS1 was used for the mesh sensitivity study.

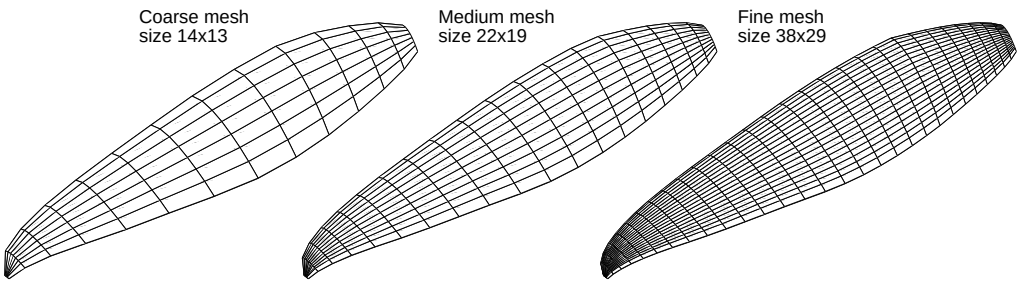


FIGURE 6.20: Three meshes used in mesh sensitivity study.

**Computational cost depending on mesh size for single propeller:**

| Mesh size | blade panels | max blade+wake panels | avg. time step | total time |
|---|---|---|---|---|
| 14x13 | 364 | 2444 | 2.1 sec. | 74 min. |
| 22x19 | 836 | 3876 | 4.7 sec. | 164 min. |
| 38x29 | 2204 | 6844 | 15.12 sec. | 524 min. |

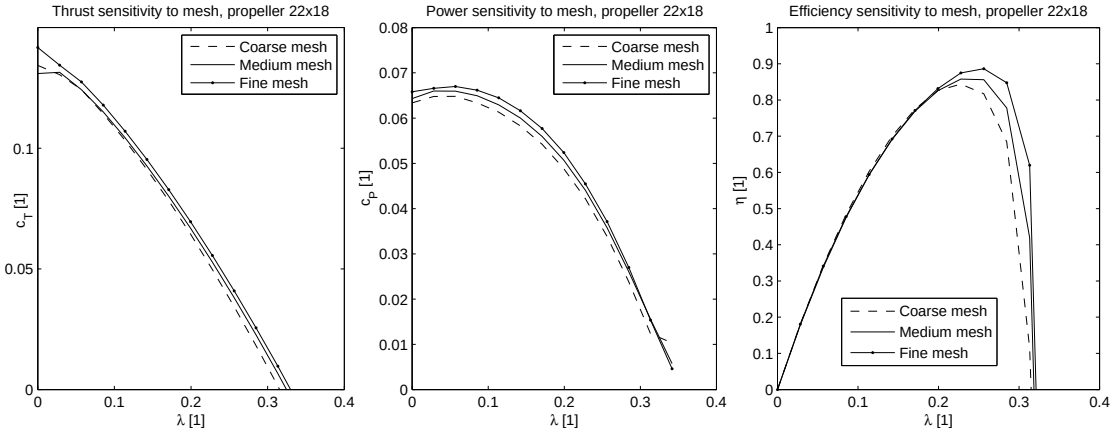


FIGURE 6.21: Sensitivity of propeller performance curves to mesh.

# Chapter 7

# Coupled 2D Integral Boundary Layer Model

## 7.1 Boundary layer model description

The boundary layer model used in this work is based on the work of Drela [33] and Drela and Giles [52], Johansen [53], Green et al. [54], Veldman [55] and Bijleveld and Veldman [56]. Due to the large extent of the topic, the information provided in this thesis is focused on the most important aspects of the model. Detailed description of the model can be found in [A 5].

### 7.1.1 General boundary layer equations

Several simplifications and assumptions are used for describing the boundary layer models. It is important to be aware of their consequences as they are more or less violated in a real boundary layer flow. The boundary layer thickness is assumed to be significantly smaller than the radius of curvature of the body surface. This allows the use of curvilinear coordinates. Also the centrifugal and other volumetric forces are considered small and are neglected. The pressure is considered constant throughout the boundary layer and zero velocity is prescribed at the wall.

The curvilinear coordinates $\xi$, $\eta$ are used, where $\xi$ is the measure of the distance along the surface from the stagnation point and $\eta$ is the distance from the wall in the direction normal to the wall. The velocity $\vec{c}$ has two components $c_\xi$ and $c_\eta$. These components of velocity will be marked in this chapter as $u = c_\xi$ and $v = c_\eta$ according to the most common notation in boundary layer studies.

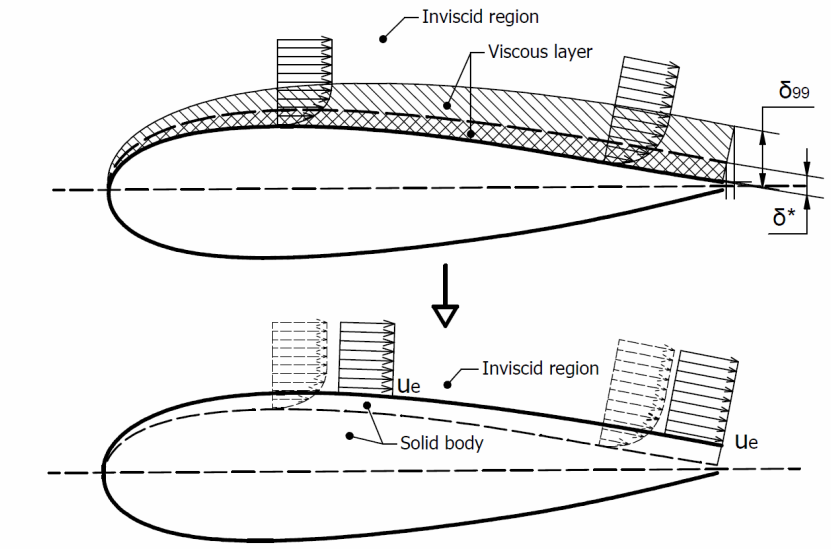


FIGURE 7.1: Solution of the boundary layer problem using viscous and inviscid regions (Figure also used in [A 5]).

The Navier Stokes equations can be simplified using the boundary layer assumptions. For a steady flow they are reduced to [57]:

$$u\frac{\partial u}{\partial \xi} + v\frac{\partial u}{\partial \eta} = -\frac{1}{\rho}\frac{dp}{d\xi} + \nu\frac{\partial^2 u}{\partial \eta^2}, \tag{7.1}$$

$$\frac{\partial u}{\partial \xi} + \frac{\partial v}{\partial \eta} = 0. \tag{7.2}$$

### 7.1.2 Viscous-inviscid boundary layer concept

The method of solution is based on a concept of dividing the fluid into viscous region and inviscid region. In a real flow there is no clear boundary between the boundary layer flow influenced by viscosity and surrounding inviscid flow. For this reason the boundary layer thickness $\delta_{99}$ is introduced, which is defined as the distance from wall, where the velocity reaches 99% of the edge velocity.

The idea of calculating an inviscid flow by replacing the original body by a new solid body with wall at $\delta_{99}$ distance from the original wall would be incorrect, because the velocity flux through the boundary layer would be neglected. To account for the boundary layer flow, the displacement thickness $\delta^*$, which is defined based on conservation of volume flow (or mass in case of compressible flow), is used as the boundary of the inviscid region (See Fig. 7.1). The thickness of the viscous boundary layer region is $\delta_{99}$, where $\delta_{99} > \delta^*$ which means that the two regions overlap.

Boundary layer edge velocity $u_e$ is the velocity at the edge of the viscous and inviscid regions and has the same value for both regions. Edge velocity and displacement thickness are two parameters through which the two regions interact.

### 7.1.3 Boundary layer parameters

**Displacement thickness** is a thickness by which a body in an inviscid flow must be enlarged to obtain the same flow as the flow outside of the boundary layer in case of a viscous flow. Displacement thickness is calculated from mass conservation law as:

$$\delta^* = \int \left(1 - \frac{u(\eta)}{u_e}\right) d\eta. \tag{7.3}$$

**Momentum thickness** $\theta$ is a thickness by which a body must be enlarged in case of an inviscid flow to match the momentum of the viscous flow between the body and a reference point in a sufficient distance from the wall.

$$\theta = \int \frac{u(\eta)}{u_e} \left(1 - \frac{u(\eta)}{u_e}\right) d\eta. \tag{7.4}$$

**Momentum thickness Reynolds number** $Re_\theta$ is a Reynolds number defined based on momentum thickness and edge velocity.

$$Re_\theta = \frac{\rho u_e \theta}{\mu}. \tag{7.5}$$

**Kinetic energy thickness** $\theta^*$ is defined in a similar way as momentum and displacement thicknesses, instead of mass and momentum the conserved quantity is kinetic energy.

$$\theta^* = \int \frac{u(\eta)}{u_e} \left(1 - \frac{(u(\eta))^2}{u_e^2}\right) d\eta. \tag{7.6}$$

These various types of boundary layer thicknesses are not tied through simple relations and their ratios can indicate the shape of the velocity profile and thus the state and properties of the boundary layer. Moreover, several other non-dimensional coefficients in addition to the $Re_\theta$ are defined. They are listed below:

**Shape parameter** $H$ is the ratio of the displacement thickness to momentum thickness.

$$H = \frac{\delta^*}{\theta}. \tag{7.7}$$

**Kinetic energy shape parameter** $H^*$ is the ratio of kinetic energy thickness to the momentum thickness.

$$H^* = \frac{\theta^*}{\theta}. \tag{7.8}$$

**Skin friction coefficient** $C_f$ is a non-dimensionalised wall shear stress $\tau_w$.

$$C_f = \frac{2\tau_w}{\rho u_e^2}. \tag{7.9}$$

**Dissipation coefficient** $C_D$ is a measure of dissipation which occurs across the boundary layer due to shear stress. This dissipation also occurs in the wake, where skin friction coefficient is zero.

$$C_D = \frac{1}{\rho u_e^3} \int \tau \frac{\partial u}{\partial \eta} d\eta. \tag{7.10}$$

**Shear stress coefficient** $C_\tau$ is defined based on the maximum shear stress across the boundary layer.

$$C_\tau = \frac{\tau_{max}}{\rho u_e^2}. \tag{7.11}$$

### 7.1.4 Integral boundary layer model

The 2D integral boundary layer model is strictly speaking a 1D model solving the problem of 2D boundary layer using only one coordinate $\xi$. The integral method approach was first described in the papers by Kármán and Polhausen in 1921 [57]. Key component of the integral boundary layer is a velocity profile, which is parametrized by the boundary layer properties. Example of such velocity profiles are Hartree's profiles [58] derived from the Falkner Skan equation for wedge flows.

The integral boundary layer model was created according to Drela and Giles ([33], [52]) with some modifications.

The first governing equation of the integral boundary layer model is the integral momentum equation:

$$\frac{d\theta}{d\xi} + (2 + H)\frac{\theta}{u_e}\frac{du_e}{d\xi} = \frac{C_f}{2}. \tag{7.12}$$

The second governing equation of the described boundary layer model is the kinetic energy shape parameter equation

$$\theta \frac{dH^*}{d\xi} + H^*(1-H)\frac{\theta}{u_e}\frac{du_e}{d\xi} = 2C_D - H^*\frac{C_f}{2}. \tag{7.13}$$

The primary variables were chosen $H$ and $\theta$ unlike the Drela's model where the primary variables are $\theta$ and $\delta^*$. The edge velocity $u_e$ depends on the boundary layer displacement thickness and inviscid solution and is treated as a function of primary variables $u_e = u_e(H, \theta)$ The remaining parameters of the boundary layer equation are all functions of the primary variables $H^* = H^*(H, \theta)$, $C_f = C_f(H, \theta)$ and $C_D = C_D(H, \theta)$ An auxiliary equation is solved together with the governing equations, which is different for turbulent and for laminar regions.

#### 7.1.4.1 Laminar closure equations

In the laminar region, the following equations are used (simplified equations from[52] with removed compressibility effects):

$$H^* = \begin{cases} 1.515 + 0.076\frac{(4-H)^2}{H}, & \text{for } H < 4 \\ 1.515 + 0.040\frac{(4-H)^2}{H}, & \text{for } H > 4 \end{cases}. \tag{7.14}$$

$$\begin{aligned} C_f &= \frac{2}{Re_\theta}\left(-0.067 + 0.01997\frac{(H-7.4)^2}{H-1}\right) \text{ for } H < 7.4 \\ &= \frac{2}{Re_\theta}\left(-0.067 + 0.022\left(\frac{H-7.4}{H-6}\right)^2\right) \text{ for } H > 7.4. \end{aligned} \tag{7.15}$$

$$\begin{aligned} C_D &= \frac{H^*}{2Re_\theta}\left(0.207 + 0.00205(4-H)^{5.5}\right) \text{ for } H < 4 \\ &= \frac{H^*}{2Re_\theta}\left(0.207 - 0.003\frac{(H-4)^2}{1+0.02(H-4)^2}\right) \text{ for } H > 4. \end{aligned} \tag{7.16}$$

For transition prediction, the $e^9$ method also used in the XFOIL [33] and ISES code [52] is employed. This method is based on observing the amplification of small velocity perturbation in a viscous flow. The modes of these disturbances (waves) are described by the Orr-Somerfeld equation. The $e^9$ method assumes that when the most unstable Tollmien-Schlichting wave is amplified by $e^{\tilde{n}} = e^9 = 8103$, transition occurs. In practice, the value of transition amplification ratio $\tilde{n}_{crit}$ can differ from 9. It can be used for simulating the effect of surface roughness, vibrations and free-stream turbulence on

transition location. The following auxiliary equation for amplification ratio is solved together with governing equations in laminar region:

$$\frac{d\tilde{n}}{d\xi} = \frac{d\tilde{n}}{dRe_\theta}\frac{m+1}{2}l\frac{1}{\theta}, \tag{7.17}$$

where:

$$\frac{d\tilde{n}}{dRe_\theta} = 0.01\sqrt{[2.4H - 3.7 + 2.5tanh(1.5H - 4.65)]^2 + 0.25}, \tag{7.18}$$

$$l = \frac{6.54H - 14.07}{H^2}, \tag{7.19}$$

$$m = \left(0.058\frac{(H-4)^2}{H-1} - 0.068\right)\frac{1}{l}. \tag{7.20}$$

When the value of amplification ratio reaches the predefined critical value $\tilde{n}_{crit}$ the transition occurs and solution switches to turbulent closure equations.

#### 7.1.4.2 Turbulent closure equations

The following closure equations are used for the turbulent region of the boundary layer [52]:

$$H^* = \begin{cases} 1.505 + \frac{4}{Re_\theta} + \left(0.165 - \frac{1.6}{\sqrt{Re_\theta}}\right)\frac{(H_0-H)^{1.6}}{H}, & \text{for } H < H_0 \\ 1.505 + \frac{4}{Re_\theta} + (H-H_0)^2\left[\frac{0.04}{H} + \frac{0.007logRe_\theta}{(H-H_0+4/logRe_\theta)^2}\right], & \text{for } H > H_0 \end{cases}, \tag{7.21}$$

where:

$$H_0 = \begin{cases} 4, & \text{for } Re_\theta < 400, \\ 3 + \frac{400}{Re_\theta}, & \text{for } Re_\theta > 400, \end{cases} \tag{7.22}$$

$$C_f = 0.3e^{-1.33H}[log_{10}Re_\theta]^{-1.74-0.31H} + 0.00011\left[tanh\left(4 - \frac{H}{0.875}\right) - 1\right], \tag{7.23}$$

$$C_D = \frac{C_f}{2}U_s + C_\tau(1 - U_s), \tag{7.24}$$

$$U_s = \frac{H^*}{2}\left(1 - \frac{4}{3}\frac{H-1}{H}\right). \tag{7.25}$$

Instead of amplification rate equation, an auxiliary equation for shear stress coefficient is calculated in the turbulent region. Green et al. [54] proposed a lag-entrainment method which calculates $C_\tau$ based on its equilibrium value $C_{\tau EQ}$ and its spatial rate of change:

$$\frac{\theta(3.15 + H + \frac{1.72}{H-1})}{C_\tau}\frac{dC_\tau}{d\xi} = 4.2(C_{\tau EQ}^{0.5} - C_\tau^{0.5}), \tag{7.26}$$

where:

$$C_{\tau EQ} = H^*\frac{0.015(H-1)^3}{(1-U_s)H^3}. \tag{7.27}$$

### 7.1.5 Solution of the boundary layer equations

In the laminar region, the system of equations consist of only Equations (7.12) and (7.13). Amplification ratio is defined explicitly by Eq. (7.17) and is computed after the system of equations is solved. More complicated situation arises in turbulent region where the auxiliary equation Eq. (7.26) for $C_\tau$ must be solved together with the governing equations in one system. An additional unknown was selected to be $\sqrt{C_\tau}$ instead of $C_\tau$ which simplifies the solution a little. The procedure will be explained for the case of turbulent closure. Newton-Raphson method is used for finding the roots of the following functions (in turbulent region):

$$f_1 = \frac{\theta_i - \theta_{i-1}}{\xi_i - \xi_{i-1}} + (2 + H_{i-1/2})\frac{\theta_{i-1/2}}{u_{ei-1/2}}\frac{u_{ei} - u_{ei-1}}{\xi_i - \xi_{i-1}} - \frac{C_{fi-1/2}}{2} = 0, \tag{7.28}$$

$$\begin{aligned} f_2 = \theta_{i-1/2}\left(\frac{dH^*}{dH}\right)_{i-1/2}\frac{H_i - H_{i-1}}{\xi_i - \xi_{i-1}} + {H^*}_{i-1/2}(1 - H_{i-1/2})\frac{\theta_{i-1/2}}{u_{ei-1/2}}\frac{u_{ei} - u_{ei-1}}{\xi_i - \xi_{i-1}} \\ -2C_{Di-1/2} + {H^*}_{i-1/2}\frac{C_{fi-1/2}}{2} = 0, \end{aligned} \tag{7.29}$$

$$\begin{aligned} f_3 = \frac{2\theta_{i-1/2}(3.15 + H_{i-1/2} + \frac{1.72}{H_{i-1/2}-1})}{C_{\tau_{i-1/2}}^2}\frac{C_{\tau_i}^{0.5} - C_{\tau_{i-1}}^{0.5}}{\xi_i - \xi_{i-1}} \\ -4.2(C_{\tau EQ}{}_{i-1/2}^{0.5} - C_{\tau_{i-1/2}}^{0.5}) = 0. \end{aligned} \tag{7.30}$$

In the above equations, $i$ is the index of current station. The term "station" will be used for each position along streamwise coordinates $\xi_i$ specified by the discretization. The

algorithm proceeds in a downstream-marching fashion such that $i-1$ is the index of previously calculated section, one discretization step upstream from the current station $i$. The method uses central differencing of variables, which means that e.g. $H_{i-1/2} = 0.5H_i + 0.5H_{i-1}$. The Jacobian for the i-th downstream station is:

$$J = \begin{pmatrix} \frac{\partial f_1}{\partial H_i} & \frac{\partial f_1}{\partial \theta_i} & \frac{\partial f_1}{\partial C_{\tau_i}^{0.5}} \\ \frac{\partial f_2}{\partial H_i} & \frac{\partial f_2}{\partial \theta_i} & \frac{\partial f_2}{\partial C_{\tau_i}^{0.5}} \\ \frac{\partial f_3}{\partial H_i} & \frac{\partial f_3}{\partial \theta_i} & \frac{\partial f_3}{\partial C_{\tau_i}^{0.5}} \end{pmatrix}. \tag{7.31}$$

At each downstream station, the variables are initialized by previous station values. Several Newton iterations are required before solution converges. Convergence is judged by the residual values. At station i, n+1 iteration steps is calculated as follows (index $i$ dropped for clarity):

$$J \begin{pmatrix} H_{n+1} - H_n \\ \theta_{n+1} - \theta_n \\ C_{\tau n+1}^{0.5} - C_{\tau n}^{0.5} \end{pmatrix} = \begin{pmatrix} -f_1 \\ -f_2 \\ -f_3 \end{pmatrix}. \tag{7.32}$$

In laminar region the $f_3$ function is dropped and Jacobian matrix has size $2 \times 2$. When transition is detected, shear stress coefficient is initialized to $C_\tau = 0.03$ and calculation continues with turbulent closure equations.

## 7.2 Coupling of the boundary layer model to inviscid solution

The boundary layer displacement thickness, calculated based on edge velocity distribution, influences the solution of the inviscid region, which as a result produces different edge velocity distribution. This interaction of the viscous and inviscid regions can be handled four different ways [55],[53] in order of increasing complexity:

- Direct method: A simple method where the inviscid solution is calculated first, then the boundary layer is computed in the downstream direction. Edge velocity is treated as a constant. New body is created using displacement thickness from boundary layer calculation and the cycle repeats beginning with new inviscid solution.

- Inverse method: Same approach as in direct mode, except the flow solver runs in inverse mode, calculating new geometry for a prescribed velocity field and boundary layer model solves for edge velocity, based on a given displacement thickness distribution from the flow solver.
- Quasi-simultaneous method: A simplified relation between $\delta^*$ and $u_e$ is used as an interaction law. Several passes are needed, however, unlike direct and inverse methods, issues with singularity of solution are avoided.
- Fully simultaneous method: The inviscid flow and boundary layer equations are solved in one large system of equations.

In regions of strong interaction between the two regions, direct and inverse methods fail to converge. This is due to a singular behavior of the governing equations described by Goldstein for conditions near separation [59]. Strong interactions are large changes in displacement thickness that occur near transition, laminar layer separation and reattachment points and near trailing edge (Goldstein singularity). The matter is discussed in more detail in [5]. Quasi-simultaneous method was selected due to the possibility of extending the method to calculating 2D boundary layer of three-dimensional bodies.

### 7.2.1 Interaction laws for quasi-simultaneous method

#### 7.2.1.1 Veldman's interaction law

Properties of various interaction laws were studied by Veldman et al. [55], [60], [56] based on a mathematical analysis of criteria for solution existence. One of the simplest interaction laws is based on the thin airfoil theory and works as follows. For current ("NEW") boundary layer pass, the edge velocity is calculated from the previous ("OLD") boundary layer pass and corresponding inviscid solution:

$$u_{ei,NEW} = u_{ei,OLD} + \frac{4}{\pi(\xi_i - \xi_{i-1})} c_\infty ({\delta^*}_{i,NEW} - {\delta^*}_{i,OLD}). \tag{7.33}$$

In case of first boundary layer pass, ${\delta^*}_{i,OLD}$ is set to zero and $u_e$ is the result of inviscid solution of original body without any wall displacement.

#### 7.2.1.2 New local and global linear interaction laws

The main problem with a simple interaction law above is the fact that it simulates the effect of local wall displacement with a general formula, that does not accurately capture

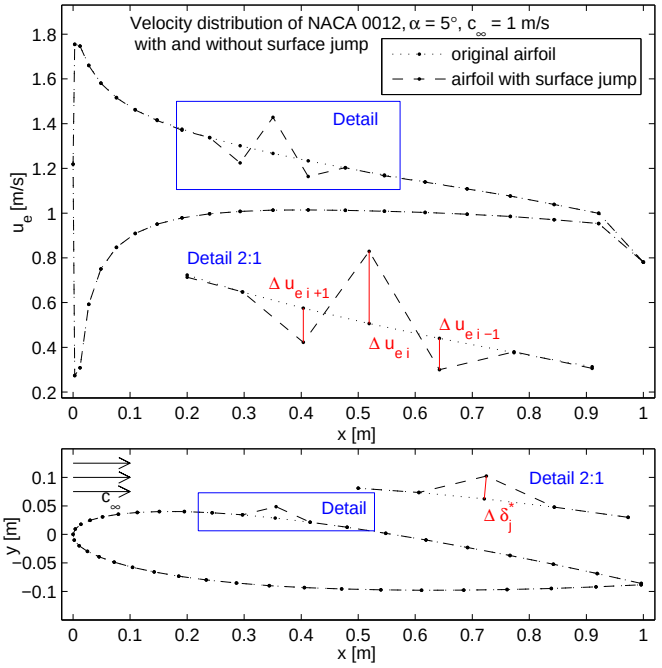


FIGURE 7.2: Response of velocity to surface jump. Note: Surface displacement has been exaggerated for illustration purposes.

the sensitivity of edge velocity to this displacement thickness change. The idea of two new interaction laws, presented by the author in [A 5] was to capture accurately the local interaction of $u_e$ and $\delta^*$ by numerical differentiating of the inviscid panel method results with regards to small change of nodal points position in the direction normal to the surface. (See Fig. 7.2) The influence coefficient $d_{ij}$ of a small displacement of i-th node on edge velocity at j-th collocation point can be accurately calculated by numerical differentiation:

$$d_{ij} = \frac{\partial u_{ei}}{\partial \delta^*{}_j}. \tag{7.34}$$

These interaction coefficients form a response matrix, which can be used for precise determination of new velocity distribution, when the shape of the airfoil changes (with assumption of small displacements of the airfoil surface). An example of such response matrix is presented in Fig.7.3. It was calculated using numerical differentiation for NACA 0012 airfoil at 5° angle of attack, discretized by 17 surface nodes. Important feature of the matrix is a dominating positive main diagonal with still significant negative subdiagonal and superdiagonal. Other members of the matrix have less significant values.

The disadvantage of this method is the fact that N calculations of inviscid solution are needed for creating the $N \times N$ matrix of influence coefficients due to displacement thickness jump, where N is the number of surface nodes. The difference between local

| $d_{ij}$ | j=1 | 2 | 3 | ... | ... | ... | ... | ... | ... | ... | ... | ... | ... | ... | ... | ... | ... | N |
|---|---|---|---|---|---|---|---|---|---|---|---|---|---|---|---|---|---|---|
| i=1 | 8.9 | −5.2 | −1.3 | −1.4 | −1.3 | −1.5 | −1.9 | −3.1 | −6.3 | 2.8 | 1.6 | 1.1 | 0.9 | 0.7 | 0.7 | −0.7 | 8.9 |
| 2 | −3.1 | 12 | −3.9 | 1 | 0.8 | 1.2 | 1.7 | 3.1 | 6.7 | −3.2 | −1.9 | −1.4 | −1.1 | −1.1 | −1.3 | 0.2 | −3.1 |
| 3 | −0.2 | −5.2 | 12.1 | −5.7 | 0 | −0.4 | −0.2 | −0.2 | −0.1 | 0 | 0 | 0 | −0.1 | −0.2 | 0.6 | −0.4 | −0.2 |
| ... | −0.1 | 0.2 | −5.8 | 14.2 | −6.9 | 0 | −0.5 | −0.2 | 0.1 | −0.2 | −0.1 | −0.2 | −0.2 | 0.4 | −0.3 | −0.3 | −0.1 |
| ... | 0 | −0.3 | 0.3 | −7.2 | 17.6 | −9.3 | −0.3 | −1 | −0.8 | 0.1 | −0.1 | −0.1 | 0.4 | −0.2 | −0.2 | 0 | 0 |
| ... | 0 | −0.1 | −0.4 | 0.5 | −9.3 | 23.5 | −13. | −1.1 | −2.1 | 0.1 | 0 | 0.5 | −0.1 | −0.2 | 0 | 0 | 0 |
| ... | 0 | −0.1 | −0.1 | −0.5 | 0.8 | −13. | 35 | −26 | −3.1 | 0.6 | 0.9 | 0 | −0.1 | 0.1 | 0 | 0 | 0 |
| ... | 0 | 0 | −0.1 | −0.1 | −0.8 | 1.6 | −21. | 53.1 | −49 | −1.6 | 1.1 | −0.1 | 0.2 | 0 | 0 | 0 | 0 |
| ... | 0 | 0 | 0 | −0.1 | −0.1 | −0.8 | 2.1 | −23. | 16.5 | 12.6 | −0.8 | 0.5 | 0.1 | 0.1 | 0 | 0 | 0 |
| ... | 0 | 0 | 0 | 0 | 0 | 0 | −0.2 | 0.4 | 5.6 | 14 | −5.8 | 0.4 | −0.2 | 0 | 0 | 0 | 0 |
| ... | 0 | 0 | 0 | 0 | −0.1 | −0.1 | 0.4 | 0.5 | 1.8 | −13. | 19.2 | −7.5 | 0.4 | −0.3 | −0.1 | 0 | 0 |
| ... | 0 | 0 | 0 | −0.1 | −0.1 | 0.3 | 0.1 | 0.1 | 1.4 | −0.7 | −9.5 | 16.2 | −6.5 | 0.3 | −0.3 | −0.1 | 0 |
| ... | 0 | 0 | −0.1 | −0.2 | 0.3 | −0.1 | −0.1 | 0.1 | 0.6 | −0.8 | −0.2 | −7.2 | 13.6 | −5.6 | 0.2 | −0.2 | 0 |
| ... | −0.1 | −0.2 | −0.3 | 0.3 | −0.2 | −0.2 | −0.1 | −0.1 | −0.1 | −0.1 | −0.4 | 0 | −5.8 | 11.8 | −4.9 | 0.1 | −0.1 |
| ... | −0.1 | −0.4 | 0.6 | −0.2 | −0.1 | 0 | 0 | 0 | 0.1 | −0.2 | −0.2 | −0.4 | 0 | −5 | 10.6 | −4.6 | −0.1 |
| ... | −3 | 0.1 | −1.2 | −1 | −1 | −1.3 | −1.7 | −2.9 | −6.2 | 2.8 | 1.6 | 1.1 | 0.7 | 0.9 | −3.6 | 11.1 | −3 |
| N | 9 | −0.6 | 0.7 | 0.7 | 0.9 | 1.1 | 1.6 | 2.8 | 6.3 | −3.1 | −1.9 | −1.5 | −1.3 | −1.4 | −1.3 | −5.2 | 9 |

FIGURE 7.3: Typical matrix of velocity response to displacement thickness.

and global interaction laws is in the use of influence coefficients $d_{ij}$. In case of local linear interaction law, the diagonal member of interaction coefficient matrix $d_{ii}$ is used instead of Veldman's coefficient $4/(\pi\Delta\xi c_\infty)$:

$$u_{e\,i,NEW} = u_{e\,i,OLD} + d_{ii}(\delta^*{}_{i,NEW} - \delta^*{}_{i,OLD}). \tag{7.35}$$

In the case of global linear interaction law, the downstream stations edge velocity values are updated using $d_{ij}$ coefficients as the solution marches downstream. There is no point of updating the upstream stations, since the computation marches only in one direction. When global interaction law is employed, a jump in the displacement thickness influences the edge velocity at the node itself and at all downstream nodes from the jump position. In local interaction law, only the velocity at node itself is influenced by a velocity jump. Neither interaction law converges in as few steps as a fully simultaneous method, but the new interaction methods have a faster convergence rate than most basic Veldman's interaction law and converge also in some cases where Veldman's method fails. The results of using the global interaction law are not significantly better than using the local interaction law [A 5], so the local linear interaction law (LLIL) was used in the coupling of 2D boundary layer to 2D airfoil in this work.

#### 7.2.1.3 Fast way of computing linear interaction coefficient

It was found that the linear interaction law coefficient $d_{ii}$ can be computed without the need of additional inviscid flow calculations simply from the velocity field of the original body in an inviscid flow. This procedure takes equal computational time as Veldman's interaction law (it is negligible, compared to numerical differentiation). The difference

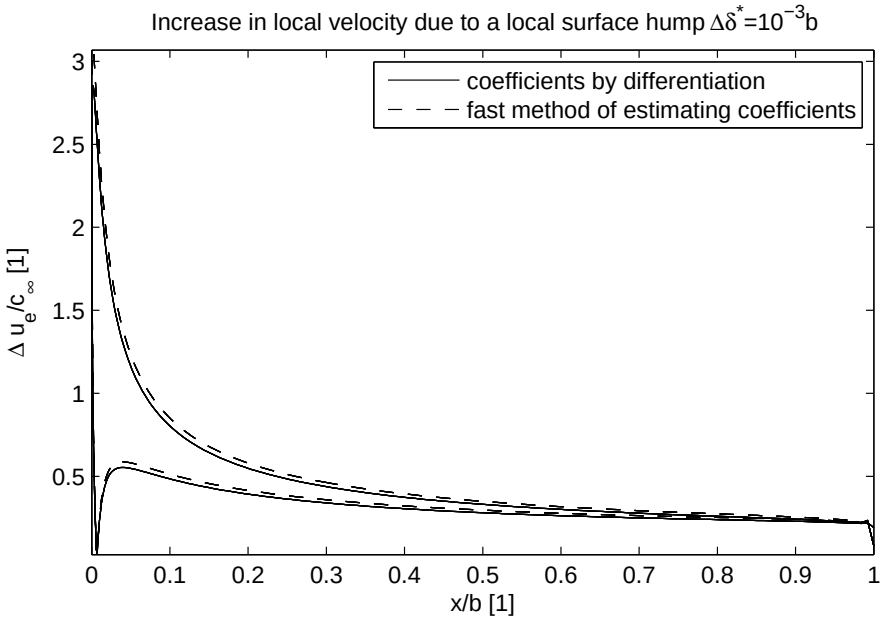


FIGURE 7.4: Influence of a local jump in displacement thickness on the surface velocity at the position of the jump, NACA 0012, $\alpha = 5°$.

between computing $d_{ii}$ by numerical differentiation and by the proposed fast method is in Fig. 7.4. The formula is presented in Eq. (7.36):

$$d_{ii} = \frac{2u_{e\ i,inv}}{(\xi_i - \xi_{i-1})}. \tag{7.36}$$

## 7.3 Application of boundary layer model to a 2D airfoil

The boundary layer model is first verified on a 2D airfoil. (Note: flat plate boundary layer verification of the presented method is given in [A 5]) For this purpose a simple 2D panel method is created using linear vortex distribution panels and stream function formulation. The results of an upper skin boundary layer on a NACA0012 airfoil under positive angle of attack $\alpha = 5°$ are compared against XFOIL results. Moderate Reynolds number 500 000 was used for the comparison. The method was tested and gives good results for the ranges of Re between $10^5$ and $3 \cdot 10^6$ although cases outside this range can be calculated as well with caution. Since the two models (boundary layer model developed in this thesis and XFOIL boundary layer model) use the same integral equations, the differences between the results are caused partly by a different numerical scheme and mainly by the way of coupling of the inviscid region to the boundary layer.

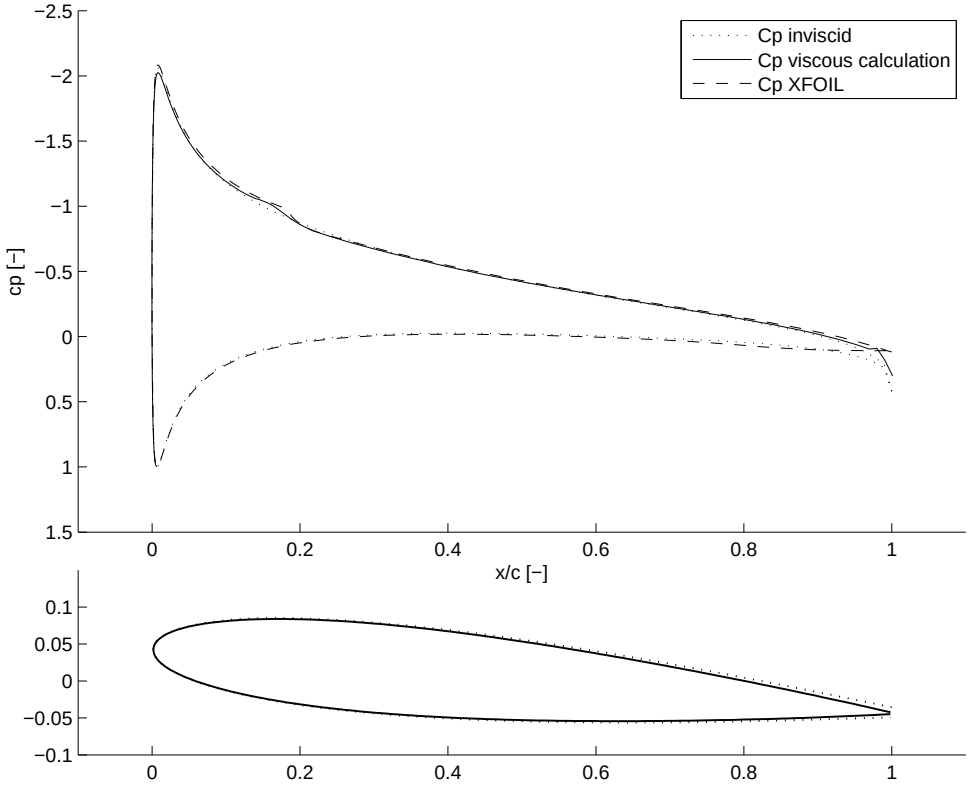


FIGURE 7.5: Pressure coefficient of a NACA 0012 airfoil, $\alpha = 5°$, Re = 500 000.

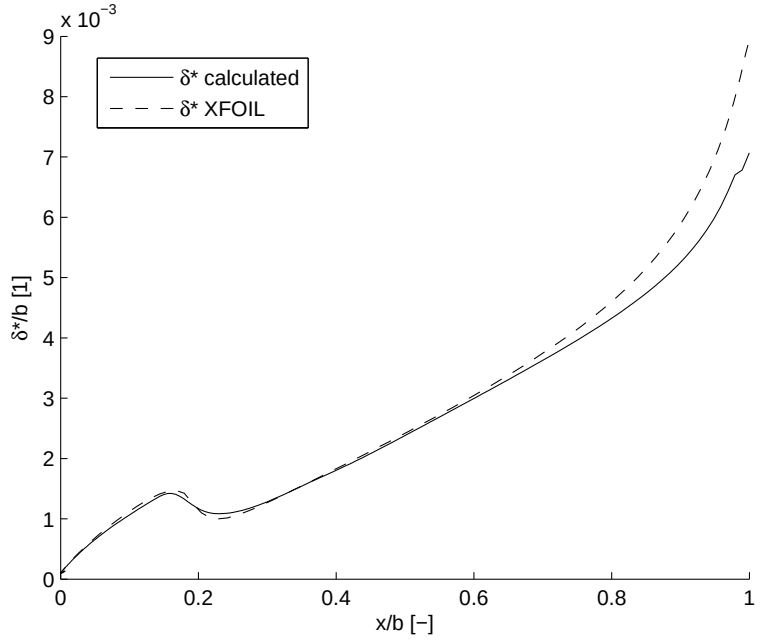


FIGURE 7.6: Displacement thickness comparison.

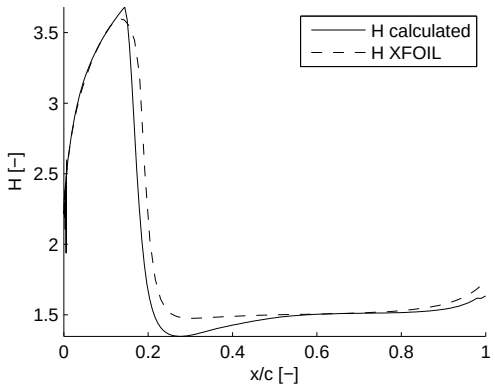


FIGURE 7.7: Shape factor comparison.

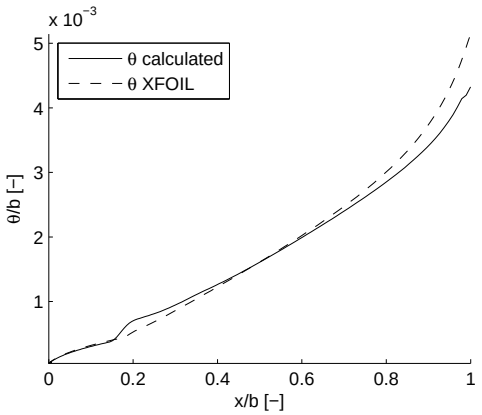


FIGURE 7.8: Momentum thickness comparison.

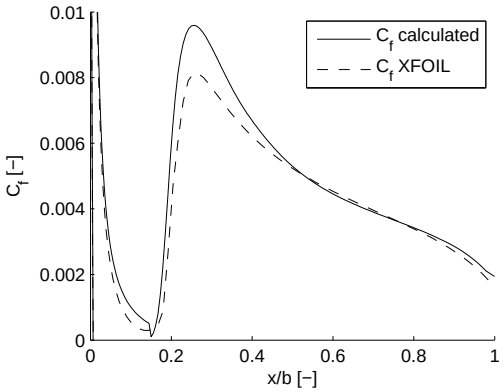


FIGURE 7.9: Skin friction cefficient comparison.

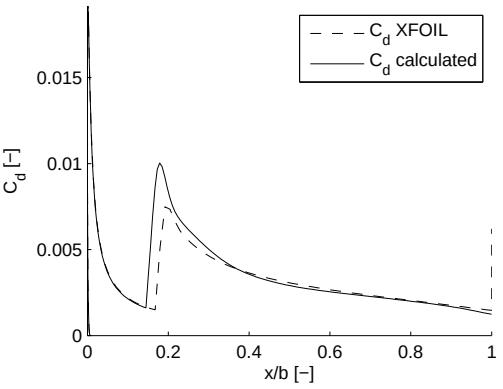


FIGURE 7.10: Drag coefficient comparison.

## 7.4 Calculating viscous drag from BL properties

Unlike the friction drag, which can be easily obtained from wall shear stress and surface integration, pressure (form) drag is a result of dissipation both in the boundary layer and in the wake. It is possible to evaluate the overall viscous drag either in a sufficient distance from the airfoil (far-field formulas), which is a more precise method, or approximate the dissipation in the wake using some of the available near-field methods, such as Squire-Young formula or Eppler method [61]. The far field viscous drag can be computed from the developed momentum thickness of the wake $\theta_\infty$ far downstream [61]:

$$F_{Dvisc} = \rho\theta_\infty c_\infty^2. \tag{7.37}$$

To avoid computing wake layer, Squire-Young formula is used, which extrapolates the behavior far downstream based on the state of boundary layer just behind the trailing edge.

$$F_{Dvisc} = \rho\theta_{T.E.}\left(\frac{c_{T.E.}}{c_\infty}\right)^{0.5(5+H_{T.E.})} c_\infty^2, \tag{7.38}$$

where $c_{T.E.}$ is the inviscid velocity just behind the trailing edge (the edge velocity at trailing edge will be used) and $H_{T.E.}$ is the shape factor at the trailing edge. The total viscous drag is calculated as the sum of upper and lower boundary layer contributions.

## 7.5 Interaction between 3D body and 2D boundary layers

Interaction between viscous boundary layer and inviscid panel method solution is the key element of the presented numerical method. The coupling process is described in detail in the following sections:

### 7.5.1 Obtaining boundary layer input data

First procedure of connecting a 2D boundary layer to a 3D body in inviscid flow is to compute the streamlines on the surface of the body. Each streamline should begin at a stagnation point and there should be equal number of streamlines on the suction and pressure sides of the wing. Also, there should be a reasonable number of streamlines along the span to enable surface interpolation of skin friction.

The algorithm for computing streamlines first interpolates the surface velocity of $M \times N$ panels to a finer mesh using cubic interpolation. This is done for two reasons. First reason is that stagnation point is found more precisely as the minimum of the refined surface velocity distribution at a specified span section. Second reason is the fact that 3D panel method uses only between 20-80 panels to discretize an airfoil section. With 80 panels streamwise and 40 panels spanwise, the total number of panels is 3200 already without wake, which gives $3200^2$ influence coefficients. In most practical cases, the contra-rotating propeller blade will be discretized by 40 panels streamwise and 20 spanwise. For boundary layer to converge reliably, between 100-150 conveniently distributed stations are required. This is achieved by surface velocity refinement using cubic interpolation. Example of such streamlines is in Fig. 7.11, where an elliptic oscillating wing under constant side slip angle 10° is captured at the point of maximum positive angle of attack $\alpha = 15°$, and Fig. 7.12 shows streamlines of a loaded propeller blade.

After the streamlines are found, the cumulative sum of lengths of the segments of each streamline will provide B.L. coordinate $\xi$. Edge velocity $u_e$ is simply the interpolated

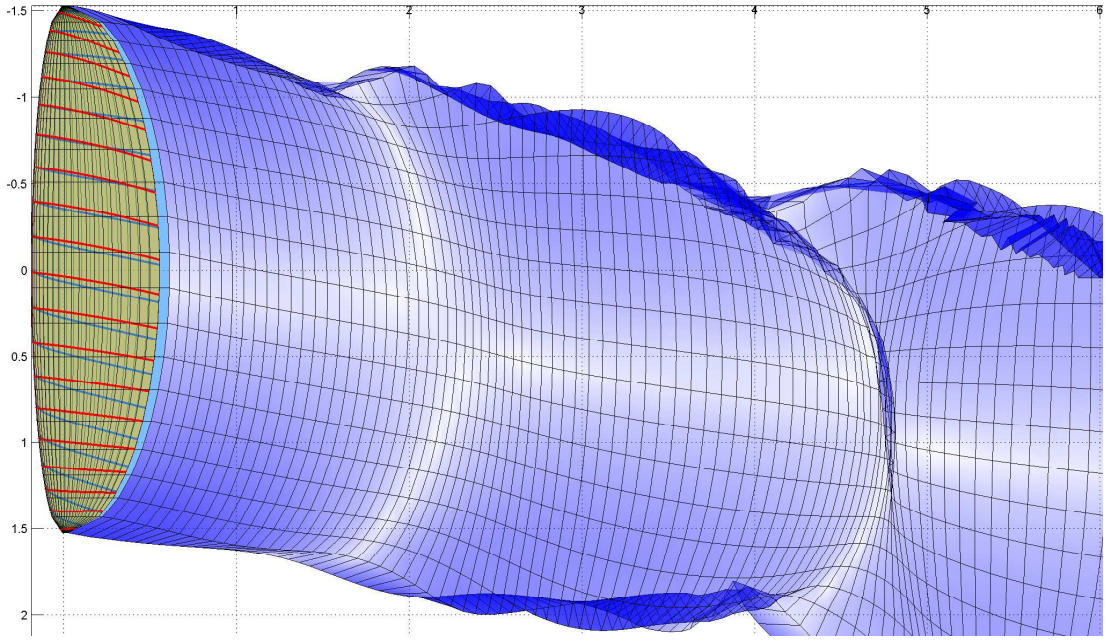


FIGURE 7.11: Instant streamlines on the surface of an elliptic oscillating and side-slipping wing. Red: top surface streamlines. Blue: bottom surface streamlines.

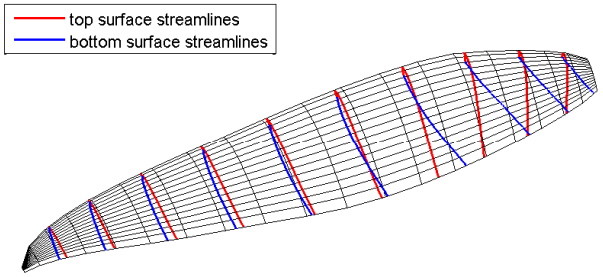


FIGURE 7.12: Surface streamlines of a heavily loaded propeller blade.

surface velocity at each point of the streamline. Interaction coefficients are calculated according to Eq. (7.36).

### 7.5.2 Handling stall conditions

In the present numerical scheme, boundary layer separation is detected by either boundary layer solver divergence, or reaching of a predefined shape parameter value. In general, calculating results for angles of attack beyond maximum lift is neither providing realistic values, nor it is deemed necessary. In some cases, however, the blade or wing stalls only in a very limited section of the span. In these cases, the position of separation along the streamline is marked as separation point and boundary layer thickness and shape factor are grown from this point downstream artificially by user defined gradients. The information about the number of separated span stations and downstream position of

separation is available as an output. Results with presence of large separated regions should be approached with caution.

### 7.5.3 Coupling of the boundary layer

The local linear interaction coefficient $d_{ii}$ only estimates the local response of edge velocity to a local change of displacement thickness. Further boundary layer passes, with inviscid flow solution updates in-between, are necessary to arrive at a converged solution. Even with an accurate linear interaction coefficient, between 10 and 20 passes are required for converged solution. This is a known problem of quasi-simultaneous viscous-inviscid interaction methods [60].

Repeatedly calculating inviscid solution between passes can be easily performed with a two-dimensional panel method but this approach would be too time consuming with three dimensional panel method with sufficient panel density.

A completely different solution approach was developed for boundary layer coupling to a 3D panel method. To make the boundary layer model easily portable, a replacement inviscid model is proposed, which allows to approximate the edge velocity based on initial surface velocity distribution and displacement thickness alone.

#### 7.5.3.1 Replacement inviscid model

Each column of the response matrix $d_{ij}$ contains information about the response of edge velocity to a single node displacement. One such response is demonstrated in Fig. 7.2. As can be seen, neighboring nodes of the node $j$ with surface jump $\Delta\delta^*_j$ are subject to drop in edge velocity of about half the magnitude of the velocity growth at $j$-th node. This can be also observed by comparing the values of subdiagonal and superdiagonal with main diagonal of the response matrix.

Based on these observations, new replacement inviscid model has been formulated, which can be used for boundary edge velocity updates between boundary layer passes:

$$u_{ei} = u_{ei,orig} + d_{ii}(\delta^*{}_i - 0.5\delta^*{}_{i-1} - 0.5\delta^*{}_{i+1}). \tag{7.39}$$

Although the replacement inviscid model does not account for global effects of boundary layer thickening, such as shifting of the stagnation point, its estimation of edge velocity behavior is sufficient to produce a boundary layer solution surprisingly similar to the XFOIL results. When the replacement inviscid model is used together with the boundary

layer model, the only input parameters needed are the velocity distribution with surface coordinates. This makes the resulting boundary layer truly portable with small impact on results accuracy.

### 7.5.4 Drag evaluation from Trefftz plane

The Trefftz plane analysis is based on the concept of a fictional bounding box, with edges aligned with free stream velocity, which contains a finite wing. If the box is made large enough, the influence of the wing on the velocities on the box surfaces approaches zero, except the rear face, through which the wake passes. The rear face of the box is called Trefftz plane. Due to the large distance behind the wing, several assumptions can be made. First of all, the influence of bound vortex is neglected and the horseshoe vortices passing through the plane act as infinite vortex filaments. Moreover, due to the sufficient distance, the force-free vortex wake sheet is already aligned with the flow and therefore it is perpendicular to the Trefftz plane.

Induced drag, as a byproduct of lift, can be calculated from the change of kinetic energy between front face of the bounding box and rear face (Trefftz plane) [16]:

$$F_{Di} = -\frac{\rho}{2} \int \int (c_y^2 + c_z^2) dy dz. \tag{7.40}$$

The remaining components of drag connected to viscosity (friction drag and pressure (form) drag) can be expressed by a single viscous drag formula for incompressible flow [62]:

$$F_{Dvisc} = \int \int \Delta p_0 dy dz. \tag{7.41}$$

The above equations are used directly for evaluating CFD results used for validation (Appendix B).

Different process based on Trefftz plane theory is used for presented panel method and lifting line wake. Following the steps described in [16], formula for induced drag can be derived as:

$$F_{Di} = -\frac{\rho}{2} \int_{-L/2}^{L/2} \Gamma(z) c_z dz. \tag{7.42}$$

Where $L$ is the local wake span, $z$ is spanwise coordinate, $\Gamma(z)$ is local circulation strength and $c_z$ is the local induced downwash. The coordinates must be aligned with

free stream velocity, so that in sufficient distance from wing, wake filaments are parallel to $x$ axis, and perpendicular to the $y - z$ plane (Trefftz plane).

## 7.6 Comparison of numerical methods on the case of finite wing

In order to evaluate the performance of the 3D panel method coupled with boundary layer solver, this new combined model was compared against lifting line model computation and three-dimensional CFD calculation of a finite wing using commercial package Ansys FLUENT. Details of the comparison are described in [A 6]. Information about CFD calculation are contained in appendix B, since they do not directly relate to the main topic of this thesis. The lifting line model results rely on precise airfoil polars, which are in this case computed using XFOIL.

As a model case, an elliptic wing with root chord 2.5m, wing span 10m and NACA 4415 airfoil was generated and analyzed. This resulted in a wing with low aspect ratio 5.11 and M.A.C 1.96m. To fit into the low Reynolds number and low Mach number region of interest, free stream velocity was set to 5m/s, which results in quite low Reynolds number $6 \cdot 10^5$ and Mach number $Ma = 0.015$. With these conditions, compressibility is negligible and boundary layer is relatively thick with considerable laminar portion, which is suitable for showing the differences between the models.

Drag evaluation from Trefftz plane was used to obtain the total and induced drag coefficients. The k-$\omega$ SST Transitional turbulence model was chosen for representing CFD results. The result in terms of drag and lift coefficients are shown in Figures 7.13, 7.14 and 7.15. To demonstrate the issue of drag evaluation from force integration over the wing's surface, the total drag from force integration is shown as well.

Concerning lift vs. angle of attack, CFD results indicate lower lift slope angle, while LL method and 3D panel method produced almost identical results. CFD predicts negative angle of attack stall quite early, at approximately $\alpha = -10°$, unlike LL and 3D panel method which indicate attached flow even at $\alpha = -15°$. Positive angle of attack stall is predicted by all methods at approximately $\alpha = -17°$. CFD predicts sharp stall, LL method predicts smooth and gradual loss of lift. The lift results of 3D panel method with boundary layer contain a small jump at $\alpha = 7°$ from which the lift slope angle changes. The lift curve continues rising until it reaches its maximum at $\alpha = 13°$. This can be explained by trailing edge separation beginning and progressing to a fully separated flow. The lift prediction around the angle of attack, where the trailing edge boundary layer separation begins still show that some improvements to the model could be made.

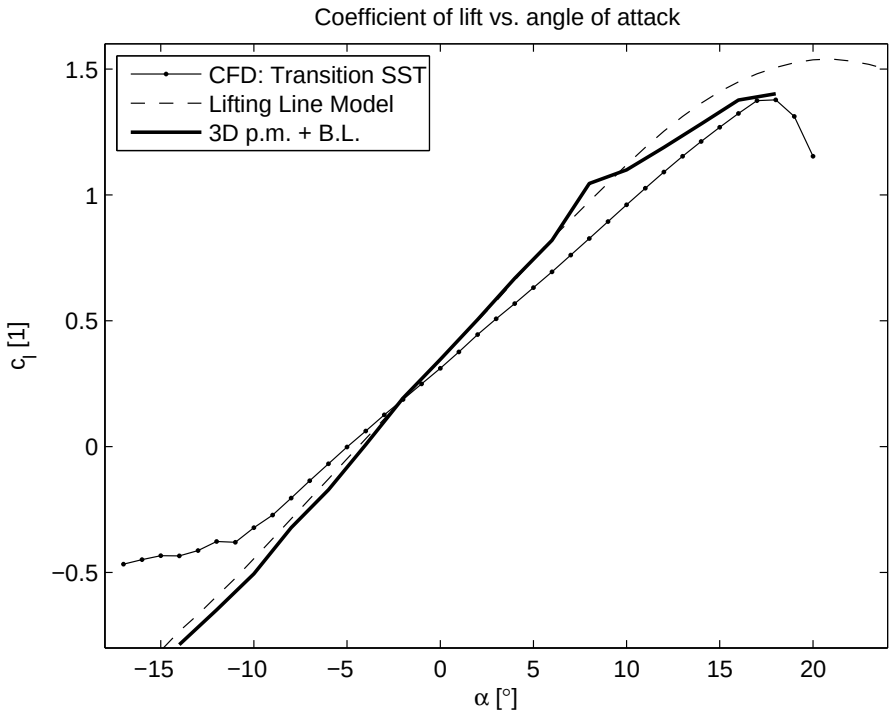


FIGURE 7.13: Coefficient of lift vs. angle of attack, elliptic wing.

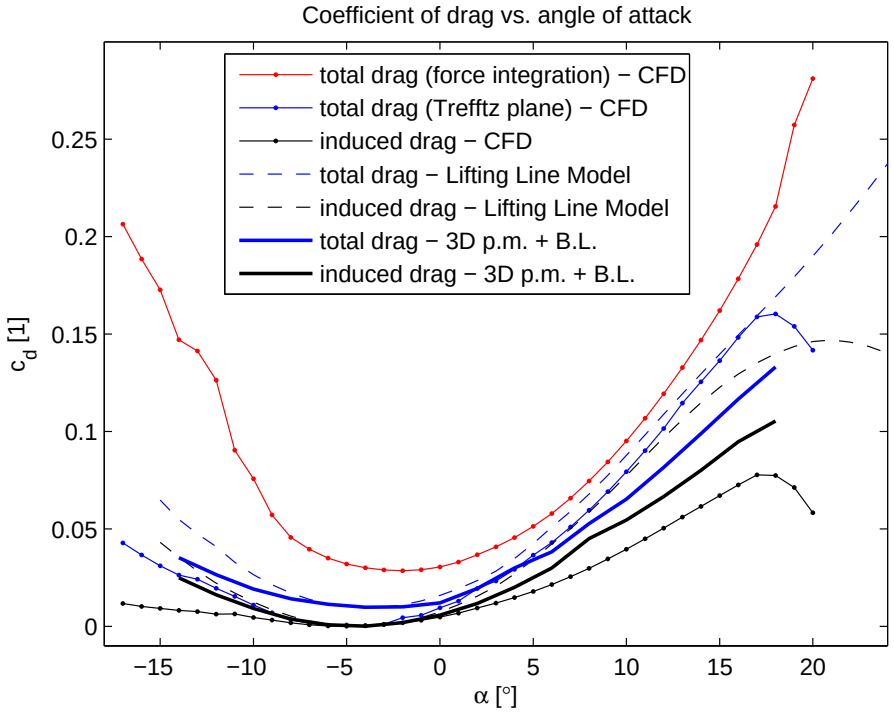


FIGURE 7.14: Coefficient of drag vs. angle of attack, elliptic wing.

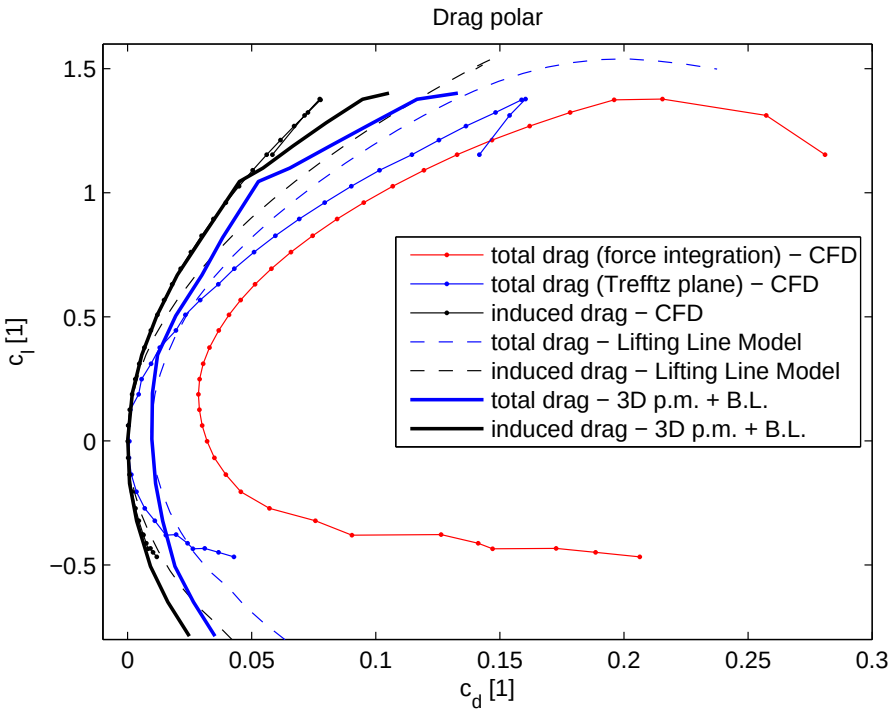


FIGURE 7.15: Drag polar, elliptic wing.

The drag results in Figure 7.14 confirm, that drag prediction is in general more problematic than lift prediction. Even when total drag by CFD force integration is disregarded, the results still differ noticeably. Induced drag evaluated in the Trefftz plane by CFD software package is rather low compared to the other computational methods which suggests numerical dissipation could be the issue here. The difference between drag calculated by lifting line method and 3D panel method with boundary layer falls under 20%.

# Chapter 8

# Experimental Investigation of Contra-Rotating Propellers

## 8.1 Measurement setup

The experiment described on the following pages together with data from initial measurement is described in detail in a conference paper [A 7] by the author et al. Experimental setup has been built with the assistence of Ing. Martin Brada and departmental technicians. The goal of the experiment is to provide accurate and detailed aerodynamic data for a set of contra-rotating propellers. The propellers should rotate in a free space with few obstructions that would interfere with the flow. The rotational rate (rpm) of each propeller must be controlled independently and accurately. This leaves a pair of electric motors the only option as the power plants.

First important decision is the selection of scale of the experiment. Reynolds numbers (with respect to chord length) well above 100 000 should be reached. This condition is met in case of propellers with diameter 0.508 m (20") and larger for which large selection of both electric motors and propellers themselves exist. The chord length of a 20" diameter propeller at $0.7R$ is typically between 0.03 and 0.04 m and using typical rotational speed of 6000-8000 rpm, the Reynolds numbers with respect to chord length fall in range between 200 000 and 400 000. Another global parameter is the arrangement of the drive units. There are three possible configurations, shown in Fig. 8.1.

In all three configurations, supporting structure is obtrusive but unavoidable. Configuration No. 2 has no real advantages, flow is disturbed by the supporting structure and propeller distance is too large. Configurations No. 1 and 3. have both adjustable propeller distances. Configuration No. 1 was selected, because at the price of higher

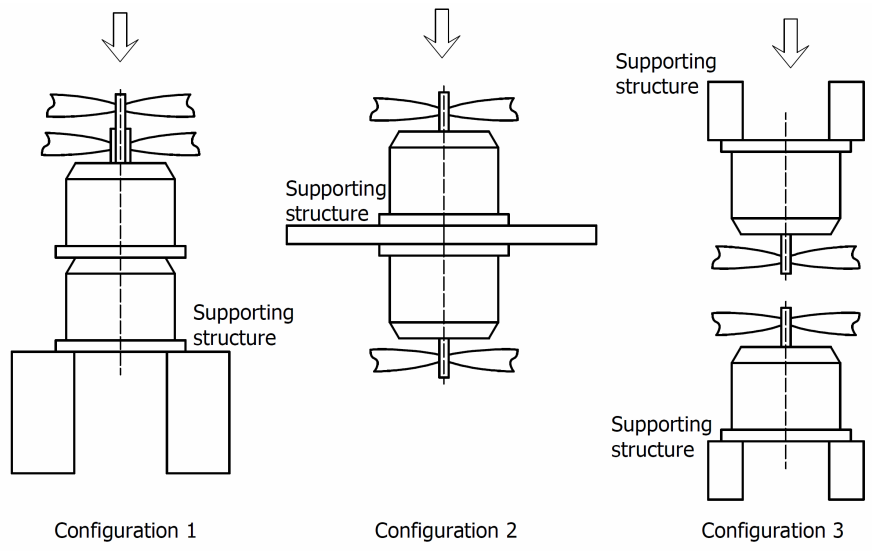


FIGURE 8.1: Possible configurations of contra-rotating coaxial propeller drive, also appeared in [A 7].

mechanical complexity of coaxial shafts, it features clear inlet path, which is beneficial for comparison with numerical results.

## 8.2 Description of the test stand

The mechanical design of aerodynamic balances acting as a motor mount takes advantage of standard Zemic L6D type load cells. Double Axi 5330/20 coaxial motors connected to 24V lead acid battery with up to 6kW of input power were used. The two motors were decoupled and rejoined with a coupling member containing bearing. This member can carry only axial loads, no torque is transferred. The upstream motor, which powers second (downstream) propeller is attached to a thrust and torque measuring three-armed motor mount. Because the downstream propeller is axially disconnected from the shaft, the motor mount measures only thrust from the upstream propeller and torque from the downstream propeller. The thrust force from the downstream propeller is carried via pullrods to single a load cell. Similarly, the torque from the upstream propeller is measured by a single load cell. Figure 8.2 shows the setup of electric motors with aerodynamic balances. Photos (Fig. 8.3, 8.4) show the actual realization of the design. For safety reasons, the test stand is equipped with a protection wire mesh to catch possible debris in case of mechanical or structural failure of propellers or shaft assembly. The mechanical design of the test stand allows limited modification of propeller distance in the range of 40 mm to 80 mm.

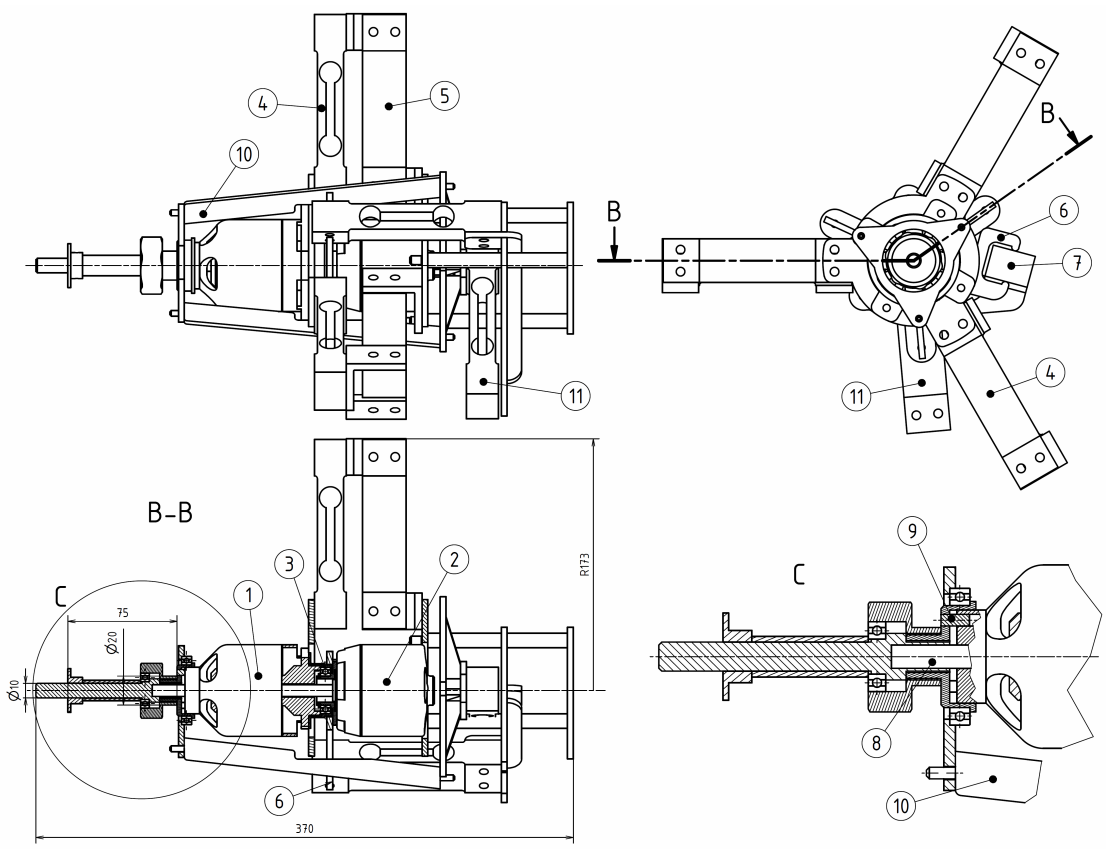


FIGURE 8.2: The coaxial motor power unit including force measuring motor mount, also appeared in [A 7]

1 Upwind electric motor
2 Downwind electric motor
3 Coupling member with bearing
4 Motor mount thrust measuring load cell
5 Motor mount torque measuring load cell
6 Arm connected to downstream motor
7 Dedicated load cell for torque of downstream motor
8 Inner shaft of downstream motor
9 Torque carrying pins
10 Pullrods
11 Load cell for thrust measurement of downstream propeller

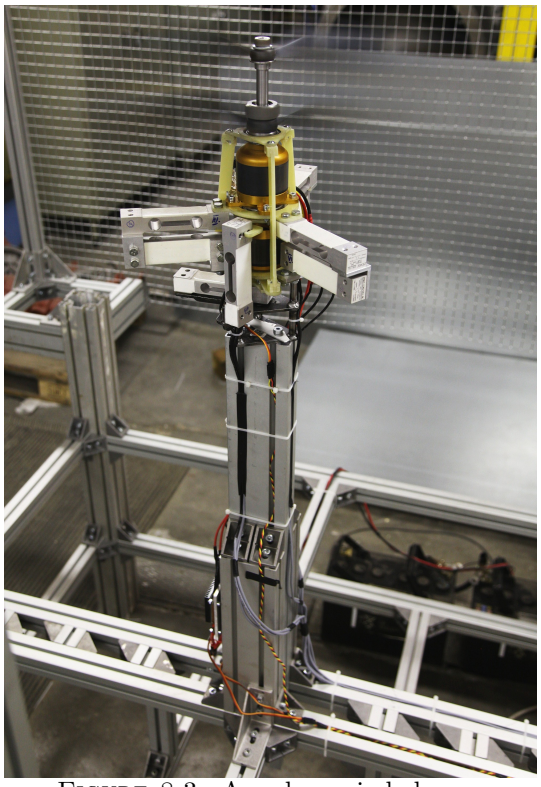

FIGURE 8.3: Aerodynamic balances mounted on a rigid support column.

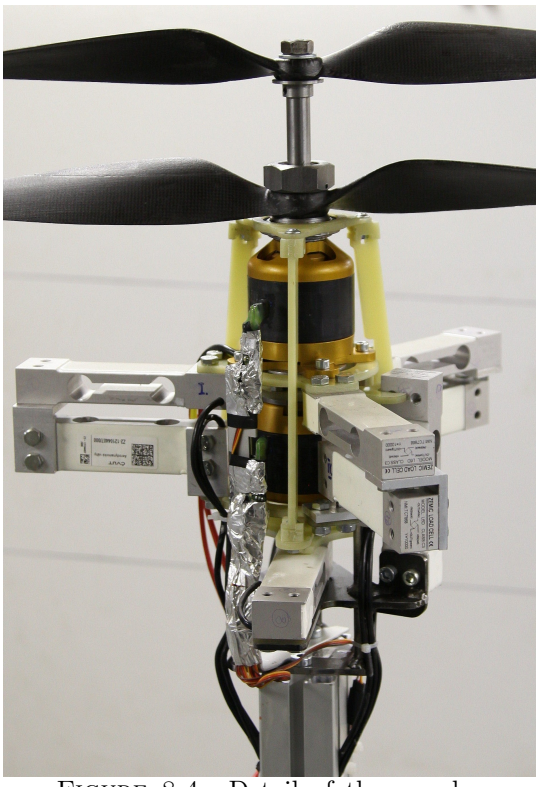

FIGURE 8.4: Detail of the aerodynamic balances.

## 8.3 Measured quantities and user control

The signals from the bridges of all 8 load cells are converted to digital signal by an A/D converter with $2 \times 6$ channels designed for this purpose (Fig.8.5). The A/D converter samples the signal at a high rate and sends the averaged results to PC. Every load cell is calibrated separately to obtain a unique sensitivity constant for each load cell. After the balances are assembled, the thrust of the upstream propeller and forces due to torque of the downstream propeller (both measured by three load cells), are calculated as a sum of contributions from each load cell. The forces are converted to torques through a secondary calibration process. Zero force reading is performed before each run. From the measured signal, zero readings and calibration constants, torque $Q_1, Q_2$ and thrust $T_1, T_2$ of each propeller are obtained. Index 1 belongs to the upstream propeller and index 2 to the downstream one.

An infra-red LED diode and photodiode pair measures the rotational speed of each motor. Room temperature, atmospheric pressure and relative humidity are measured before each set of measurements to determine air density.

A supplementary measurement of noise in terms of overall sound pressure level and sound spectra is performed. Its purpose is to provide some useful insight into the problematic aspect of CRP application: excessive noise generation. Details of noise measurement

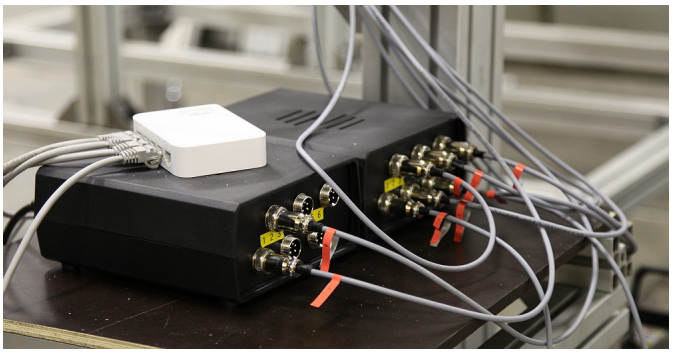

FIGURE 8.5: Custom made A/D converter for load cell signal.

setup are in [A 7] and [A 1]. NTI XL2 audio analyzer with M2211 Class 1 measurement microphone was used for the noise data acquisition.

The electric motors are controlled via speed controllers using PWM signal. The PWM signal is generated by a 4 channel PWM generator connected to a computer workstation. A set of MATLAB scripts with interactive GUI has been prepared for the purpose of measurement control and data acquisition. The user specifies a sequence of PWM signals for each motor and duration of each measurement step. The whole measurement process is automatic, with the exception of acoustic measurements, which must be done manually during each measurement step.

## 8.4 Measured propellers

Several propeller sets were originally planed to be analyzed, but due to some issues only one CRP set was analyzed. This is due to the fact that manufacture of carbon fiber blades according to provided CAD data is quite expensive and there are only few commercially available CRP propeller sets that unfortunatelly do no fit the mount of the test stand. Moreover, no precise geometry data are available for off-the-shelf products.

### 8.4.1 Aero-elastic properties of small scale propellers

Aero-elastic properties of small scale aircraft propellers were obtained by analyzing the shape of the rotating blades photographed by a camera and a flash synchronized to the blade position. Detailed description and results can be found in [A 1]. The research revealed that bending of the blades forward occurs with increasing thrust. This bending is reduced by centrifugal forces, which prevents the blades from bending even further under higher rpms. Light and rigid carbon blades bended in a similar fashion as heavy but flexible fiber reinforced plastic blades due to centrifugal forces. Twist was

determined from a side view and top view photo. Image analysis did not reveal any significant twisting of the loaded blades, which would have an effect on the performance. This confirms the assumption, that for the size and material of propellers used in the experimental investigation, blades can be treated as rigid.

### 8.4.2 Propeller set PS1

The set of propellers that is being analyzed both numerically and experimentally is a pair of almost identical 22" ($D = 558.8mm$) propellers. The difference between the two propellers is of course their orientation (left and right handed) and pitch. The upstream propeller has pitch designation 18" ($457.2mm$), whereas the downstream propeller has nominal pitch 20" (508 mm). Other parameters, such as chord length distribution, airfoil geometry and pitch distribution shape, are the same. Precise surface geometry data used for mold manufacture are available. This is important for verification of computational models of the propellers. An important factor that must be considered when interpreting the results is the fact that the propellers were designed for a positive (non-zero) advance ratio, but they are being tested at static thrust conditions.

FIGURE 8.6: Measured propeller set PS1, top view.

FIGURE 8.7: Measured propeller set PS1, side view.

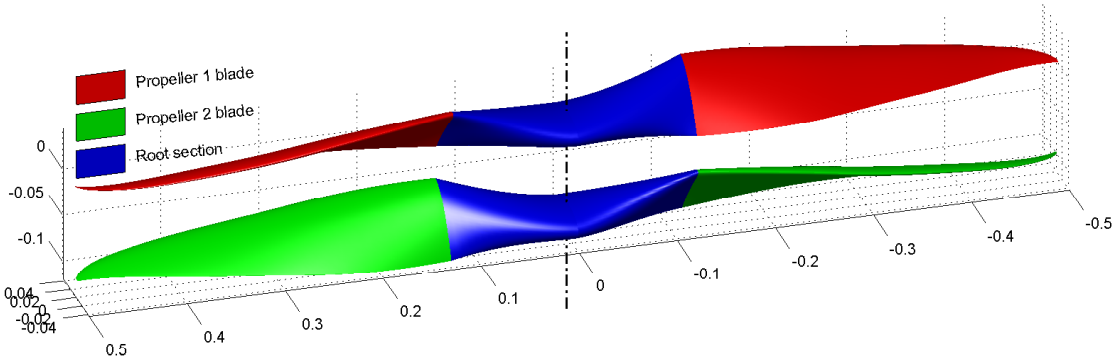


FIGURE 8.8: Measured propeller set PS1, geometry imported to MATLAB.

# Chapter 9

# Results, Analysis and Discussion

The numerical methods are tested on cases of single and contra-rotating propellers for which experimental data are available. This establishes the level of accuracy to be expected from the computational methods. Experimental and numerical results of single propeller with variable advance ratio, CRP with variable rotational rate ratio, and CRP with variable propeller distance are presented. These results are also published in [A 8]. The difference between CRP and equivalent single propeller is explored numerically. Experimental results of contra-rotating propellers are supplemented with results of noise measurement where applicable. Noise measurement results do not serve for numerical model verification but complete the experimental investigation of CRP systems.

Each section describes one investigated case and contains subsection describing results of 3D panel method and lifting line method both compared to experiment where available. When all experimental results are exhausted, purely numerical studies are carried out to explore various properties of CRP systems.

3D panel method with boundary layer model consists of a force-free wake described in Chapter 5 connected to a blade represented by a 3D panel body (Chapter 6) with boundary layer (Chapter 7). Results with boundary layer component switched off are also shown and described as “inviscid” in the legends.

Lifting line based model consists of a force-free wake described in Chapter 5 connected to a blade represented by a lifting line formed by bound vortex segments (Chapter 6). Polars calculated by XFOIL are used in the lifting line model.

## 9.1 Verification using single propeller wind tunnel results

Based on the results obtained during recent measurement of model propellers in a wind tunnel [A 9], data from the measurement of an APC $20 \times 13$ propeller were selected for verification of the numerical model in a single propeller test scenario. Note, that this measurement was obtained using different equipment from the one described in Chapter 8. Due to vibrations, the measured data from wind tunnel contained significant scatter of points, as can be seen from the error bars (Fig. 9.1), showing standard deviation of the measured data. Geometry of the propeller blades was scanned using manual contact scanner.

### 9.1.1 Results of 3D panel method with boundary layer

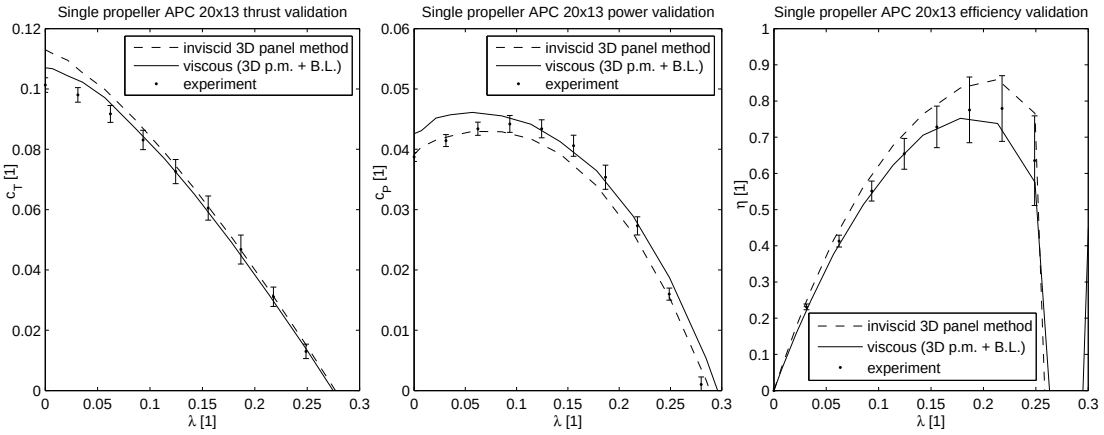


FIGURE 9.1: Comparison of numerical and experimental data to verify functionality in case of single propeller.

Both viscous and inviscid model results are shown in the comparison (Fig. 9.1). The inviscid results are shown for reference purposes and were calculated using the same model as viscous results, only with boundary layer model disabled. Coefficient of thrust is predicted well by the viscous model, except region near static thrust ($\lambda = 0$), where the numerical results of thrust are too optimistic. This is connected to more problematic coupling between panel method and boundary layer in conditions of separation, as was also seen in finite wing validation case. Separation onset and extent of separation is sensitive to various aspects of numerical modeling as well as experimental conditions such as surface roughness, level of turbulence or even background noise levels. Larger error is therefore to be expected for a nearly stalled blade.

Prediction of power corresponds well with experiment in the region of ($\lambda > 0.1$). Again for low advance ratios, the power is over-predicted, which is in correspondence to thrust

being slightly over-predicted. The fact that power calculated by inviscid model matches well the experiment near static thrust conditions is only a coincidence caused by the missing viscous power losses and induced power due to thrust overprediction canceling out each other. Efficiency calculated from experimental data is well matched by the numerical model.

### 9.1.2 Results of lifting line method

Single propeller APC $20 \times 13$ is again used for evaluating performance of the lifting line code. The calculated results using lifting line representation of the blades are shown in Fig. 9.2 together with experimental results and results of 3D panel method with boundary layer, which are discussed above.

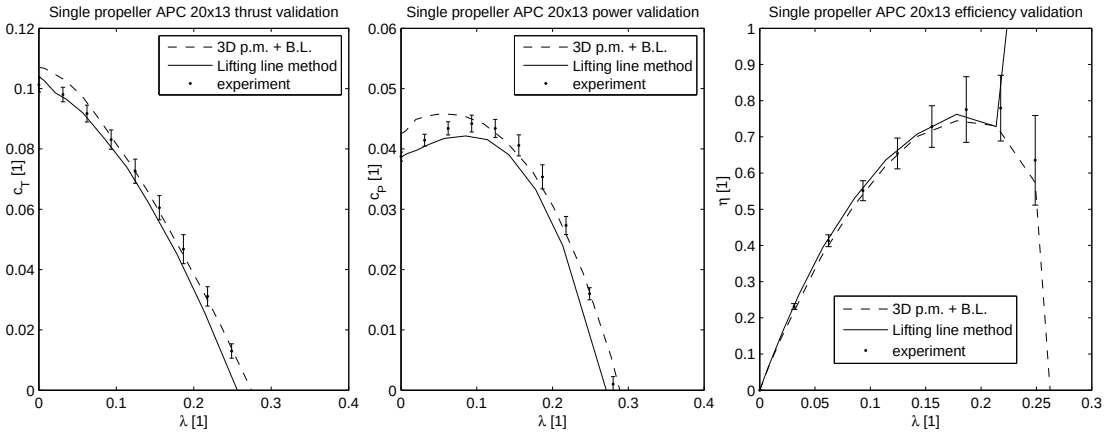


FIGURE 9.2: Comparison of lifting line model results with experiment and 3D panel method with boundary layer. Case of a single propeller APC $20 \times 13$.

Given a much lower complexity of the method, the lifting line method produces surprisingly accurate results. The prediction of performance near static conditions by lifting line is slightly better than that of 3D panel method with boundary layer probably due to more precise separation prediction provided by XFOIL polars used in the blade representation. On the other hand the lifting line method shows weaker agreement with experiment for all advance ratios above 0.1. The efficiency corresponds well with experiment for both methods, except erratic behavior of lifting line method near maximum advance ratios, which is due to high sensitivity of the efficiency expression to small errors near zero thrust regime.

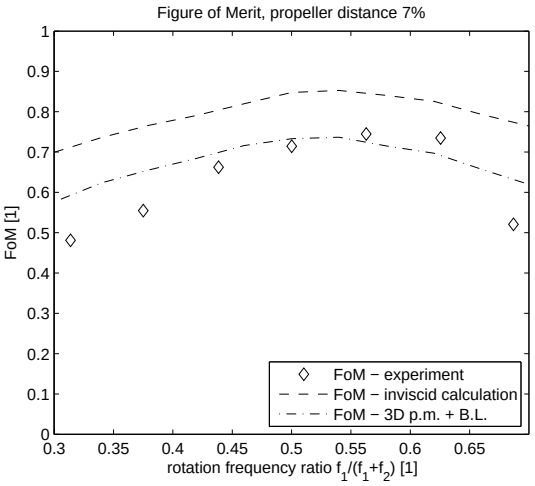


FIGURE 9.3: Figure of Merit vs. ratio of frequency of rotation.

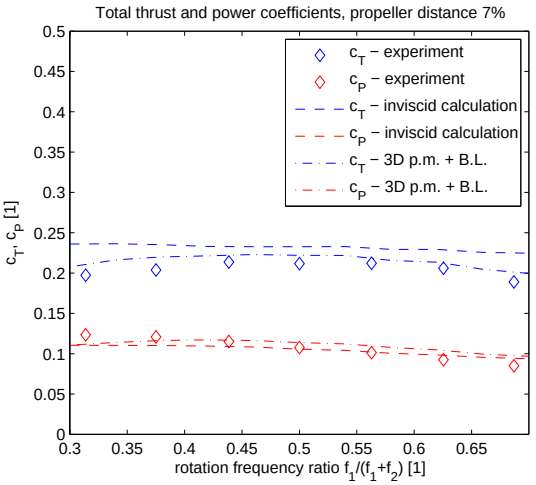


FIGURE 9.4: Total thrust and power coefficients of the system vs. ratio of frequency of rotation.

## 9.2 Contra-rotating propellers in static thrust regime

### 9.2.1 Case of variable rotational speed ratio

The experimental setup described in Chapter 8 allowed examining of CRP system under different rotational frequencies. The ratio of rotational frequencies is expressed as $f_1/(f_1 + f_2)$ and reaches 0 when only downstream propeller rotates, 0.5 when both propellers rotate at the same frequency ($f_1 = f_2$) and can reach up to 1, when only upstream propeller rotates. The experimentally investigated frequency ratio falls in the range $0.3 \div 0.7$.

#### 9.2.1.1 Results of 3D panel method with boundary layer

Figure 9.3 shows the Figure of Merit dependence on rotational ratio. The propeller distance in the experiment and calculations was set to 7% of propeller diameter.

Boundary layer component of the numerical model improves the solution considerably. Still, there is a notable overprediction of Figure of Merit for high and for low frequency ratios. This is due to the fact that both propellers have relatively high pitch, and are partially stalled (according to numerical results) even in case of equal rotational frequencies, where the load is shared evenly by the propellers. When one of the propellers rotates considerably faster than the other, it overtakes most of the loading and falls into deep stall. This explains the departure of numerical results from experimental data in conditions of extreme frequency ratios because the described computational method is not able to resolve separated flow accurately.

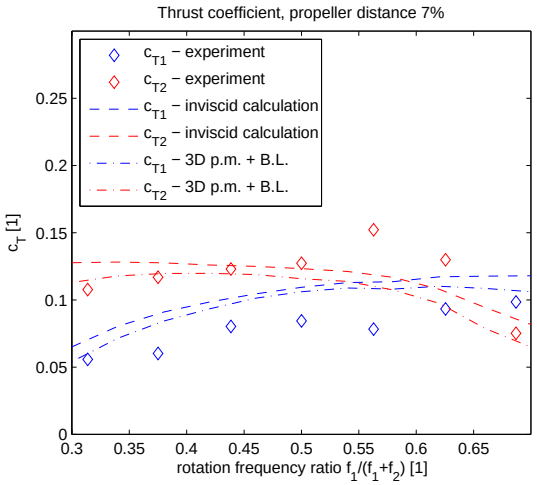


FIGURE 9.5: Individual thrust coefficients of each propeller vs. ratio of frequency of rotation.

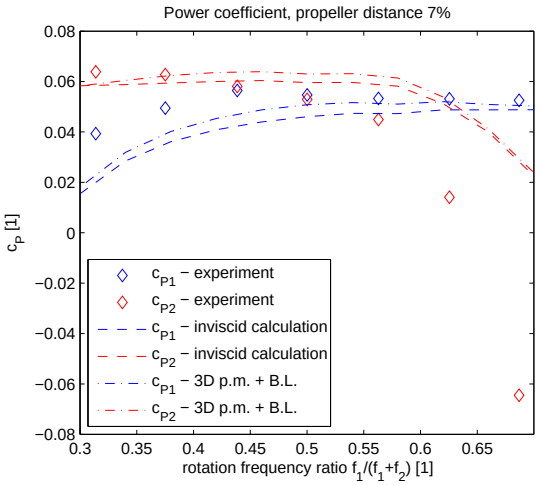


FIGURE 9.6: Individual power coefficients of each propeller vs. ratio of frequency of rotation.

The same phenomena described using Figure of Merit can be seen in diagrams of overall thrust and power coefficients in Fig. 9.4. Power coefficient is predicted well, whereas thrust coefficient is overpredicted by the numerical method.

The individual thrust and power coefficients of the propellers shown in Figures 9.5 and 9.6 reveal a less than ideal match. This may be due to some degree of thrust and torque sharing in the experiment between individual force measuring members due to relative axial and radial friction between coaxial shafts. The sum of thrust and sum of torque was not affected by this problem, however individual thrust and torque of each propeller measured during experiment is subject to some systematic error.

**Unsteady forces**

A typical plot of thrust and power over time is shown in Fig. 9.7. It has been calculated using PS1 geometry, with propellers 7%$D$ apart rotating at frequency 100 Hz in opposite direction under zero free stream velocity. Figure 9.8 shows the detail of first half of third rotation. To obtain better resolution, the time step was lowered for the detailed calculation.

During one period of rotation (10 ms), the upstream propeller shows gradual variations in thrust with peak-to-peak amplitude 13% of the mean value. Fluctuations in power of the upstream propeller are negligible. Both thrust and power of the downstream propeller are significantly influenced by the presence of wake of the first propeller with sharp jump of values during blade passage through wake. The amplitude of downstream propeller thrust fluctuation is 40% of mean value and in case of power the amplitude reaches 44% of mean value. Since rotational speed is constant, conclusions about power fluctuations are applicable to torque as well. The number of peaks in thrust and power (4) per rotation relates to the number of times the downstream blade passes through a

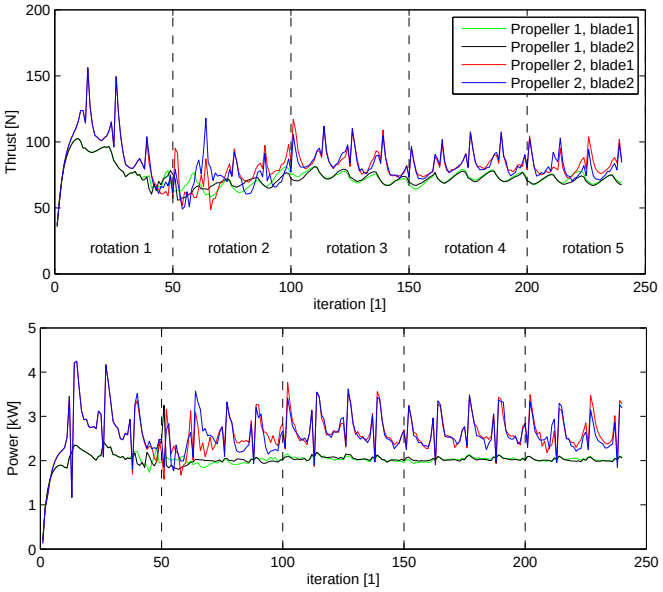


FIGURE 9.7: Unsteady values of thrust and power during initial 5 rotations.

wake sheet and also it corresponds to the number of times the upstream propeller blade comes to close proximity of the downstream propeller blade.

During first rotation, the wake is being formed and both blades of each propeller experience symmetrical loading. During second rotation, due to numerical stability reasons, the wake becomes asymmetric, loses its defined shape, which results in erratic thrust and power values. During third rotation, the behavior of the system stabilizes as the region of collapsed wake moves downstream under the self induced velocity. Rotation number 4 shows no significant changes and its results can be already used for thrust and power averaging and comparison against experimental results.

The frequency of largest amplitude of force oscillations corresponds to the frequency of downstream propeller passing upstream propeller wake. This occurs four times per rotation, given a same speed of rotation of both propellers. When the propellers are measured at rotation frequency $f = 50Hz$, observing the Nyquist criterion, sampling frequency in the experiment has to be $f_s > 400Hz$. During experiment described in Chapter 8, the samples were averaged in the A/D converter to a lower sampling rate, therefore no experimental data are available for comparison.

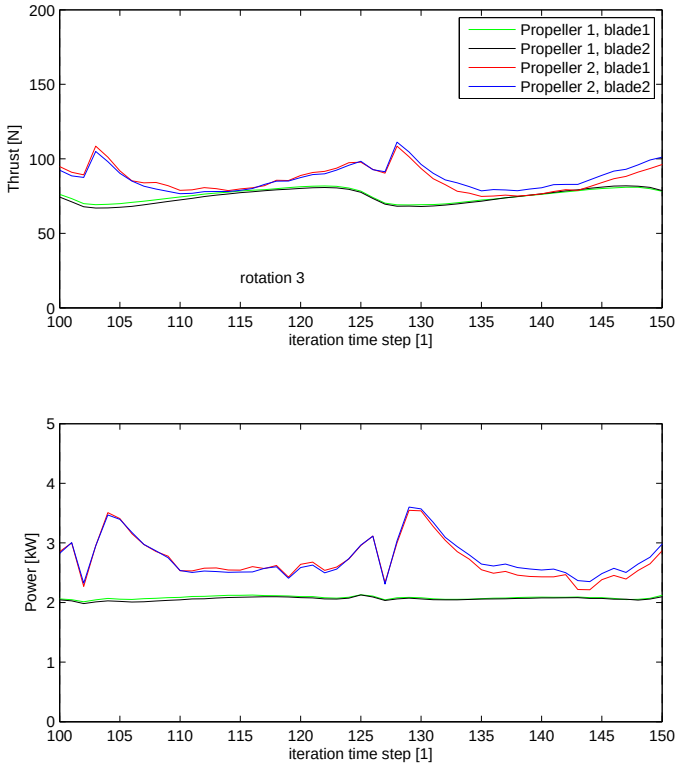


FIGURE 9.8: Unsteady values of thrust and power during one half of rotation.

#### 9.2.1.2 Results of lifting line method

The results of lifting line in terms of Figure of Merit and overall thrust and power coefficients are shown in Figs. 9.9 and 9.10. Although the lifting line model prediction corresponds well with experiment near 0.5 frequency ratio, as the ratio moves towards 0 or 1 the lifting line prediction shows a weaker fit with experiment than 3D panel method with boundary layer.

The same can be concluded about thrust and power coefficients of the individual propellers, where the trends and shape of the curves show better correspondence of 3D panel method results to the experiment than lifting line method results.

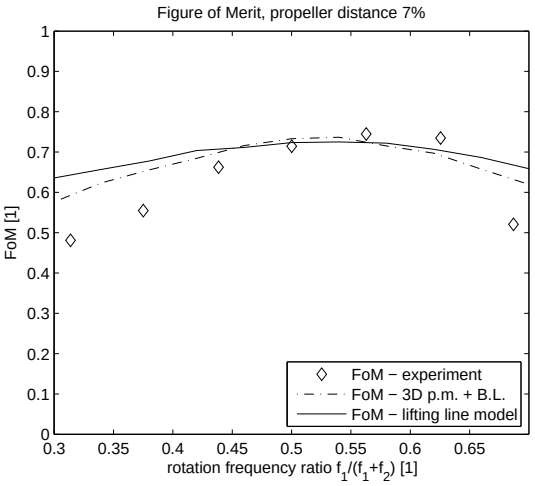


FIGURE 9.9: Figure of Merit vs. ratio of frequency of rotation.

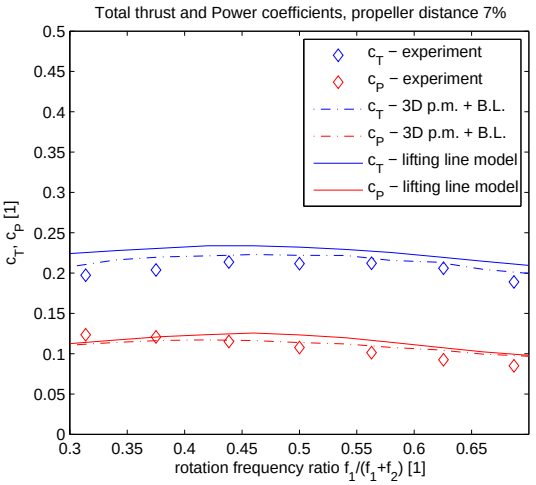


FIGURE 9.10: Total thrust and power coefficients of the system vs. ratio of frequency of rotation.

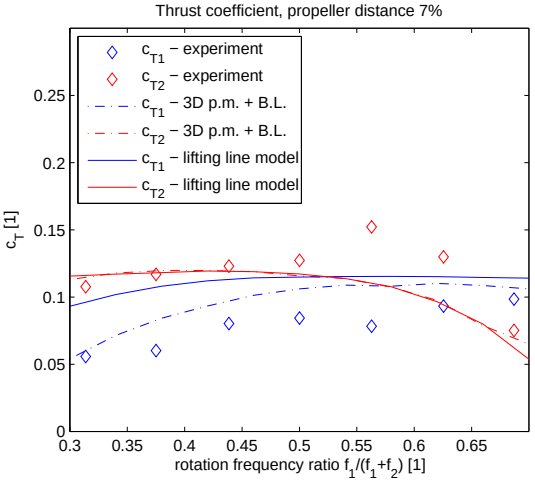


FIGURE 9.11: Individual thrust coefficients of each propeller vs. ratio of frequency of rotation.

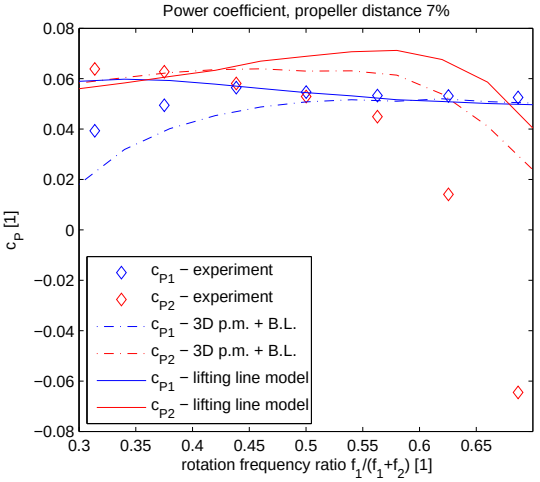


FIGURE 9.12: Individual power coefficients of each propeller vs. ratio of frequency of rotation.

#### 9.2.1.3 Results of acoustic measurement

The overall sound pressure level for various rotational frequency ratios is shown in Fig. 9.13. Sound pressure level has a decreasing tendency with decreasing frequency of rotation of the downstream propeller. Sound pressure level minimum (88 dB) is reached when the downstream propeller rotates at its slowest speed and correspondingly maximum (94 dB) is reached for the highest speed of the downstream propeller. Because these two regimes have very similar aerodynamic performance, it becomes apparent that the overall SPL is dictated by the downstream propeller moving through the disturbed air of the upstream propeller. This is also visible in the frequency spectra, where the main difference lies in the high frequency broadband noise. Reducing the frequency of downstream propeller is one possible solution for lower noise of CRP systems.

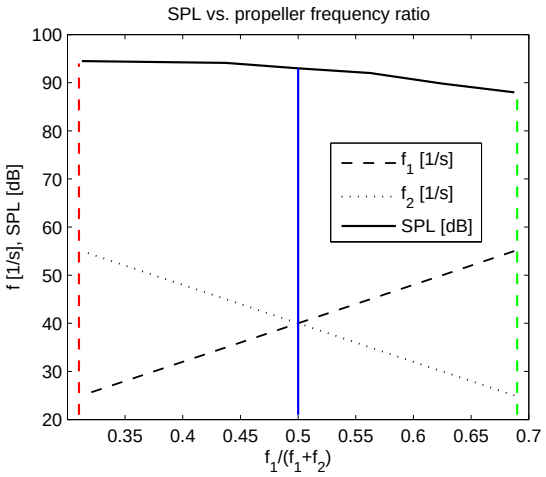


FIGURE 9.13: Sound pressure level vs. rotational frequency ratio.

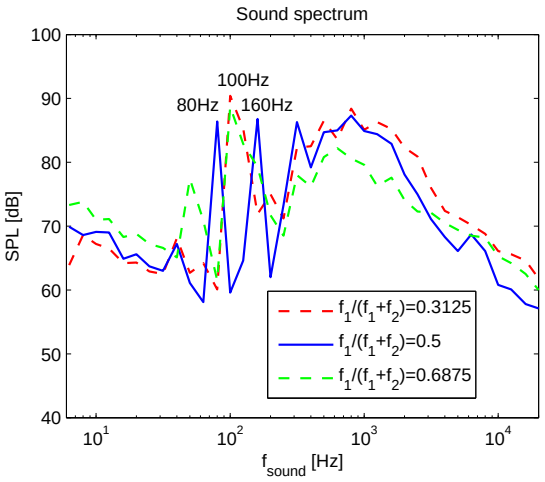


FIGURE 9.14: Sound spectra for selected 3 cases.

Frequency spectra of noise generated at three selected cases of frequency ratios $f_1/(f_1+f_2) = [0.31; 0.5; 0.69]$ is presented in Fig. 9.14. When both propellers rotate at the same frequency, the spectrum shows a significant peak at blade passing frequency, which is twice the rotational frequency for two-bladed propellers $f_{BP} = 2f_1 = 2f_2 = 80Hz$. Each blade of the downstream propeller strikes the wake of an upstream blade 4 times per rotation, which produces a peak in the spectrum at 160Hz. In the other two cases, one propeller was rotating at frequency 25Hz while the other at frequency 55Hz. The spectra look quite similar with a significant peak at 100Hz belonging to the faster propeller. Since blade passing frequency of the faster propeller is $f_{BP} = 2f_{fasterprop} = 110Hz$, the peak should be at this frequency. This difference is attributed to low resolution of the frequency spectra which was measured in third octave bands.

### 9.2.2 Case of variable propeller distance

CRP propeller set PS1 under static thrust conditions is used in propeller distance study. Rotational frequencies are kept equal. The experimental equipment allowed to study only relatively small range of propeller distances between 7% and 14% $D$. Numerical results are presented for a wider range of propeller distances.

#### 9.2.2.1 Results of 3D panel method with boundary layer

Simple momentum theory predicts subtle increase of performance when the propeller distance is increased. This is due to additional air entering between propeller discs. Influence of the propeller distance on Figure o Merit is shown in Fig. 9.15 and thrust sharing is demonstrated on thrust coefficients in Fig. 9.16. Experimental results confirm

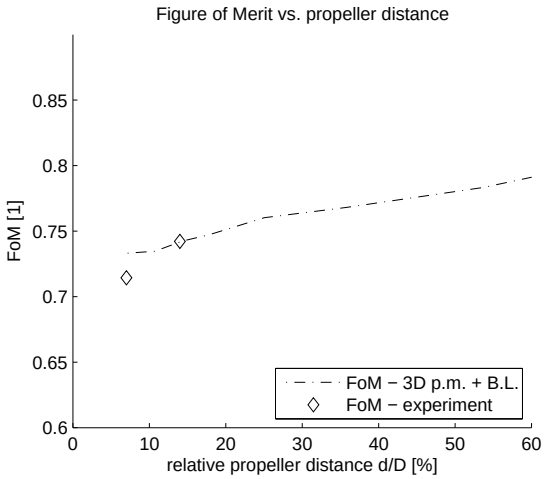


FIGURE 9.15: Figure of Merit vs. propeller distance.

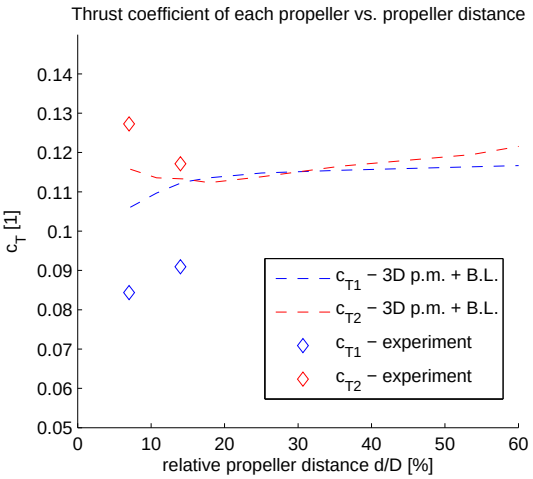


FIGURE 9.16: Thrust coefficient of each propeller vs. propeller distance.

the trends of numerical results although there is up to 7% difference in Figure of Merit and almost 28% difference in $c_{T1}$ between experiment and numerics. The latter is probably again due to mutual influence of thrusts measurement via friction between coaxial shafts.

The numerical results confirm increase of performance ($FoM$) as propeller distance is increased. For propeller distances $7\% \div 20\%$ $D$ rapid thrust redistribution occurs, where the upstream propeller increases its loading and downstream one unloads. The upstream propeller is influenced less and less by the downstream one as the propeller distance and thus induced velocity decreases. On the other hand downstream propeller stays in the slipstream of upstream one so the thrust could remain constant. The fact that the dowstream propeller unloads is probably due to stronger slipstream of the higher loaded upstream propeller.

As the propeller distance increases above 20% $D$, also downstream propeller thrust coefficient increases. This can be caused by vortex wake dissipation and decrease of induced velocities. The limiting case of two contra-rotating propellers an infinite distance apart is equal to the case of two isolated propellers.

#### 9.2.2.2 Results of lifting line method

The Figure of Merit calculated by the lifting line method (Fig. 9.17) has a growing tendency with increasing propeller distance with almost the same gradient as that of 3D panel method results. The individual thrust coefficients (Fig. 9.18) calculated by lifting line method show more erratic behavior than those calculated by 3D panel method. This could be attributed to the lifting line of downstream propeller passing through the wake

being more sensitive to actual wake position and discretization than blade represented by 3D panels.

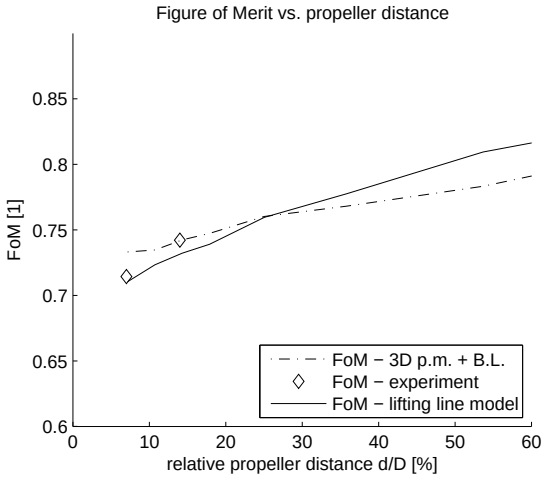


FIGURE 9.17: Figure of Merit vs. propeller distance.

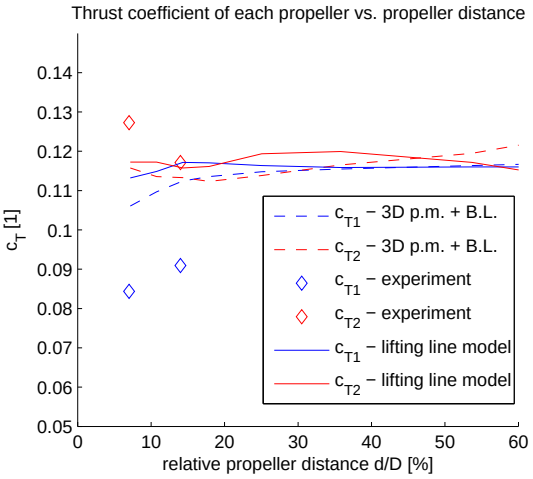


FIGURE 9.18: Thrust coefficient of each propeller vs. propeller distance.

## 9.3 CRP response to variable advance ratio

In the following sections the CRP system is studied using numerical tools only, because no further experimental data was available. Typical curves of thrust, power and efficiency vs. advance ratio for a single propeller were presented in Fig. 9.2. The propeller set PS1 was analyzed using 3D panel method with boundary layer. Figure 9.19 shows the development of force free wake behind CRP system for various advance ratios. For low advance ratios a typical vortex cloud is formed and the vortex sheets behind each blades are hardly distinguished from each other. As the advance ratio rises, the vortex wakes stretch and straighten to form almost a helicoidal surface for a mildly loaded blades. In case of the highest shown advance ratio, the CRP system already acts as a windmill and the rotor and wake is loaded again, but in opposite direction.

Results of both 3D panel method with boundary layer and lifting line model are shown in Figs. 9.20, 9.21 and 9.22.

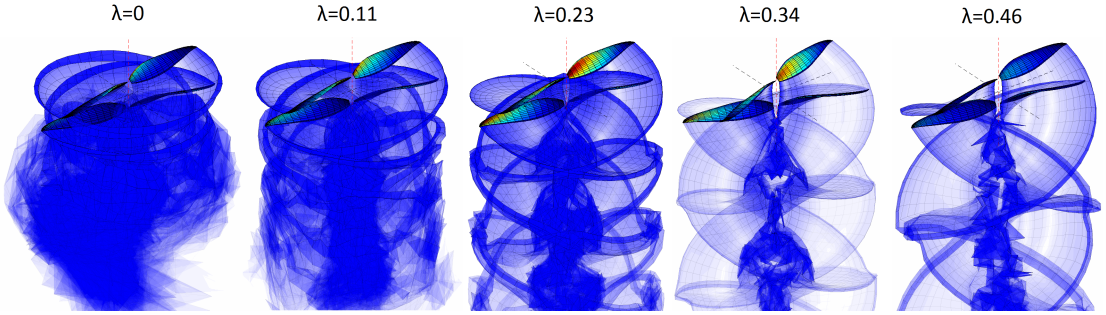


FIGURE 9.19: Development of CRP wakes for selected advance ratios.

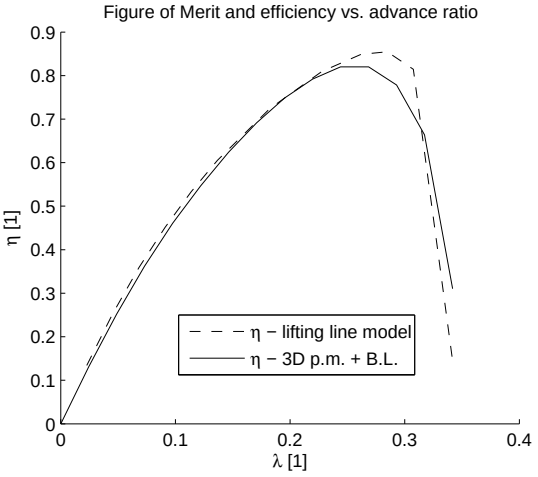


FIGURE 9.20: Efficiency vs. advance ratio.

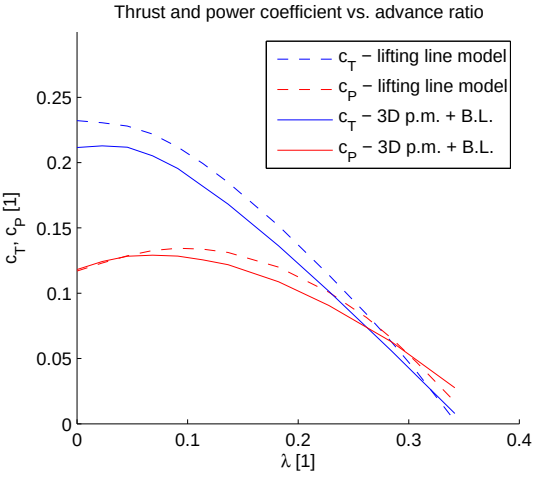


FIGURE 9.21: Overall thrust and power coefficients vs. advance ratio.

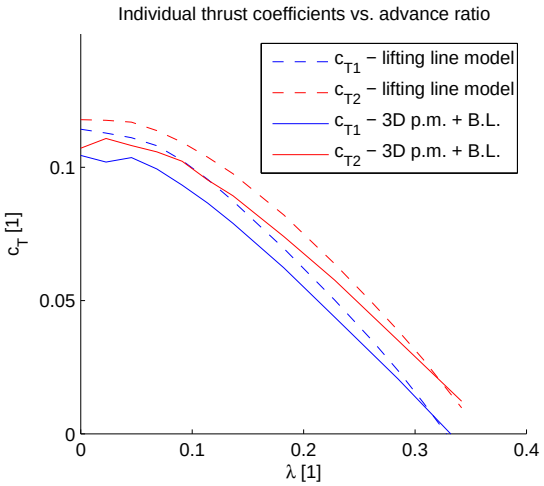


FIGURE 9.22: Individual thrust coefficients of each propeller vs. advance ratio.

## 9.4 Comparison of performance of a CRP and equivalent single propeller

Finding an equivalent propeller to a CRP system can produce different results depending on what kind of equivalence is sought. Here, an equivalent propeller is considered to be a propeller of the same diameter as each of the CRP propellers. For a fair comparison and to achieve the same blade solidity, single propeller is fitted with 4 blades, each of the same geometry as the upstream propeller of the propeller set PS1. The same approach is used for example in Anikin's work [2]. Since the downstream propeller of propeller set PS1 has a slightly larger pitch, it was decided to use (for this case only) a CRP system containing downstream propeller with the same geometry as the upstream one, only mirrored to allow opposite rotation.

The shape of the wake system behind CRP and single propeller is shown in Fig. 9.23. The main difference is that behind CRP system, wakes from each propeller intersect periodically.

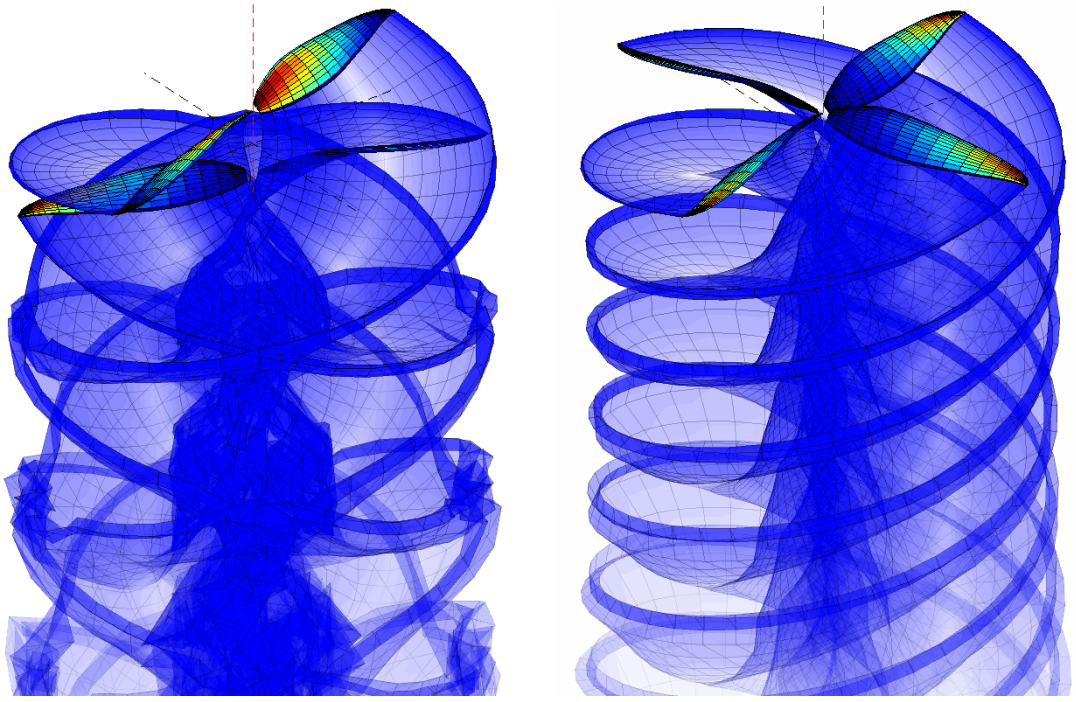

FIGURE 9.23: Wakes behind CRP and equivalent single propeller at $\lambda = 0.23$.

The performance of a contra-rotating propeller set (downstream propeller geometry mirrored from the upstream PS1 geometry) and the performance of an equivalent four-bladed propeller were calculated using 3D panel method with boundary layer for various free stream velocities. Efficiency vs. advance ratio (Fig. 9.24) is surprisingly similar in both cases. The percentage difference of CRP efficiency compared to single propeller

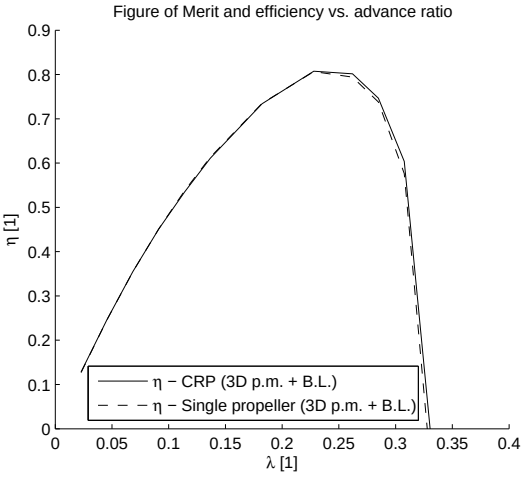


FIGURE 9.24: Efficiency vs. advance ratio.

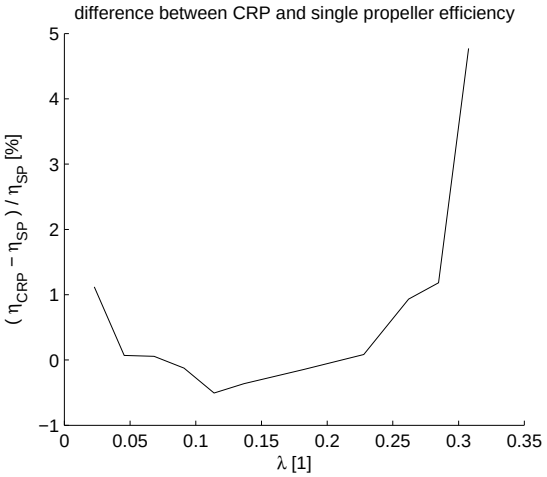


FIGURE 9.25: Difference between efficiency of CRP and single propeller.

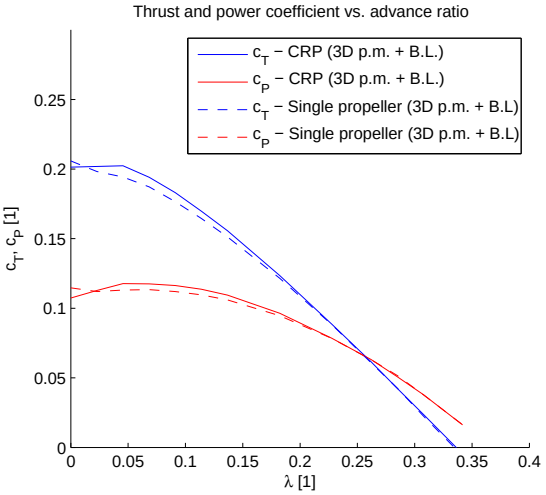


FIGURE 9.26: Overall thrust and power coefficients vs. advance ratio.

is expressed in Fig. 9.25. Against expectations, the efficiency of a CRP system is only slightly higher in case of higher advance ratios and lower for $\lambda = 0.05 \div 0.2$. Explanation is provided by Figure 9.26, which shows that thrust coefficients are noticeably higher in case of CRP for $\lambda = 0.05 \div 0.2$. It follows from the momentum theory, that higher loading of the propeller disc brings decrease in efficiency. The expected reduction of wake swirl losses (see Eq. 2.7) and its effect on efficiency has been overcome by increased induced power losses due to higher loading.

To evaluate the true efficiency difference, CRP and single propeller should be compared at the same thrust coefficient and advance ratio conditions. One option is to slightly modify the geometry of the blades so the thrust performance matches in the whole range of advance ratios. However this process is lengthy and success is not guaranteed. Second option, which was ultimately chosen, is to correct the efficiency of the CRP results using correction factor calculated as the ratio of: efficiency of ideal propulsor

at thrust of single propeller to the efficiency of ideal propulsor at thrust of CRP. This correction factor should provide reliable results as long as the difference between the thrust coefficients of the two propulsion systems compared is small. Figure 9.27 shows comparison of efficiency of single propeller as calculated by the panel method, efficiency of an ideal propulsor of the same disc area and thrust as single propeller and finally efficiency of CRP system corrected to the same thrust as that of single propeller. Figure 9.28 presents the percentage difference between CRP and single propeller efficiency and shows also corrected values using correction described above.

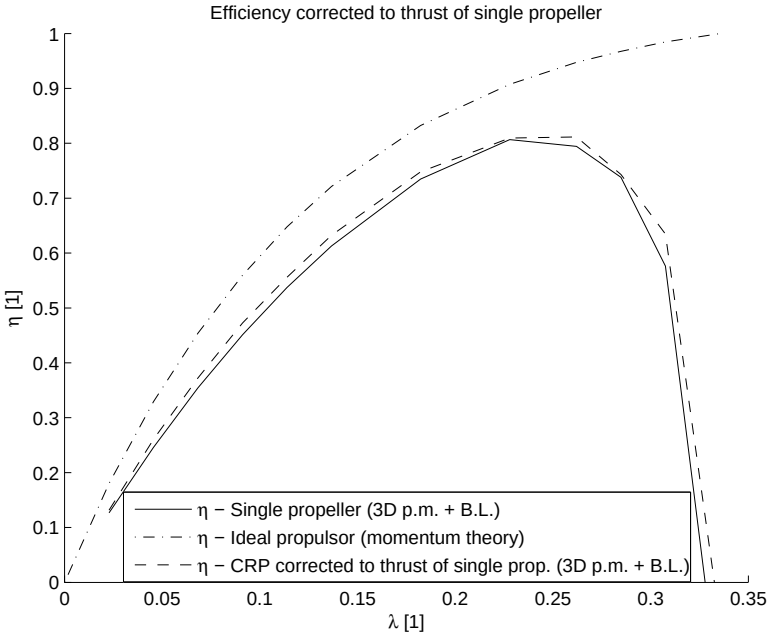


FIGURE 9.27: Efficiency of propulsion systems at the same thrust vs. advance ratio.

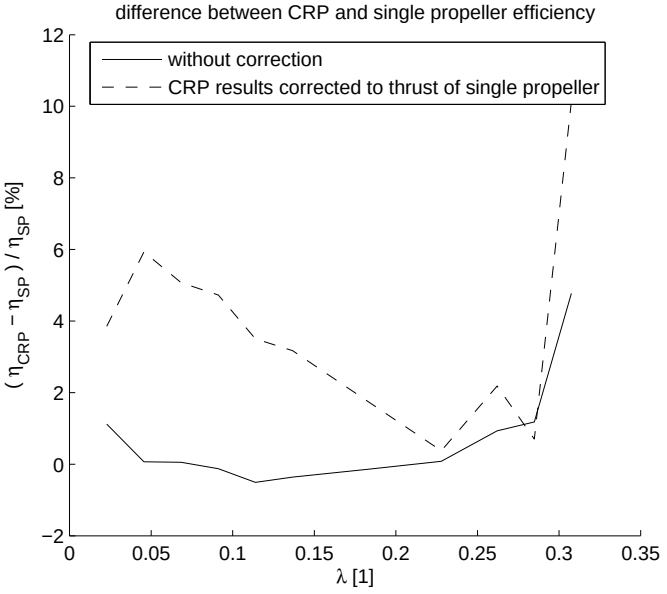


FIGURE 9.28: Difference between efficiency of CRP and single propeller.

## 9.5 CRP in off-axis flow conditions

During flight of a multicopter UAV, the angle between free stream velocity and axis of rotation of CRP is generally non-zero and can reach e.g. $\varphi = 60 \div 80°$ in forward flight or even $\varphi > 90°$ when braking. In such conditions, simpler models with axi-symmetric assumption are not usable.

To investigate the behavior of CRP system, the following case was studied. Propeller set PS1 rotates with equal rotational frequency $f_1 = f_2 = 50Hz$. Axial component of the free stream velocity produces advance ratio ($\lambda = 0.06$) and remains constant throughout the simulation. The component of free stream velocity perpendicular to the axis of rotations starts at 0 ($\varphi = 0°$) and is increased gradually to twice the value of axial component. The range of angle of inflow is therefore $\varphi = 0 \div 63°$.

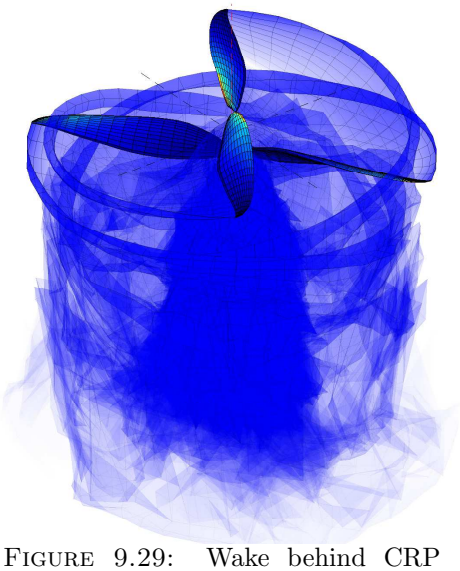

FIGURE 9.29: Wake behind CRP with axial inflow.

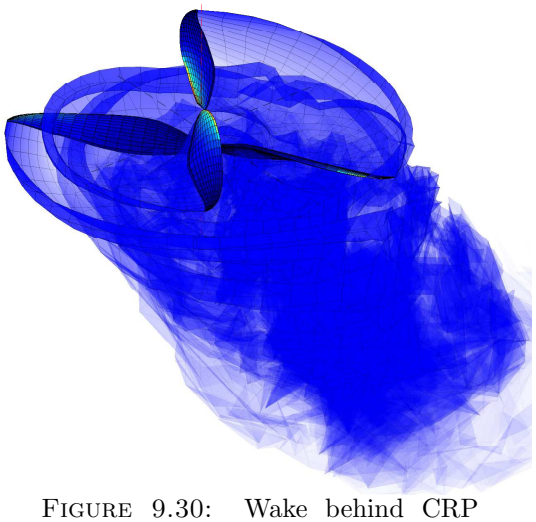

FIGURE 9.30: Wake behind CRP with 60° inflow.

Shape of the wake under two selected angles of free stream velocity is shown in Fig. 9.29 and 9.30. Figure of Merit and efficiency as a function of inflow angle is presented in Fig. 9.31. Both efficiency and advance ratio are provided due to low value of $\lambda$. The result (Fig. 9.31) show that $FoM$ and efficiency are quite insensitive to angle of free stream velocity. Only at high angles of free stream above 30° the performance begins to rise gradually. This effect exist also in single rotor helicopters and results in forward flight being more efficient than hover. Individual thrust coefficients are shown in Fig. 9.32.

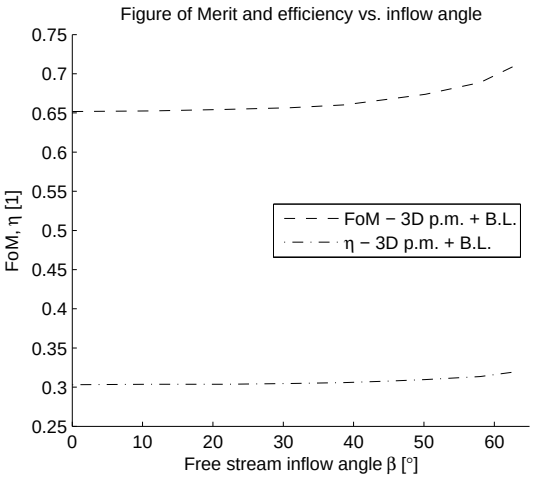


FIGURE 9.31: Figure of Merit and efficiency vs. inflow angle.

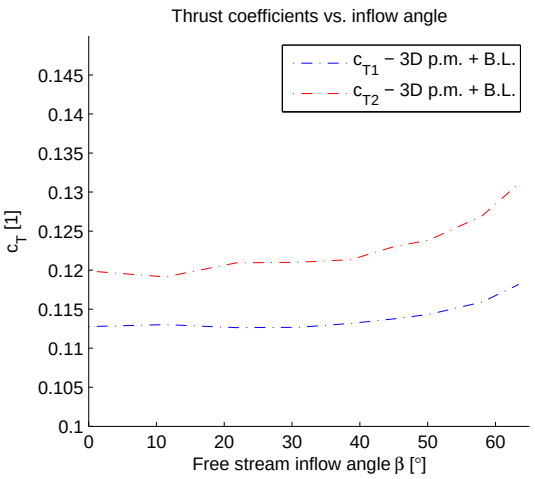


FIGURE 9.32: Individual thrust coefficients vs. inflow angle.

## 9.6 Discussion

The overall match of experimental and numerical data meets and exceeds expectations for a fast analysis and design tool. The numerical prediction is less consistent in conditions where blade flow separation exists as can be expected. Model based on 3D panel method with boundary layer performs slightly better compared to lifting line model regarding the match with experiment. More experimental data for different propellers or even wind tunnel test would be beneficial to accurately determine the range of applicability of both methods.

The performance curves and behavior of a CRP system are not much different from a single propeller. A contra-rotating propeller system is able to get the maximum performance out of a given propeller disc area due to a)reduction of swirl losses and b) additional air being sucked in between the propeller discs. The first factor depends on the design of the propellers, which must be carefully matched together. The second factor is influenced mainly by the propeller distance. With higher propeller distance the investigated propeller set showed modest increase in performance and audible reduction of noise. Comparison of CRP system and equivalent single propeller showed $1 \div 6\%$ increase of efficiency depending on the advance ratio. This might no be enough to justify practical application due to inherent noise issues, complexity and added weight and costs of the contra-rotating systems. However the benefits of nearly zero reaction torque are important in some designs.

When larger propellers than those studied in this work are designed, compressibility effects come to play. It might be often necessary to design propellers with high power coefficients at relatively high advance ratios, because the rotation rate is limited by tip Mach numbers. In these cases the swirl losses are increased and the propulsion system

may greatly benefit from the use of contra-rotating propellers. The application of CRPs on Russian heavy bomber TU-95 was driven by the need of reducing swirl losses due to high flight speed and limited propeller rotational rate by tip Mach number.

Performance of the investigated CRP system in off-axis flow was very insensitive to the directional angle up to a point, where the performance started to increase due to additional lift known from aerodynamics of horizontal flight of helicopters.

# Chapter 10

# Conclusions and Recommendations

Two different computational models for analysis of contra-rotating propeller aerodynamics were successfully developed, tested and used for exploring the properties of the unsteady flow of incompressible fluid through a CRP system. The main difference between the two models is the representation of propeller blades.

The simpler lifting line based model uses segments of bound vortex across the span of a blade and appropriate airfoil polars to calculate circulation, lift and drag corresponding to the local velocity conditions. This model is a materialization of well-known principles and features only slight improvements to the core method. It serves as a reference for the other more advanced numerical model which contains some new and unique components.

The second computational model uses actual body surface discretization and an inviscid 3D panel method solver for blade representation. To include the effects of viscosity, 2D boundary layer is calculated along surface streamlines with a new method of coupling between inviscid and viscous regions.

An important component of both lifting line and 3D panel models is a force-free wake. The results of simple test cases from Chapter 5 demonstrate that vorticity, whether in form of point or line vortices, is a powerful and fast tool for modelling of wakes. Inclusion of a vortex core model with core radius growth contributed to the stability of the solution by removing singularity problems. Functionality of the force-free wake was demonstrated on the case of an oscillating finite wing.

The two numerical models when applied on an actual case of contra-rotating propellers both provide results in good agreement with experiment. Best match of numerical and experimental data is obtained by 3D panel method with boundary layer. Lifting line

model of the blade, despite its simplicity, provides only slightly worse match. This can be attributed to excellent 2D polar data calculated by XFOIL and low influence of three-dimmensional flow effects. The 3D panel method without boundary layer regularly overpredicts performance, which illustrates the importance of calculating boundary layer in low Reynolds number flows.

A CRP system boasts very similar performance characteristics as equivalent single propeller. However, there are several differences. Most notably it is the increased noise formed by the downstream propeller passing through the wakes of the upstream blades. The passage is also well visible in the time plots of thrust and power during one rotation. Although some power losses due to highly unsteady character of loading of the downstream blades are unavoidable, results indicate, that the swirl losses recovered by the second propeller easily compensate for any such losses and net decrease in power consumed by CRP is observed compared to equivalent single propeller at the same thrust levels.

## 10.1 Contribution to the state-of-the-art

Contribution to the state-of-the-art can be divided into two main fields. First, rather theoretical field is the development of numerical methods which incorporates basic research. The second field of applied research brings advances in understanding contra-rotating propeller aerodynamics using the newly developed models and also results of original experimental research.

### 10.1.1 Contribution in the field of computational methods

Coupling between inviscid 3D panel method and integral two equation 2D boundary layer model is performed using new interaction model. So called “portable” boundary layer formulation is presented using linear interaction law and replacement inviscid model (Eq. (7.39)) in section 7.5.3. Both the replacement inviscid model and interaction law benefit from fast method of estimation of interaction coefficients shown in Eq. (7.36). As a result, the calculation of boundary layer along selected streamlines on the surface of a rigid body proceeds without the need of 3D panel method solution between subsequent boundary layer passes.

Results of experimental and numerical verifications on cases of CRP system and finite wing show promising results and suggest that this solution could be quite useful in wide ranges of low Reynolds numbers problems of flow past streamlined bodies. The

method is especially useful in cases, where simpler methods such as lifting line or lifting surface methods with vortex wake struggle to produce accurate solutions. These difficult cases include low aspect ratio wings and blades, highly loaded rotors, blade and wing geometries with high sweep angle or rapid changes in planform shape or airfoil shape.

During construction of the simpler lifting line model representation of propeller blades, an issue with vorticity distribution near tip resulted in its thorough investigation and two solutions of the tip problem, which can be found in Section 6.1.3. This tip treatment significantly improves the solution near blade or wing tip and enables the use of more bound vortex segments without introducing numerical instability.

### 10.1.2 Contribution in the field of propeller aerodynamics

The presented work contains original results of experimental research on contra-rotating fixed pitch small scale aircraft propellers. The remaining published work on the CRP topic uses commercial CFD packages for analysis, with limited extent of results due to computational power requirements. Presented work fills the gap with complete results of CRP analysis using in-house developed and verified numerical tool. According to the research of literature the presented work is the first to use a fully coupled boundary layer model with a 3D potential flow solver in research of propellers in general. Thanks to the boundary layer simulation, the computational model provides more precise results under design conditions and realistic prediction even under off-design conditions with some separation present. Several scenarios were studied and discussed. The following conclusions about the performance of CRP systems were reached:

- Response of a contra-rotating propeller system to change of ratio of frequencies of rotation showed that peak Figure of Merit is obtained for slightly different propeller rotational frequency ratio than 1:1. Although the most effective ratio depends on the exact geometry and conditions, it can be generalized that by controlling the ratio of rotation of propellers throughout the operation range, overall efficiency can be increased.

- Increasing propeller distance redistributes thrusts and slightly increases the values of Figure of Merit, while reducing noise. Propellers should be placed as far apart as possible and practical.

- Performance of a CRP system is initially insensitive to angle of off-axis free-stream velocity, only at angle higher than 30° the efficiency begins rising due to the effect of additional lift provided by forward flight component of velocity.

- CRP system and equivalent single propeller of the same diameter and blade solidity must be compared strictly at the same thrust level, otherwise incorrect conclusions may be drawn. At the same thrust levels, contra-rotating propeller system provides $1 \div 6\%$ increase in efficiency over equivalent single propeller. The increase is more evident for low advance ratios, where the propellers are more loaded.

- Both upstream and downstream propellers are subject to fluctuating thrust force. The upstream propeller experiences rather smooth and gradual changes of thrust, while the downstream propeller is subject to sharp peaks in thrust when the blades pass through wakes. Power of the upstream propeller is almost constant in time, while the power of downstream propeller suffers peaks corresponding to thrust oscillations.

## 10.2 Recommendations on the future work

The results obtained so far indicate that the computational model is very capable. One direction of future research is the application of the complete model "as it is" to other similar problems of fluid dynamics, such as vertical axis wind turbines or research of aerodynamics of various unmanned aerial vehicles. It is quite natural to use such methods for large scale optimizations that are not possible with current computers and finite volume CFD methods due to prohibitive computational time. Parameters such as propeller geometry and rotational rate ratio can be optimized to maximize propulsion efficiency or Figure of Merit. Minor improvements can be still made to enhance the speed of the presented method. Gradual simplification of wake panel geometry far from the propellers can be done by combining several panels into one. Boundary layer variables are initialized every time step. Using values from previous time step could also speed up the solution.

Further experimental work could provide additional data for precise setting of the numerical model. Performing wake visualization and velocity field measurement can help with setting of initial vortex size and rate of dissipation in the wake.

Another direction of future research is to extend the fields of application of the current model. Even small scale propellers often operate at high subsonic Mach tip speed. Compressibility effects can be accounted for by simple corrections such as Prandtl-Glauert or Kármán-Tsien compressibility corrections. Although the method is not suitable for cases of completely internal flow, some features, such as ducts and hubs, could be produced, either using 3D panel bodies, or axisymmetric bodies formed by vortex rings. After

such modification, it would be possible to model ventilation fans, ducted fans and similar engineering problems, including contra-rotating configurations and configurations with stator blades. Addition of effects from bluff bodies such as separated flow behind mast of a VAWT is problematic but not impossible through careful implementation of source elements.

# References


[1] Coleman, C. P. (1997). A survey of theoretical and experimental coaxial rotor aerodynamic research. Tech. Rep. 3675, NASA.

[2] Anikin, V. A. (1991). Aerodynamic features of a coaxial rotor helicopter. Tech. Rep. ERF91-66, Kamov Helicopter Scientific and Technology Company.

[3] Ramasamy, M. (2013). Measurements comparing hover performance of single, coaxial, tandem and tilt-rotor configurations. In: *AHS 69th Annual Forum*. pp. 1–23.

[4] Cambier, L., Heib, S. and Plot, S. (2013). The Onera elsA CFD software: input from research and feedback from industry. *Mechanics & Industry*, vol. 14, pp. 159–174. ISSN 2257-7777.

[5] Boisard, R., Delattre, G. and Falissard, F. (2011). Assessment of aerodynamics and aero-acoustics tools for open rotors. In: *9th European Turbomachinery Conference*. pp. 21–25. ISBN 978-975-561-389-5.

[6] Beaumier, P. (2014). A low order method for co-axial propeller and rotor performance prediction. In: *29th Congress of the International Council of the Aeronautical Sciences*. pp. 1–11. Hal-01079555.

[7] Rand, O. and Khromov, V. (2010). Aerodynamic optimization of a coaxial rotor in hover and axial flight. In: *27th International Congress of the Aeronautical Sciences*. IACS, pp. 1–13.

[8] Ghassemi, H. (2009). Hydrodynamic performance of coaxial contra-rotating propeller (ccrp) for large ships. *Polish Maritime Research*, vol. 59(1), pp. 22–28. ISSN 1233-2585.

[9] Takinaci, A. C. and Atlar, M. (2001). On the importance of boundary layer calculations instead of viscous correction in heavily loaded marine propellers while using a surface panel method. *Ocean Engineering*, vol. 28, pp. 519–536. ISSN 0029-8018.

[10] Brizzolara, S., Villa, D. and Gaggero, S. (2008). A systematic comparison between RANS and panel methods for propeller analysis. In: *8th International Conference on Hydrodynamics*. pp. 1–13.

[11] Kuik, G. A. M. v., Sørensen, J. N. and Okulov, V. L. (2015). Rotor theories by proffesor Joukowsky: Mometum theories. *Progress in Aerospace Sciences*, vol. 73, pp. 1–18. ISSN 0376-0421.

[12] Okulov, V. L., Sørensen, J. N. and Wood, D. H. (2015). Rotor theories by proffesor Joukowsky: Vortex theories. *Progress in Aerospace Sciences*, vol. 73, pp. 20–45. ISSN 0376-0421.

[13] Alexandrov, V. L. (1954). *Letecké Vrtule*. Praha: SNTL.

[14] Wald, Q. R. (2006). The aerodynamics of propellers. *Progress in Aerospace Sciences*, vol. 42, pp. 85–128. ISSN 0376-0421.

[15] Froude, R. E. (1889). On the part played in propulsion by differences of fluid pressure. *Transactions of the Institute of Naval Architects*, vol. 30, pp. 390–405.

[16] Katz, J. and Plotkin, A. (2001). *Low-Speed Aerodynamics*. Cambridge Aerospace Series, Cambridge University Press. ISBN 9780521665520.

[17] Brož, V. (1990). *Aerodynamika nízkých rychlostí*. Praha: Ediční středisko ČVUT. ISBN 80-01-00198-9.

[18] Kerwin, J. E. (1961). The solution of propeller lifting surface problems by vortex lattice methods. Tech. rep., MIT - Department of Naval Architecture and Marine Engineering.

[19] Hess, J. L. and Valarezo, W. O. (1985). Calculation of steady flow about propellers using a surface panel method. *Journal of Propulsion and Power*, vol. 1(6), pp. 470–476. ISSN 0748-4658.

[20] Hsin, C. (1990). *Development and Analysis of Panel Methods for Propellers in Unsteady Flow*. Ph.D. thesis, Massachusetts Institute of Technology.

[21] Milewski, W. M. (1997). *Three-dimensional viscous flow computations using the integral boundary layer equations simultaneously coupled with a low order panel method*. Ph.D. thesis, Massachusetts Institute of Technology.

[22] Leishman, J. G. and Ananthan, S. (2006). Aerodynamic optimization of a coaxial proprotor. In: *62nd American Helicopter Society International Annual Forum*. p. 64.

[23] Heyong, X. and Zhengyin, Y. (2011). Numerical simulation of unsteady flow around forward flight helicopter with coaxial rotors. *Chinese Journal of Aeronautics*, vol. 24(1), pp. 1–7. ISSN 1000-9361.

[24] Kim, H. W. and Brown, R. E. (2010). A comparison of coaxial and conventional rotor performance. *Journal of the American Helicopter Society*, vol. 55(1), pp. 12004–12004. ISSN 0002-8711.

[25] Yang, C., Tamashima, M., Wang, G. Q., Yamazaki, R. and Koizuka, H. (1992). Prediction of the unsteady performance of contra-rotating propellers by lifting surface theory. *Transactions of the West-Japan Society of Naval Architects*, vol. 83, pp. 17–31.

[26] Paik, K., Hwang, S., Jung, J., Lee, T., Lee, Y., Ahn, H. and Van, S. (2015). Investigation on the wake evolution of contra rotating propeller using RANS computation and SPIV measurement. *International Journal of Naval Architecture and Ocean Engineering*, vol. 7(3), pp. 595–609. ISSN 2092-6782.

[27] Harrington, R. D. (1951). Full-scale-tunnel investigation of the static-thrust performance of a coaxial helicopter rotor. Tech. Rep. 2318, NASA.

[28] Dingeldein, R. C. (1954). Wind-tunnel studies of the performance of multirotor configurations. Tech. Rep. 3236, NASA.

[29] Huo, C., Barenes, R. and Gressier, J. (2015). Experimental analysis of the aerodynamics of long-shrouded contrarotating rotor in hover. *Journal of AHS*, vol. 60(4), pp. 1–12. ISSN 0002-8711.

[30] Simoes, C. (undated). Optimizing a coaxial propulsion system to a quadcopter. Tech. rep., Instituto Superior Tecnico.

[31] Miller, M. L. (1976). Experimental determination of unsteady forces on contrarotating propellers in uniform flow. Tech. Rep. SPD 659-01, David W. Taylor Naval Ship Research and Development Center.

[32] Cummings, R. M., Mason, W. H., Morton, S. A. and McDaniel, D. R. (2015). *Applied Computational Aerodynamics: A Modern Engineering Approach*, vol. 53. Cambridge University Press. ISBN 1107053749.

[33] Drela, M. (1989). XFOIL – An analysis and design system for low Reynolds number airfoils. *Low Reynolds number aerodynamics*.

[34] Hess, J. (1972). Calculation of potential flow about arbitrary three dimensional lifting bodies. Tech. Rep. MDC J5679-01, McDonnell Douglas Corporation, Long Beach, CA.

[35] Lewis, R. (2005). *Vortex Element Methods for Fluid Dynamic Analysis of Engineering Systems*. Cambridge Engine Technology Series, Cambridge University Press. ISBN 9780521017541.

[36] Smith, A. and Hess, J. (1962). Calculation of non-lifting potential flow about arbitrary three-dimensional bodies. Tech. Rep. E.S. 40622, Douglas Aircraft Company, Inc., Long Beach, CA.

[37] Morino, L. and Kuot, C. (1974). Subsonic potential aerodynamics for complex configurations: A general theory. *AIAA Journal*, vol. 12, pp. 191–197. ISSN 0001-1452.

[38] Erickson, L. (1990). Panel methods - an introduction. Tech. Rep. Technical Paper 2995, NASA, Ames Research Center, Moffet Field, CA.

[39] Koochesfahani, M. M. (1989). Vortical patterns in the wake of an oscillating airfoil. *AIAA Journal*, vol. 27, pp. 1200–1205. ISSN 0001-1452.

[40] Hommes, T., Bosschers, J. and Hoeijmakers, H. W. M. (2015). Evaluation of the radial pressure distribution of vortex models and comparison with experimental data. In: *9th International Symposium on Cavitation*. IOP Publishing, pp. 1–4. ISSN 1742-6588.

[41] Lamb, H. (1916). *Hydrodynamics, Fourth edition*. London: Cambridge University Press.

[42] Burnham, D. C. and Hallock, J. N. (1982). Chicago monostatic acoustic vortex sensing system. Tech. Rep. DOT-TSC-FAA-79-104.IV, Transportation Systems Center Cambridge MA.

[43] Vatistas, G. H., Kozel, V. and Mih, W. C. (1991). A simpler model for concentrated vortices. *Experiments in Fluids*, vol. 11, pp. 73–76. ISSN 0723-4864.

[44] Saffman, P. G. (1992). *Vortex Dynamics*. Cambridge Monographs on Mechanics, Cambridge University Press. ISBN 978-0521477390.

[45] de Vaal, J. B., Hansen, M. O. L. and Moan, T. (2014). Validation of a vortex ring wake model suited for aeroelastic simulations of floating wind turbines. In: *The Science of Making Torque from Wind 2012*. IOP Publishing, pp. 1–10. ISSN 1742-6588.

[46] Batchelor, G. K. (1967). *Introduction to Fluid Dynamics*. Cambridge University Press. ISBN 0521663962.

[47] Anathan, S. and Leishman, J. (2004). Role of filament strain in the free-vortex modeling of rotor wakes. *Journal of the American Helicopter Society*, vol. 49(2), pp. 176–191. ISSN 0002-8711.

[48] Piziali, R. A. (1994). 2-d and 3-d oscillating wing aerodynamics for a range of angles of attack including stall. Tech. Rep. 94-A-011, NASA.

[49] Ashby, D. (1999). *Potential flow theory and operation guide for the panel code PMARC_14*. NASA, Ames Research Center, Moffet Field, CA. TM-1999-209582.

[50] Sørensen, J. N., Dag, K. and Ramos-García, N. (2014). A new tip correction based on the decambering approach. In: *The Science of Making Torque from Wind 2014*. IOP Publishing, pp. 1–11. ISSN 1742-6588.

[51] Monsch, S. C. (2007). *A Study of Induced Drag and Spanwise Lift Distribution for Three-Dimensional Inviscid Flow Over a Wing*. Master's thesis, Clemson University.

[52] Drela, M. . and Giles, M. (1987). Viscous-inviscid analysis of transonic and low Reynolds number airfoils. *AIAA Journal*, vol. 25(10), pp. 1347–1355. ISSN 0001-1452.

[53] Johansen, J. (1997). *Prediction of laminar/turbulent transition in airfoil flows*. Roskilde: Risø National Laboratory. ISBN 87-550-2308-8.

[54] Green, J. E., Weeks, D. and Brooman, J. (1977). Prediction of turbulent boundary layers and wakes in compressible flow by a lag-entrainment method. *NASA STI/Recon Technical Report N*, vol. 77.

[55] Veldman, A. E. P. (1981). New, quasi-simultaneous method to calculate interacting boundary layers. *AIAA Journal*, vol. 19(1), pp. 79–85. ISSN 0001-1452.

[56] Bijleveld, H. and Veldman, A. E. P. (2013). Prediction of unsteady flow over airfoils using a quasi-simultaneous interaction method. Tech. rep., ECN Wind Energy.

[57] Schlichting, H. and Gersten, K. (2000). *Boundary-layer theory*. New York: Springer. ISBN 3-540-66270-7.

[58] Hartree, D. R. (1937). On an equation occuring in falkner and skan's aproximate treatment of the equations o the boundary layer. *Proc. Cambridge. Phil. Soc.*, vol. 33(2), pp. 223–239.

[59] Goldstein, S. (1948). On laminar boundary-layer flow near a position of separation. *The Quarterly Journal of Mechanics and Applied Mathematics*, vol. 1(1), pp. 43–69.

[60] Veldman, A. E. P. (2009). A simple interaction law for viscous–inviscid interaction. *Journal of Engineering Mathematics*, vol. 65(4), pp. 367–383. ISSN 0022-0833.

[61] Eppler, R. (2003). About classical problems of airfoil drag. *Aerospace Science and Technology*, vol. 7(4), pp. 289–297. ISSN 1270-9638.

[62] Giles, M. B. and Cummings, R. M. (1999). Wake integration for three-dimensional flowfield computations: Theoretical development. *Journal of Aircraft*, vol. 36(2), pp. 357–365. ISSN 0021-8669.

# Cited work of the author


[A1] Štorch, V., Nožička, J., Brada, M. and Suchý, J. (2016). Measurement of noise and its correlation to performance and geometry of small aircraft propellers. In: *Experimental Fluid Mechanics 2015*. vol. 116 of *EPJ Web of Conferences*, pp. 1–6. ISSN 2100-014X.

[A2] Štorch, V. and Nožička, J. (2016). A novel computational model for the analysis of contra-rotating propellers. In: *Fluid Mechanics and Thermodynamics, Proceedings of Students' Work in the Year 2015/2016*. Prague: Czech Technical University in Prague, Faculty of Mechanical Engineering, pp. 95–105. ISBN 978-80-86786-38-4.

[A3] Štorch, V., Nožička, J., Brada, M. and Suchý, J. (2015). Experimental verification of computational model for wind turbine blade geometry design. In: *Experimental Fluid Mechanics 2014*. Český Krumlov: Technical University of Liberec, vol. 92 of *EJP Web of Conferences*, pp. 1–6. ISSN 2101-6275.

[A4] Štorch, V. and Nožička, J. (2014). 3D panel methods for turbomachinery design. In: *Fluid Mechanics and Thermodynamics, Proceedings of Students' Work in the Year 2013/2014*. Prague: Czech Technical University in Prague, Faculty of Mechanical Engineering, pp. 43–51. ISBN 978-80-86786-36-0.

[A5] Štorch, V. and Nožička, J. (2015). On viscous-inviscid interaction for boundary layer calculation using two-equation integral method. In: *Fluid Mechanics and Thermodynamics, Proceedings of Students' Work in the Year 2014/2015*. Prague: Czech Technical University in Prague, Faculty of Mechanical Engineering, pp. 81–97. ISBN 978-80-86786-37-7.

[A6] Štorch, V. and Nožička, J. (2017). Verification and possible applications of new 3D panel method with boundary layer. In: *Fluid Mechanics and Thermodynamics, Proceedings of Students' Work in the Year 2016/2017*. Prague: Czech Technical University in Prague, Faculty of Mechanical Engineering, pp. 29–46. ISBN 978-80-86786-39-1.

[A7] Štorch, V., Nožička, J. and Brada, M. (2017). Experimental setup for measurement of contra-rotating propellers. In: *Topical Problems of Fluid Mechanics 2017*. Prague: Institute of Thermomechanics ASCR, pp. 285–294. ISSN 2336-5781.

[A8] Štorch, V. and Nožička, J. (in press). Contra-rotating propeller aerodynamics solved by a 3D panel method with coupled boundary layer. *Acta Polytechnica*.

[A9] Filipský, J. and Štorch, V. (2014). Comparison of propeller analysis methods and experimental data. In: *Engineering Mechanics 2014*. Brno University of Technology, pp. 172–175. ISSN 1805-8248.

# Appendix A

# Constant Source Quadrilateral Panel

A flat constant source quadrilateral panel has a rather lenghty formulation of induced velocity components. The formulas were derived by Hess [36],[34] and are given here in the form presented in [16]. The calculation is performed in the panel local coordinate frame, with $\bar{x}$ and $\bar{y}$ axis aligned with the panel and $\bar{z}$ axis normal to the panel. $\bar{x}_1, .., \bar{x}_4, \bar{y}_1, .., \bar{y}_4, \bar{z}_1, .., \bar{z}_4$ are the panel corner points in the local coordinates.

$$c_{\bar{x}} = \frac{\sigma}{4\pi}\left[\frac{\bar{y}_2-\bar{y}_1}{d_{12}} ln\left(\frac{r_1+r_2-d_{12}}{r_1+r_2+d_{12}}\right) + \frac{\bar{y}_3-\bar{y}_2}{d_{23}} ln\left(\frac{r_2+r_2-d_{23}}{r_2+r_3+d_{23}}\right) + \frac{\bar{y}_4-\bar{y}_3}{d_{34}} ln\left(\frac{r_3+r_4-d_{34}}{r_3+r_4+d_{34}}\right) + \frac{\bar{y}_1-\bar{y}_4}{d_{41}} ln\left(\frac{r_4+r_1-d_{41}}{r_24+r_1+d_{41}}\right)\right] \quad \text{(A.1)}$$

$$c_{\bar{y}} = \frac{\sigma}{4\pi}\left[\frac{\bar{x}_2-\bar{x}_1}{d_{12}} ln\left(\frac{r_1+r_2-d_{12}}{r_1+r_2+d_{12}}\right) + \frac{\bar{x}_3-\bar{x}_2}{d_{23}} ln\left(\frac{r_2+r_2-d_{23}}{r_2+r_3+d_{23}}\right) + \frac{\bar{x}_4-\bar{x}_3}{d_{34}} ln\left(\frac{r_3+r_4-d_{34}}{r_3+r_4+d_{34}}\right) + \frac{\bar{x}_1-\bar{x}_4}{d_{41}} ln\left(\frac{r_4+r_1-d_{41}}{r_24+r_1+d_{41}}\right)\right] \quad \text{(A.2)}$$

$$c_{\bar{z}} = \frac{\sigma}{4\pi}\left[tan^{-1}\left(\frac{m_{12}e_1 - h_1}{\bar{z}r_1}\right) - tan^{-1}\left(\frac{m_{12}e_2 - h_2}{\bar{z}r_2}\right)\right.$$
$$+ tan^{-1}\left(\frac{m_{23}e_2 - h_2}{\bar{z}r_2}\right) - tan^{-1}\left(\frac{m_{23}e_3 - h_3}{\bar{z}r_3}\right)$$
$$+ tan^{-1}\left(\frac{m_{34}e_3 - h_3}{\bar{z}r_2}\right) - tan^{-1}\left(\frac{m_{34}e_4 - h_4}{\bar{z}r_4}\right)$$
$$\left. + tan^{-1}\left(\frac{m_{41}e_4 - h_4}{\bar{z}r_2}\right) - tan^{-1}\left(\frac{m_{41}e_1 - h_1}{\bar{z}r_1}\right)\right] \quad \text{(A.3)}$$

Where:

$$d_{12} = \sqrt{(\bar{x}_2 - \bar{x}_1)^2 + (\bar{y}_2 - \bar{y}_1)^2} \quad \text{(A.4)}$$
$$d_{23} = \sqrt{(\bar{x}_3 - \bar{x}_2)^2 + (\bar{y}_3 - \bar{y}_2)^2} \quad \text{(A.5)}$$
$$d_{34} = \sqrt{(\bar{x}_4 - \bar{x}_3)^2 + (\bar{y}_4 - \bar{y}_3)^2} \quad \text{(A.6)}$$
$$d_{41} = \sqrt{(\bar{x}_1 - \bar{x}_4)^2 + (\bar{y}_1 - \bar{y}_4)^2} \quad \text{(A.7)}$$
$$\quad \text{(A.8)}$$

and

$$m_{12} = \frac{\bar{y}_2 - \bar{y}_1}{\bar{x}_2 - \bar{x}_1} \quad \text{(A.9)}$$
$$m_{12} = \frac{\bar{y}_3 - \bar{y}_2}{\bar{x}_3 - \bar{x}_2} \quad \text{(A.10)}$$
$$m_{12} = \frac{\bar{y}_4 - \bar{y}_3}{\bar{x}_4 - \bar{x}_3} \quad \text{(A.11)}$$
$$m_{12} = \frac{\bar{y}_1 - \bar{y}_4}{\bar{x}_1 - \bar{x}_4} \quad \text{(A.12)}$$

and

$$r_k = \sqrt{(\bar{x} - \bar{x}_k)^2 + (\bar{y} - \bar{y}_k)^2 + \bar{z}^2}, \;\; k = 1, 2, 3, 4 \quad \text{(A.13)}$$
$$e_k = (\bar{x} - \bar{x}_k)^2 + \bar{z}^2, \;\; k = 1, 2, 3, 4 \quad \text{(A.14)}$$
$$h_k = (\bar{x} - \bar{x}_k)(\bar{y} - \bar{y}_k), \;\; k = 1, 2, 3, 4 \quad \text{(A.15)}$$

# Appendix B

# Analysis of Elliptical Wing Using Commercial CFD Package

CFD analysis is performed as part of the verification process of 3D panel method with boundary layer model. This appendix describes the process and settings of the CFD calculation.

**Mesh generation**

Properly generated mesh is very important for obtaining converged and trustworthy results. The wing is divided into 2D sections with constant spanwise z-coordinate (Wing surface mesh is depicted in Fig. B.1).

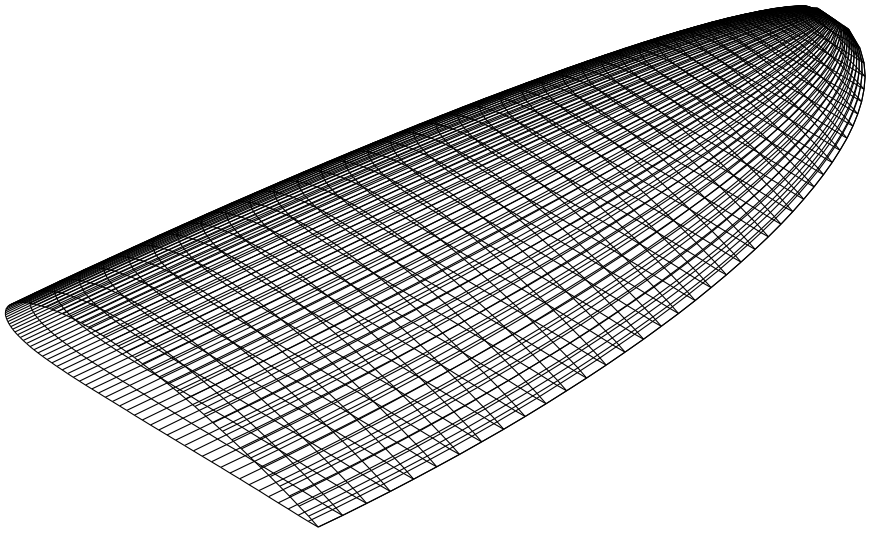

FIGURE B.1: Surface mesh of the wing.

The mesh was generated by MATLAB programmatically for a better control of the meshing process and fast mesh generation for different geometries. Hexahedral structured type of mesh was used. First, a 2D mesher script for 2D domain around an airfoil section was developed. The domain (Fig. B.2) extends more than 10 chords downstream and the shape of inlet boundary enables to set inlet-velocity condition for angles between -25° and 25°.

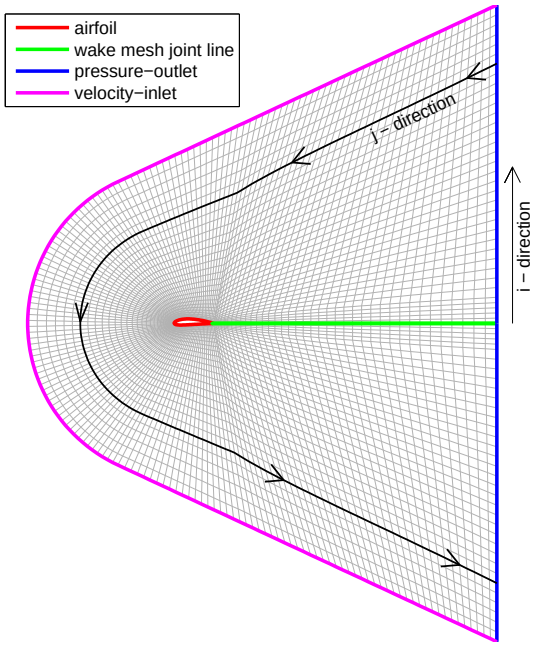


FIGURE B.2: 2D mesh in xy-plane.

To simulate boundary layer properly, an inflation layer is built around the airfoil. The height of the inflation layer is estimated as twice the height of a flat plate turbulent boundary layer $\delta_{99} \approx 0.37\xi/Re_{\xi}^{0.2}$ using free-stream velocity of planned simulations to calculate Reynolds number. This way, the boundary layer simulated by FLUENT should "fit" into the inflation layer mesh. By defining different number of cells across inflation layer height, different turbulence models can be accommodated. Only few mesh cells are required for k-$\epsilon$ turbulence model to obtain wall distance $y^+ \approx 30$, while more than 20 cells across inflation layer height are usually required in this case to produce $y^+ \approx 1$ necessary for k-$\omega$ models. The exact number of cells across inflation layer is determined by a simple trial and error, before the batch of calculations is performed. The structured mesh is produced in such way, that the inflation layer smoothly transitions into wake layer. Because the exact wake position changes with angle of attack, and the goal is to use the same mesh for all angles of attack, the wake layer cells start to grow wider just behind the trailing edge (Fig. B.3).

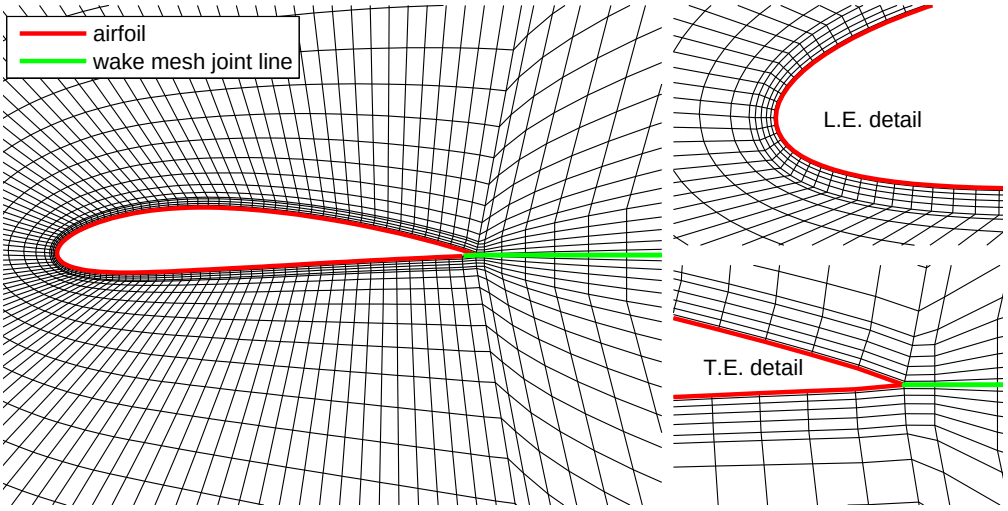


FIGURE B.3: Detail of the mesh in xy-plane.

The 3D mesher script, written using MATLAB, uses the 2D meshing procedure explained above for all wing sections up to the wing tip. For z-coordinates greater than those of the wing tip, a dummy wing extension is created with zero wing thickness and with the mesh cells of upper and lower surface interconnected.

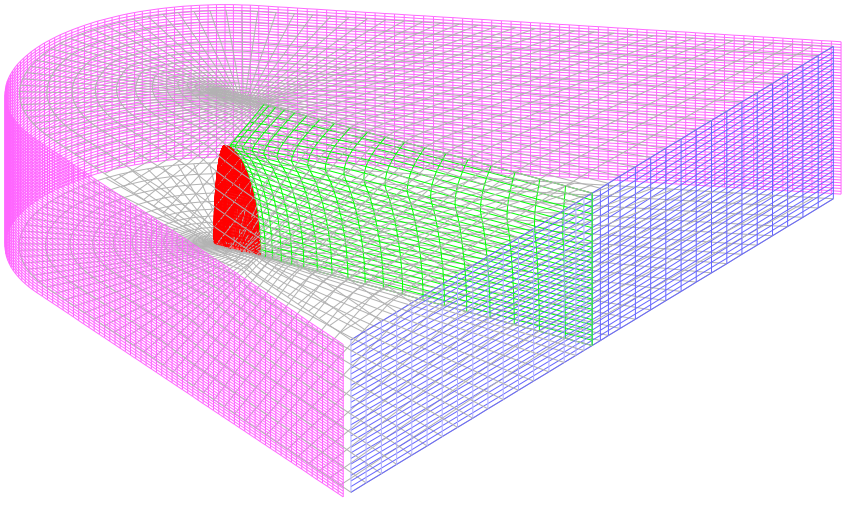

FIGURE B.4: Overview of the domain's 3D mesh.

**The following boundary conditions and settings of the model are used:**

| | |
|---|---|
| Inlet boundary condition: | velocity inlet (components of velocity) |
| Outlet boundary condition: | pressure outlet (0 relative static pressure) |
| Domain sides boundary conditions: | symmetry |
| Wing surface boundary conditions: | no-slip wall |
| Turbulence models: | k-$\epsilon$ realizable |
| | k-$\omega$ SST |
| | SST Transition |

**Results**

The lift and drag results using different turbulence models are shown in terms of their coefficients in figures B.5, B.6 and B.7.

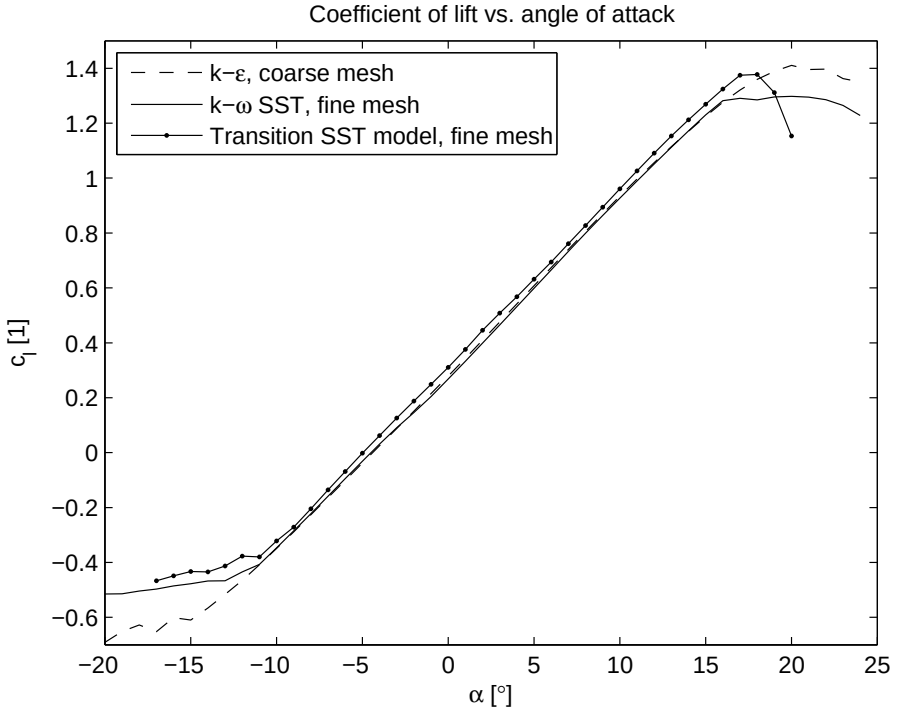


FIGURE B.5: CFD results: coefficient of lift vs. angle of attack.

In case of lift, the turbulence models provide nearly identical results in the range of $\alpha = -10°$ and $\alpha = 15°$. For larger and smaller attack angles the turbulence models provide different lift coefficient values due to different prediction of separation and stall. As expected, drag values obtained by force integration differ from drag by Trefftz plane analysis. Again, the difference between turbulence models is quite small, except for angles of attack near stall. Transition SST model was selected for 3D panel method verification, because it takes into account laminar region near leading edge, unlike the other turbulence models.

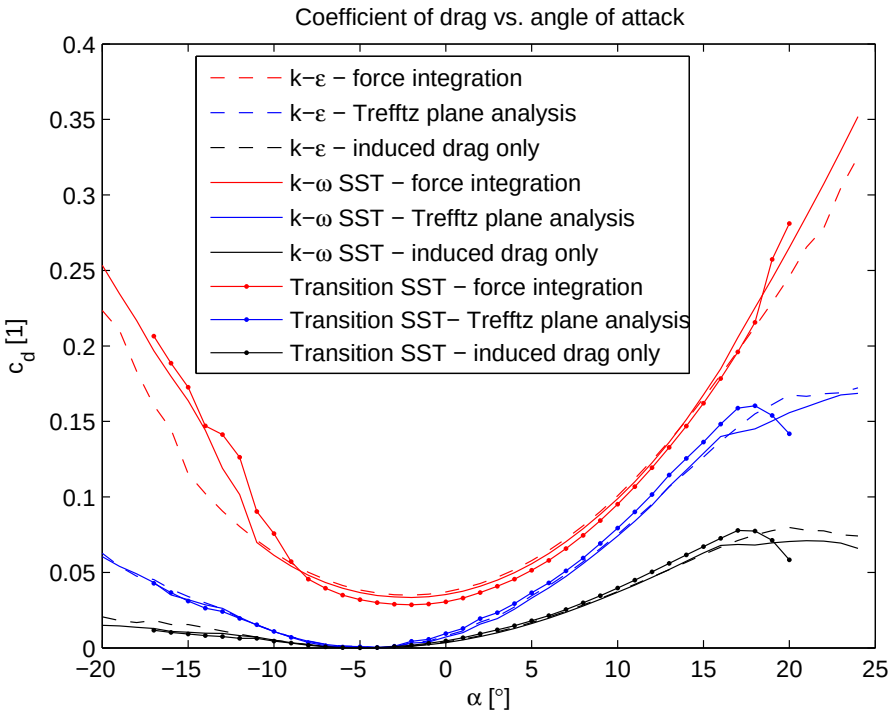


FIGURE B.6: CFD results: coefficient of drag vs. angle of attack.

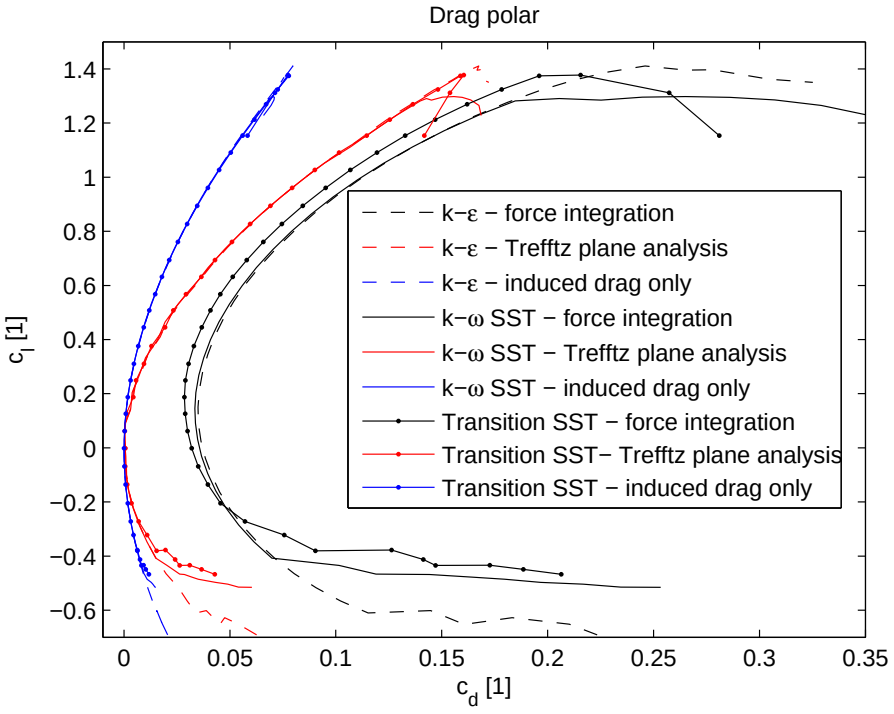


FIGURE B.7: CFD results: drag polar.

# Appendix C

# Lifting Line Tip Treatment

This appendix contains figures demonstrating the benefits of suitable tip treatment in lifting line wing discretization covered in Section 6.1.3.

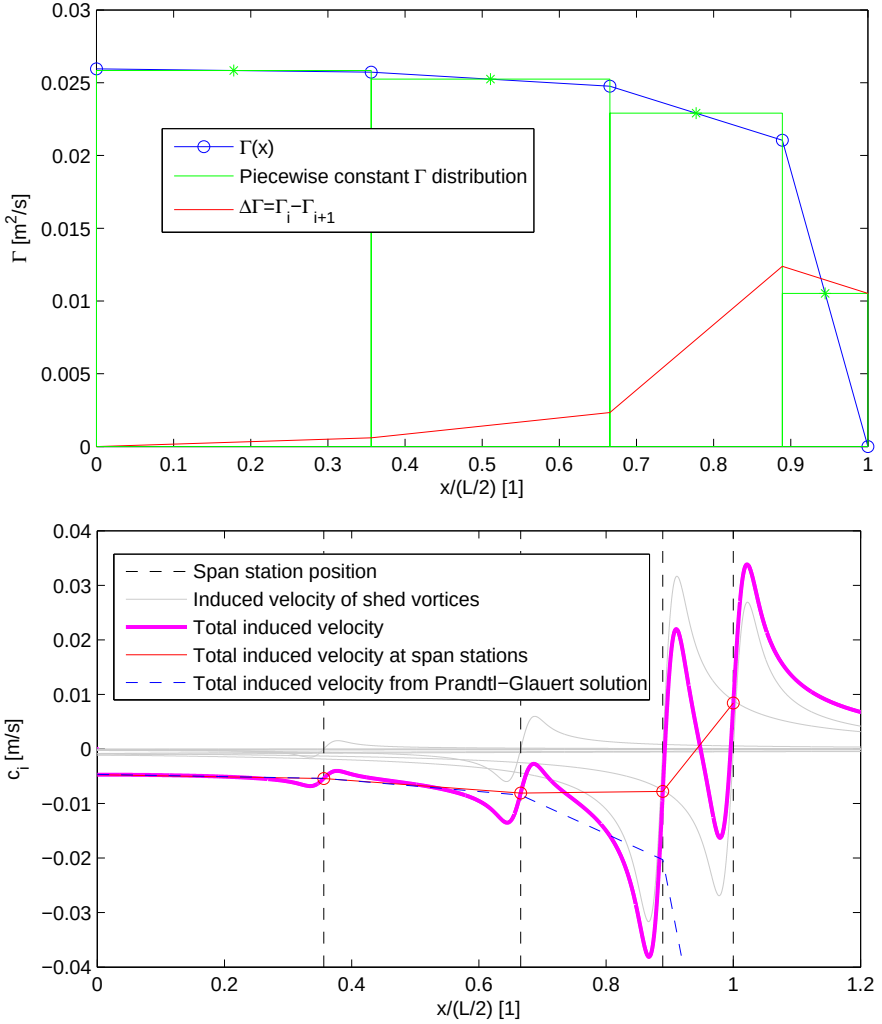


FIGURE C.1: The simplest model of the lifting line - induced velocities.

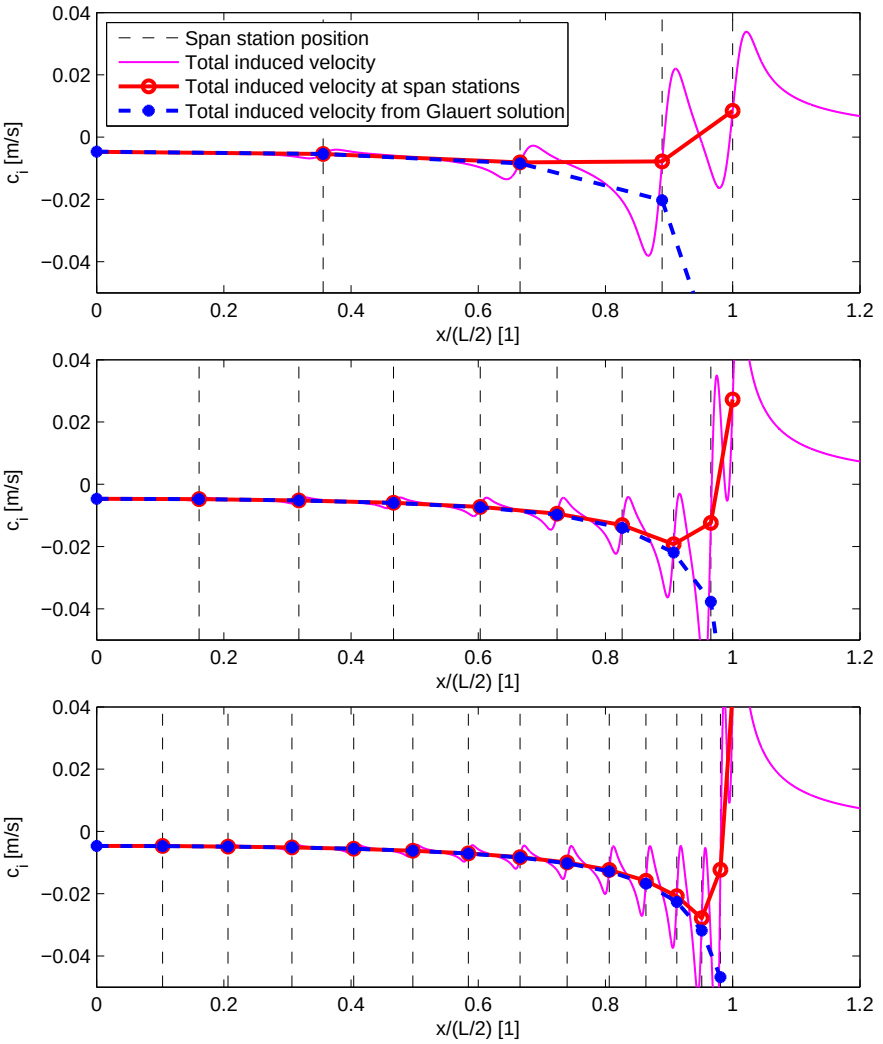


FIGURE C.2: Increasing number of lifting line segments. From top to bottom: 4, 9 and 14 segments.

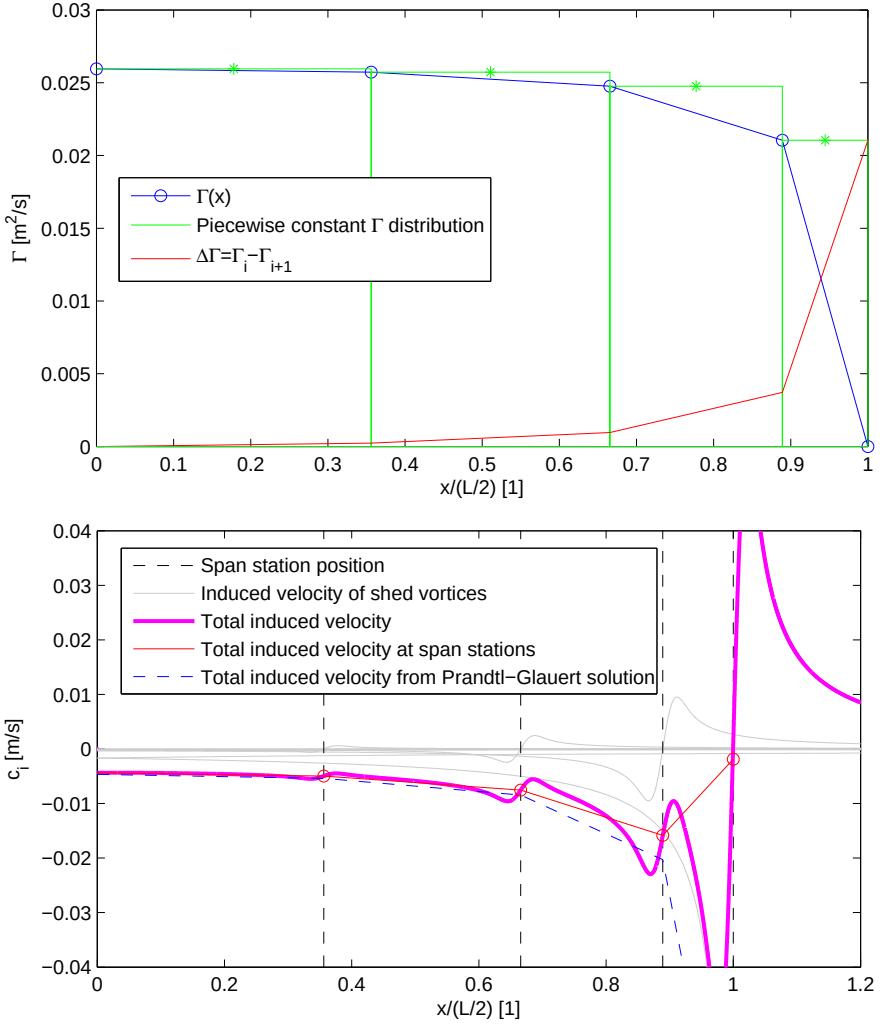


FIGURE C.3: First treatment of the tip problem - Piecewise constant circulation as maximum of neighbouring span position circulations

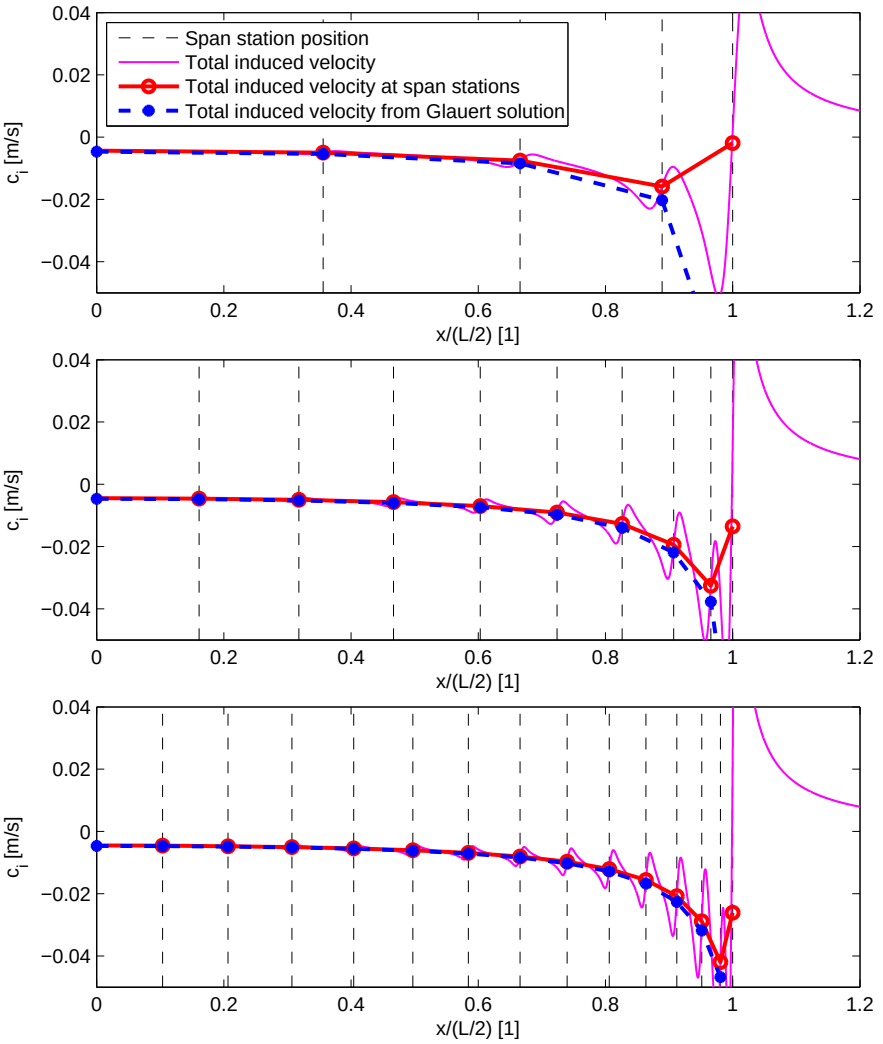


FIGURE C.4: First treatment of the tip problem - effect of the number of lifting line segments

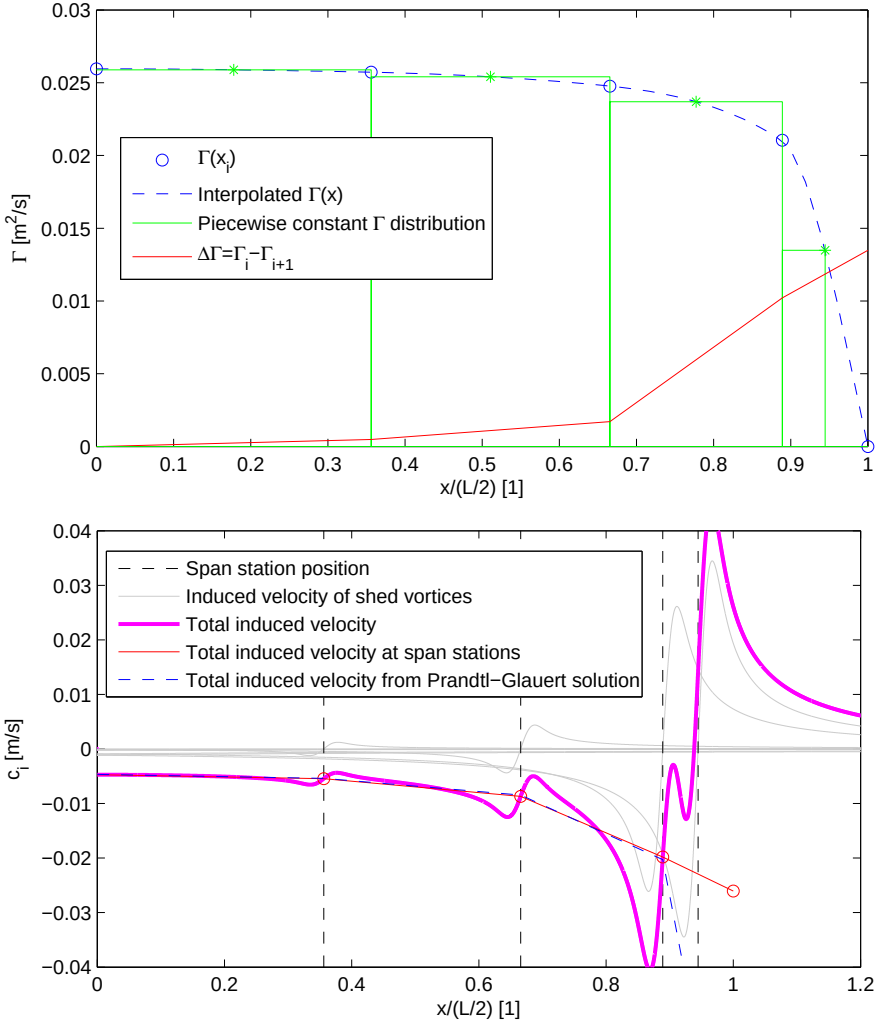


FIGURE C.5: Second treatment of the tip problem - cubic interpolation and inward shifting of tip shed vortex

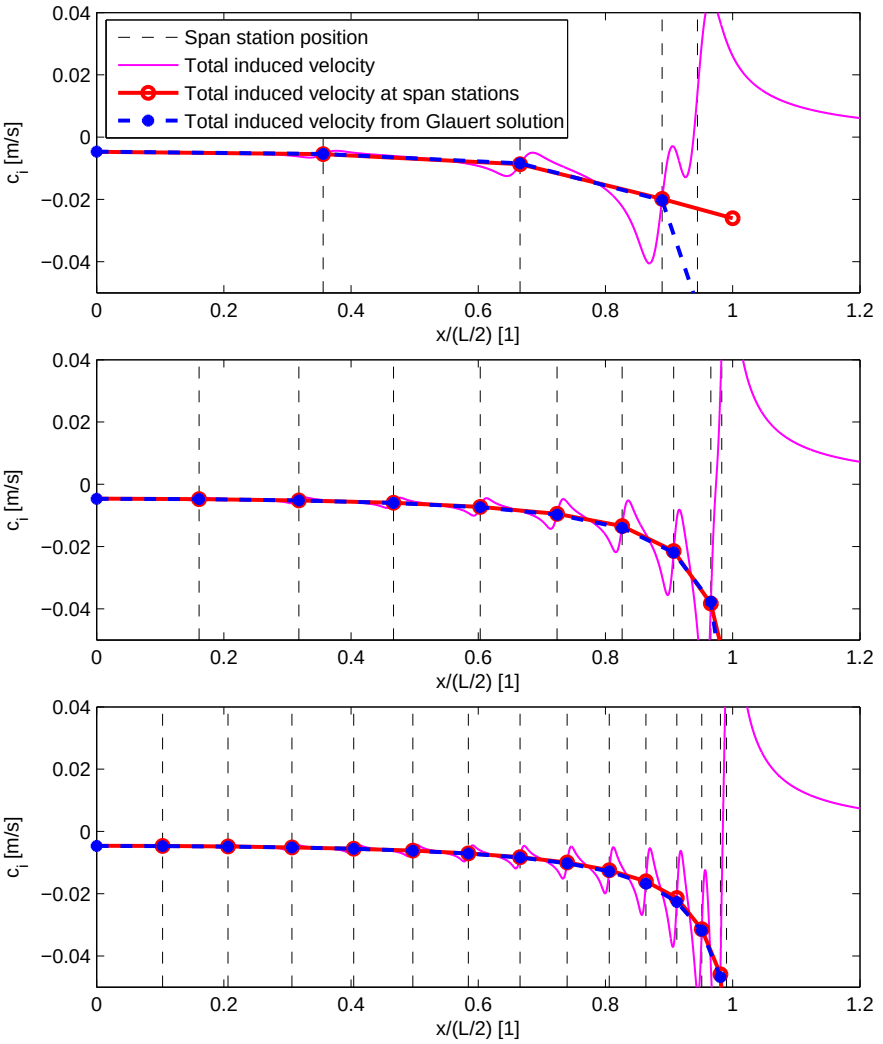


FIGURE C.6: Second treatment of the tip problem - effect of the number of lifting line segments